Study on Ferroic and Electromechanical Properties of Alkali Niobate Piezoceramics under Harsh Environment

Hiroshi Nishiyama

30511007

Supervised by

Prof. Dr. Ken-ichi Kakimoto

Life Science and Applied Chemistry
Graduate School of Engineering
Nagoya Institute of Technology

March 2021

Table of Contents

Symbols and Abbreviations

Symbols

C	Capacitance
d	Distance between inner electrodes of multilayer ceramics
d_{33}	Piezoelectric coefficient measured along the poling direction
d_{33}^*	Normalized strain, S_{Max}/E_{Max}
$d_{33}^*(\sigma)$	Stress dependence of d_{33}^*
E_a	Thermal activation energy of electrical conductivity
E_{bias}	Internal bias field, $(E_C^+ - \lvert E_C^- \rvert)/2$
E_C	Coercive field
E_C^-	Negative coercive field
E_C^+	Positive coercive field
E_{Max}	Maximum applied electric field
E_{pol}	Poling field in bipolar *P*–*E* hysteresis loop of relaxor materials
E_X^+	Crossing field at zero strain of bipolar *S*–*E* hysteresis loop
e_{loss}	Polarization energy loss
ε	Permittivity
ε_0	Permittivity of the vacuum
ε_r	Relative permittivity
η_B	Domain backswitching, $1 - S_r/S_i$
L_{π_a}	Linear extrapolation from zero point of stress–polarization hysteresis loop
L_{π_b}	Linear extrapolation from maximum field of stress–polarization hysteresis loop
L_{π_C}	Tangent line at π_C of stress–polarization hysteresis loop
L_{σ_a}	Linear extrapolation from zero point of stress–strain hysteresis loop
L_{σ_b}	Linear extrapolation from maximum field of stress–strain hysteresis loop
L_{σ_C}	Tangent line at σ_C of stress–strain hysteresis loop
L_{X_a}	Linear extrapolation from zero point of unipolar *S*–*E* hysteresis loop
L_{X_b}	Linear extrapolation from maximum field of unipolar *S*–*E* hysteresis loop
L_{X_C}	Tangent line at X_C of unipolar *S*–*E* hysteresis loop
n	Number of layers of multilayer ceramics
P_D	Defect dipole

P_{Max}	Polarization at maximum electric field
P_s	Spontaneous polarization
P_r	Remanent polarization at zero electric field
P_r^-	Negative remanent polarization
P_r^+	Positive remanent polarization
$P_{r,relax}^-$	Relaxed state of remanent polarization P_r^-
p	CPE index
π_a	Intersection between tangent line at π_C and linear extrapolation from zero point of stress–polarization hysteresis loop
π_b	Intersection between tangent line at π_C and linear extrapolation from maximum field of stress–polarization hysteresis loop
π_C	Inflection point of stress–polarization hysteresis loop
$S_{BN,a-axis}$	Dimension along a-axis related to oxygen ion conduction bottleneck in perovskite ceramics
$S_{BN,c-axis}$	Dimension along c-axis related to oxygen ion conduction bottleneck in perovskite ceramics
S_i	Ideal remanent strain
S_{Max}	Maximum strain
S_{p-p}	Peak-to-peak strain in bipolar *S*–*E* hysteresis loop
S_r	Remanent strain
σ	Electrical conductivity
σ	Stress
σ_a	Intersection between tangent line at σ_C and linear extrapolation from zero point of stress–strain hysteresis loop
σ_b	Intersection between tangent line at σ_C and linear extrapolation from maximum field of stress–strain hysteresis loop
σ_C	Coercive stress, the inflection point of stress–strain hysteresis loop
σ_{Peak}	Stress where field-induced maximum strain peak of $d_{33}^*(\sigma)$
T_C	Curie temperature
T_{CPE}	CPE constant
T_{PPT}	Polymorphic phase transition temperature
ω_{Max}	Relaxation frequency
X_a	Intersection between tangent line at X_C and linear extrapolation from zero point of unipolar *S*–*E* hysteresis loop
X_b	Intersection between tangent line at X_C and linear extrapolation from maximum field of unipolar *S*–*E* hysteresis loop

X_C	Inflection point of unipolar *S–E* hysteresis loop
Z_{CPE}	Complex impedance

Abbreviations

BNT	Bismuth sodium titanate, $Bi_{1/2}Na_{1/2}TiO_3$
BT	Barium titanate, $BaTiO_3$
BCZT	Barium calcium zirconium titanate, $(Ba,Ca)(Zr,Ti)O_3$
CAGR	Compounded annual growth rate
CPE	Constant phase element
DWs	Domain walls
El-Ceram	Electrode-ceramics
GBs	Grain boundaries
ICP-OES	Inductively coupled plasma optical emission spectrometer
LNKN	Li-modified sodium potassium niobate, $(Li,Na,K)NbO_3$
LNKN6-a	$Li_{0.06}Na_{0.52}K_{0.42}NbO_3$ containing 0.65 mol% Li_2CO_3, 1.3 mol% SiO_2, 0.2 mol% $MnCO_3$, and 0.5 mol% $SrZrO_3$
NKN	Sodium potassium niobate, $(Na,K)NbO_3$
ML	Multilayer
MLCC	Multilayer ceramic capacitors
MPB	Morphotropic phase boundary
P–E	Polarization–electric field
pc	Pseudocubic
PFM	Piezoresponse force microscopy
PPT	Polymorphic phase transition
PUND	Positive-up-negative-down
PZT	Lead zirconate titanate, $Pb(Zr_{1-y}Ti_y)O_3$
RoHS	Restriction on hazardous substances
S–E	Strain–electric field
SEM-EDS	Scanning electron microscope with an energy-dispersive X-ray spectrometer
STEM	Scanning transmission electron microscope
XRD	X-ray diffraction

1. Introduction

Electroceramics are functional ceramics that are employed in a wide range of applications. In particular, piezoceramics are fundamental components of the industry. In 2019, the global market for piezoceramic devices was estimated at $25.1 billion and is expected to expand at a compounded annual growth rate (CAGR) of 6.2% over the next five years (Fig. 1.1). In 2019, lead-free piezoelectric ceramics, which is the main topic of this thesis, represented a minimal market share (an estimated value of $172 million). However, their sales are predicted to rise with a CAGR of 20.8% by 2024, ultimately reaching global revenues of $443 million (Fig. 1.2).

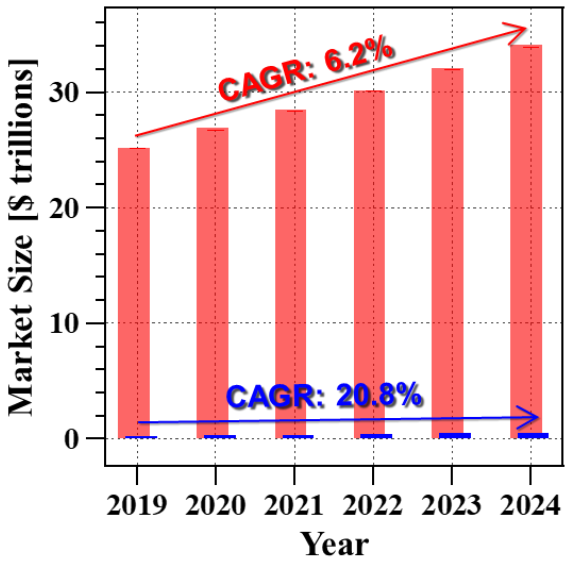

Figure 1.1: Global market for piezoelectric devices and lead-free piezoceramics. The estimated market sizes and CAGR of piezoelectric devices and lead-free piezoceramics are denoted by red and blue, respectively. The values were obtained from reference [1].

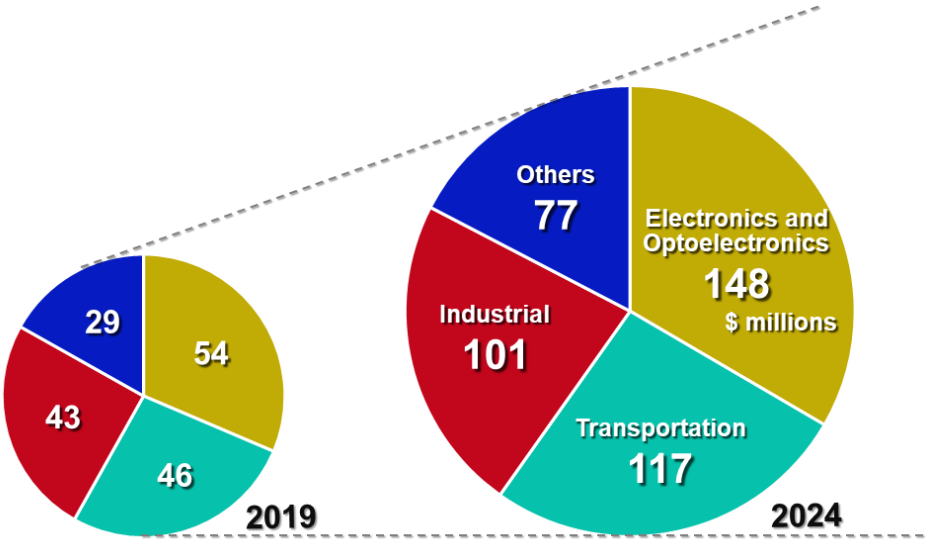

Figure 1.2: Estimated global market share breakdown for lead-free piezoceramics by application from 2019 to 2024. The values were obtained from reference [1].

One common requirement for all applications is reliability. Component reliability is particularly important in applications where actuators are difficult or impossible to exchange, such as space probes or trailing edge flaps on large wind turbines, and in applications where a long lifetime is required, such as fuel injector nozzles, thread guides in textile manufacturing, and biomedical devices that are implanted within the body. Some applications expose the piezoceramics to large mechanical stresses at high electric fields and temperatures with a long lifetime requirement. Despite the attractive electromechanical properties observed in several lead-free ferroelectrics, their mechanical reliability and macroscopic mechanical properties have been less investigated. Although there are

systematic experimental and analytical investigations of the fracture of classical ferroelectrics, such as PZT and BT [2]–[9], the phenomena that cause large unipolar strains and piezoelectric responses in newly developed lead-free piezoceramics are considerably different. Consequently, understanding the ferroelastic domain response is essential.

Further, degradation of the electric-field-induced strain and polarization during prolonged use in the unipolar driving mode is typically regarded as the domain pinning effect caused by charge agglomerations. However, as several factors, such as the domain effect and mechanical failure, simultaneously affect cyclic fatigue, the specific cause cannot be readily identified. Hence, we considered impedance spectroscopy as a powerful tool to investigate the causes of fatigue. Impedance spectroscopy is used to characterize the electrical properties of microstructures, such as grains, grain boundaries (GBs), and electrode–ceramic interfaces.

The structure and concept of this thesis are shown in Fig. 1.3. The principles of perovskite ferroelectrics are first explained, and the examples of piezoelectric applications under harsh environments are then listed. Chapters IV–VI are the main chapters. The alkali volatilization effect on the large-field ferroelectric and ferroelastic properties of (Li,Na,K)NbO_3-based bulk ceramics are summarized in Chapter IV. Consequently, the stress-dependent electromechanical properties and cyclic fatigue behaviors of (Li,Na,K)NbO_3-based multilayer (ML) piezoceramics are described in Chapters V and VI, respectively. The summary and the conclusion are listed in the last chapter.

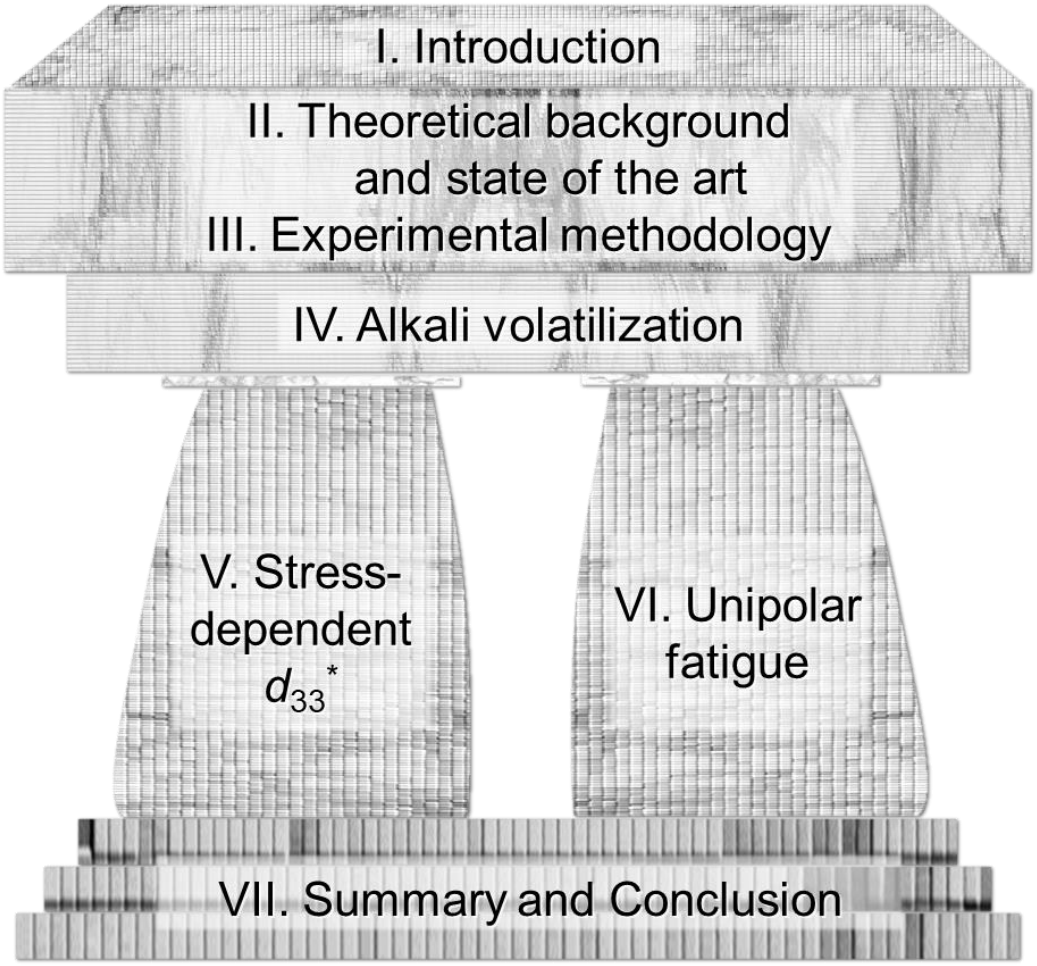

Figure 1.3: Concept and scope of this work.

2. Theoretical background

2.1 Fundamentals of ferroelectric ceramics

2.1.1 Crystal structure

Ferroelectric materials are ubiquitous in electric and electromechanical components. The largest industrial use of ferroelectric materials is in $BaTiO_3$-based ML ceramic capacitors (MLCCs), as shown in Fig. 2.1. The capacitance (C) of MLCCs is based on the formula for a plate capacitor enhanced with the number of layers:

$$C = \varepsilon \cdot \frac{n \cdot A}{d}$$

where ε is the permittivity, A is the electrode surface area, n is the number of layers, and d is the distance between the electrodes.

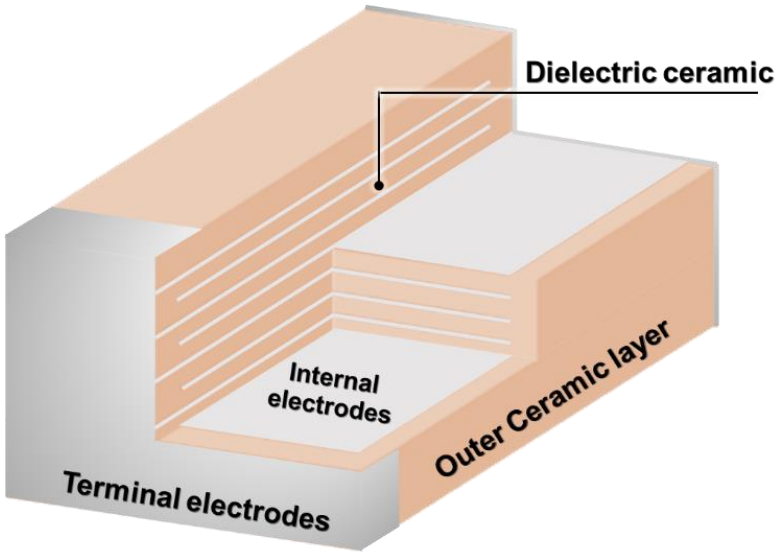

Figure 2.1: Schematic structure of a multilayer ceramic capacitor (MLCC) [10].

$BaTiO_3$ ferroelectric ceramics exhibit high permittivity due to their relatively closely spaced phase transitions, which enables high relative permittivity over a broad temperature range. Figure. 2.2 depicts the temperature-dependent permittivity of $BaTiO_3$ single crystals. $BaTiO_3$ has a perovskite structure, and the crystal phase changes over the temperature range. Each of these temperature-dependent phase transitions is referred to as a polymorphic phase transition (PPT) [11], rather than a morphotropic phase transition (MPB), which is composition dependent [12]. The cubic, tetragonal, orthorhombic, and rhombohedral phases are stable at > 130 °C, 0 °C to 130 °C, –90 °C to 0°C, and < −90 °C, respectively.

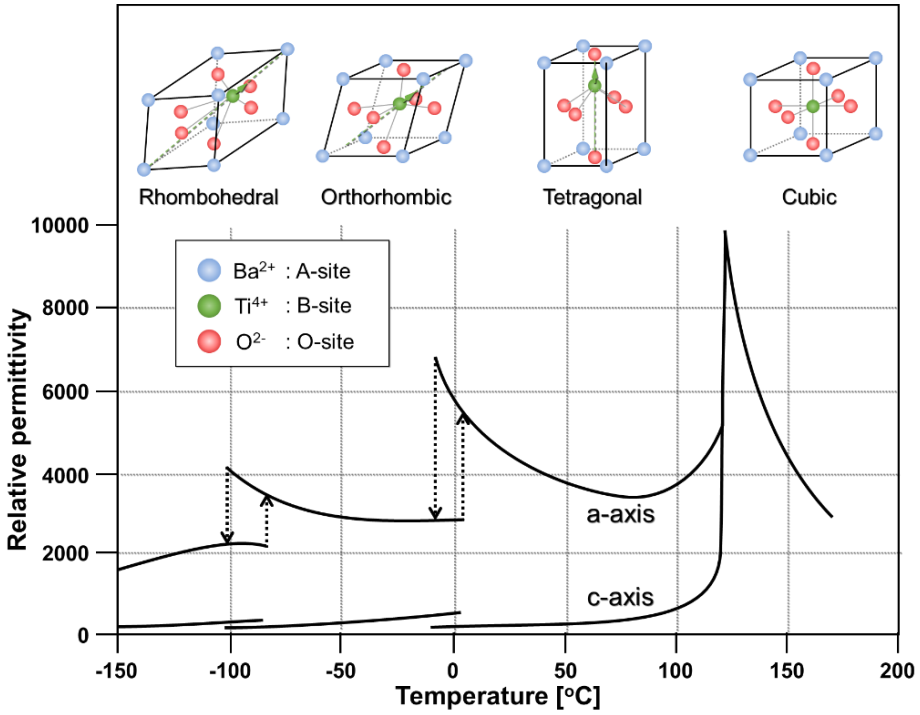

Figure 2.2: Temperature-dependent permittivity of the $BaTiO_3$ single crystal and corresponding crystal structures [13]. The spontaneous polarization P_S is denoted by green arrows.

The defining characteristic of ferroelectric materials is the existence of spontaneous dipoles (P_S) within their crystal structures, whose direction can be reoriented by the application of an electric field (Fig. 2.3). In other words, all materials belonging to a polar point group are potentially ferroelectric, but ferroelectric materials must demonstrate polarization reversal.

One of the most significant characteristics of ferroelectric ceramics is their ability to exhibit single crystal-like behavior, even when fabricated as polycrystalline ceramics, which can reorient the direction of P_S. The use of ferroelectric ceramics as piezoceramics depends on the ability to break full isotropic symmetry by applying a poling field and thus relies on the extrinsic effects (domain wall motion) in ferroelectrics. Intrinsic piezoelectricity is initially linear under a small field, so applying +5 V in one direction will produce equal and opposite strain to applying −5 V in the same direction [14]. Sintered polycrystalline ceramics all collectively cancel out their neighbors, and the net strain is zero macroscopic piezoelectric response. For this reason, quartz piezoelectrics, such as those used for timekeeping in watches, must be single crystals. Accordingly, in order for polycrystalline ferroelectric materials to be used as piezoceramics, the macroscopic random symmetry of the grains must be broken. The macroscopic symmetry of a polycrystalline ceramic sample is typically broken by applying a large electric field. The applied field aligns the crystallographic dipoles; the poling treatment is assisted by the field-induced alignment of P_S.

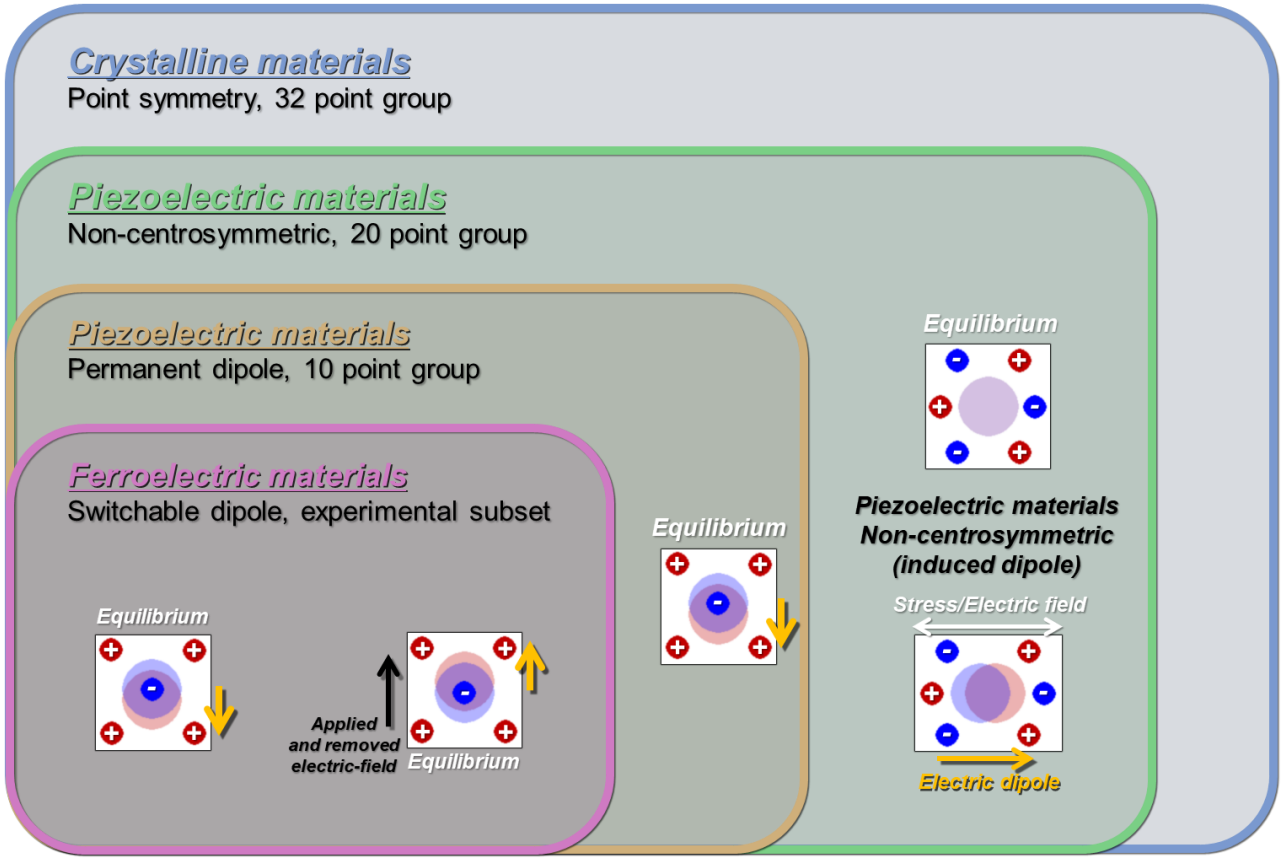

Figure 2.3: Classification of dielectrics. Of the crystalline or polycrystalline materials that exhibit piezoelectric behavior, some are pyroelectric, and of those, some are ferroelectric [10]. Materials are classified into these categories based on the symmetry of their unit cell, and their thermal, electrical, and mechanical energies.

2.1.2 Domain structure

The previous section describes the importance of the poling treatment for piezoceramics. However, the morphology of piezoceramics requires elucidation. Figure 2.4 depicts the typical domain structure of the ferroelectric (Na,K)NbO_3-based ceramic sample.

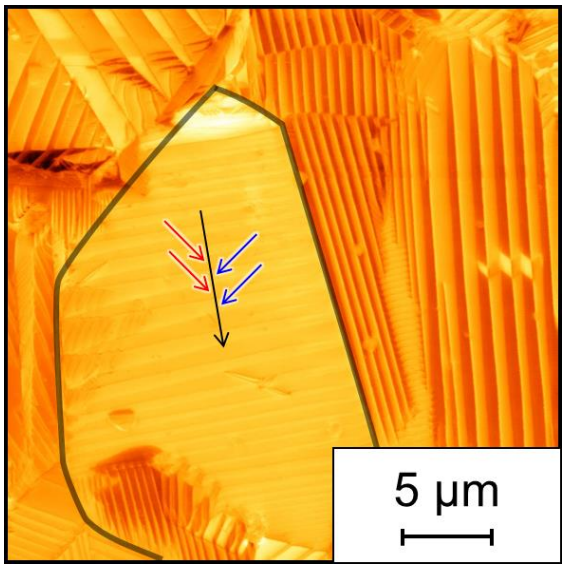

Figure 2.4: Representative ferroelectric domain structure of (Na,K)NbO_3-based piezoceramics. The PFM amplitude of the mirror-polished surface is shown.

Polarization reversal is the defining characteristic of ferroic materials, and the hysteric response is often represented as a plot of polarization vs. electric field, as shown in Fig. 2.5(a). The corresponding domain illustration is summarized in Fig. 2.5(b). Diagrams (I) to (IV) depict how the domain structure responds to the applied field in a single grain at different stages on the hysteresis loop. The corresponding *S*−*E* hysteresis loop is shown in Fig. 2.5(c). These *P*−*E* and *S*−*E* hysteresis loops were characterized with two bipolar pulses (Fig. 2.5(d)).

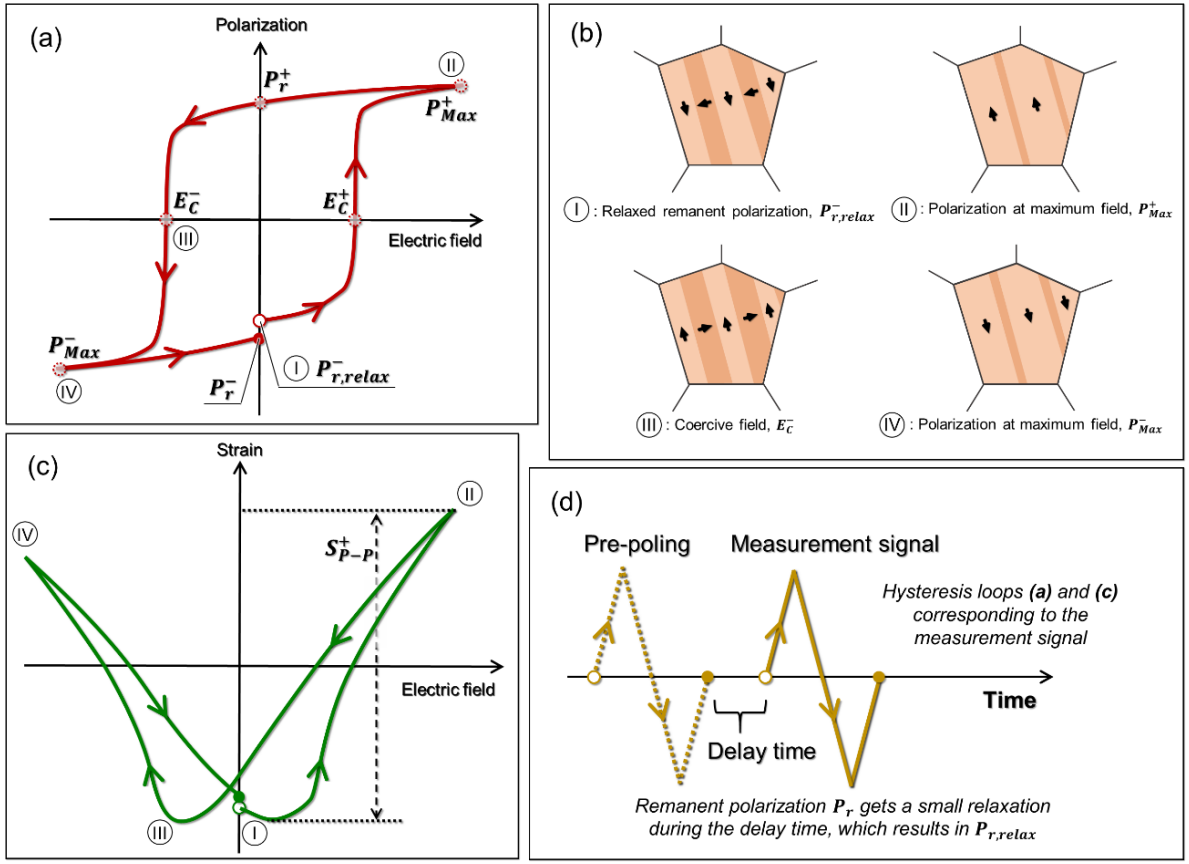

Figure 2.5: (a) Representative *P*−*E* hysteresis loop and (b) schematic evolution of the domain structure. (c) Representative *S*−*E* hysteresis loop. (d) Pre-poling pulse and measurement signal corresponding to (a) and (c) (after the reference) [10].

2.2 Piezoceramics under harsh environments

The miniaturization of electronic devices and performance improvements are required to satisfy the increasingly stringent performance requirements. Long-term stability under harsh conditions, including elevated temperatures, strong electric fields, and compressive stress, is of paramount importance to ensure reliable drive operation.

2.2.1 Piezoelectric coupling

Figure 2.6 depicts a Heckmann diagram, which describes the relationship between external fields and order parameters. Both ferroelectric and ferroelastic materials have periodic domain structures; therefore, these ferroic materials exhibit ferroelectricity and ferroelasticity. Additionally, ferroic materials exhibit stress-induced-polarization and electric-field-induced strain (Fig. 2.7); these responses are called direct and converse piezoelectric effect, respectively.

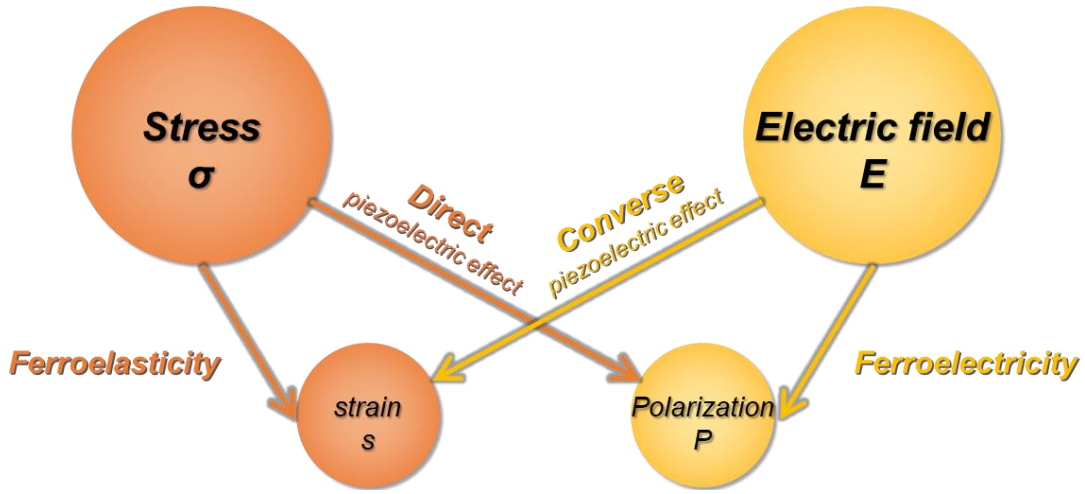

Figure 2.6: Part of a Heckmann diagram showing the relationship between the mechanical and electrical properties of ferroic materials [15].

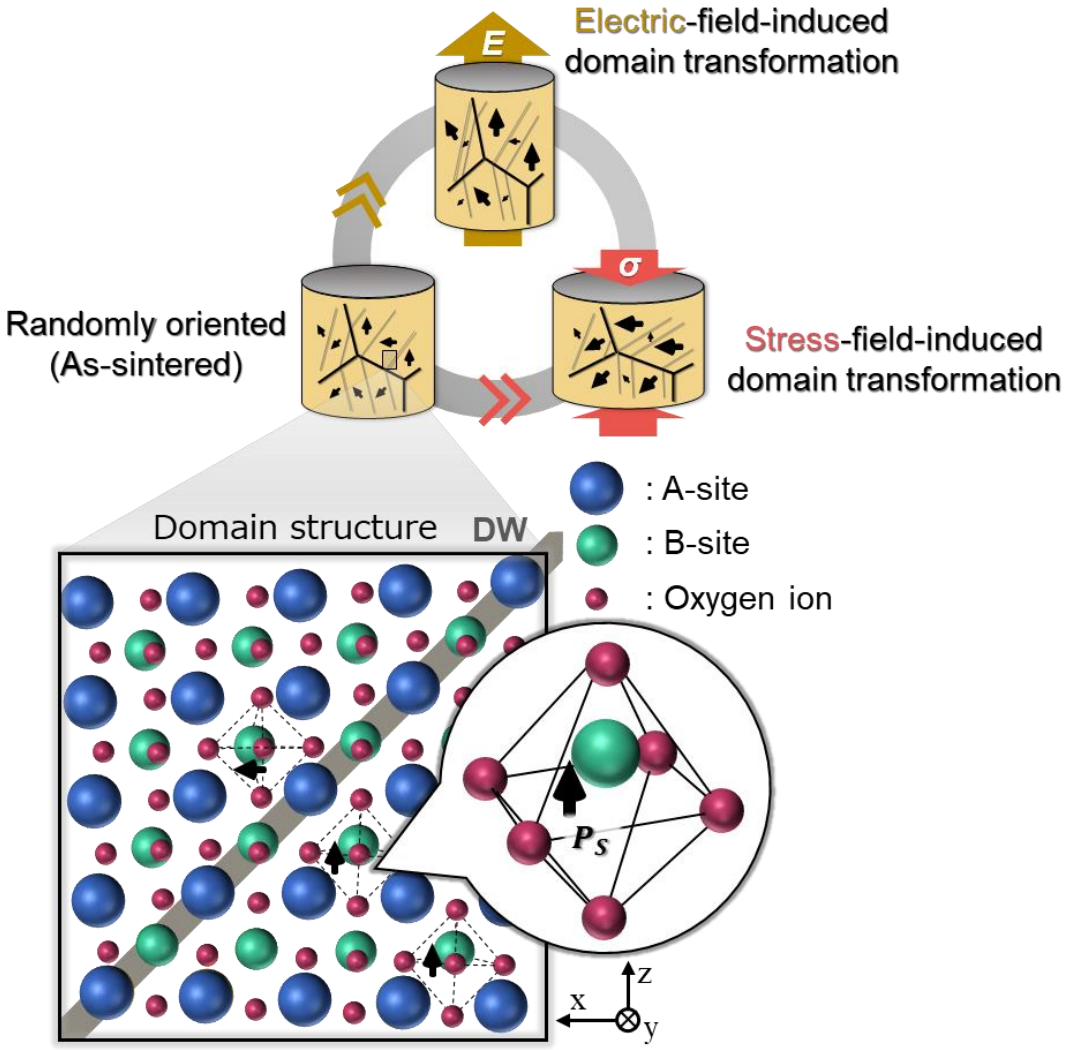

Figure 2.7: Schematic illustration of ferroelectric and ferroelastic domain transformation.

2.2.2 Large-signal properties under uniaxial compressive stress

Bipolar *P*−*E* and *S*−*E* hysteresis loops of piezoceramics exhibit a constant decrease in P_{Max} and S_{Max}, respectively, owing to domain clamping under the uniaxial compressive stress (Fig. 2.8). Conversely, unipolar *P*−*E* and *S*−*E* hysteresis loops exhibit an enhancement at a specific stress level; −50 MPa in this case. This enhancement originated from the balance of the orientation of non-180° domain structures toward the in-plane and out-of-plane directions by uniaxial compressive stress and the unipolar electric field, respectively. Electrically poled piezoceramics exhibit out-of-plane oriented domain structures before stress application. Up to a certain stress level, in-plane-oriented domains caused by a constant uniaxial compressive stress can reorient toward the out-of-plane direction due to the large electric-field application; this resulted in an apparent enhancement at −50 MPa.

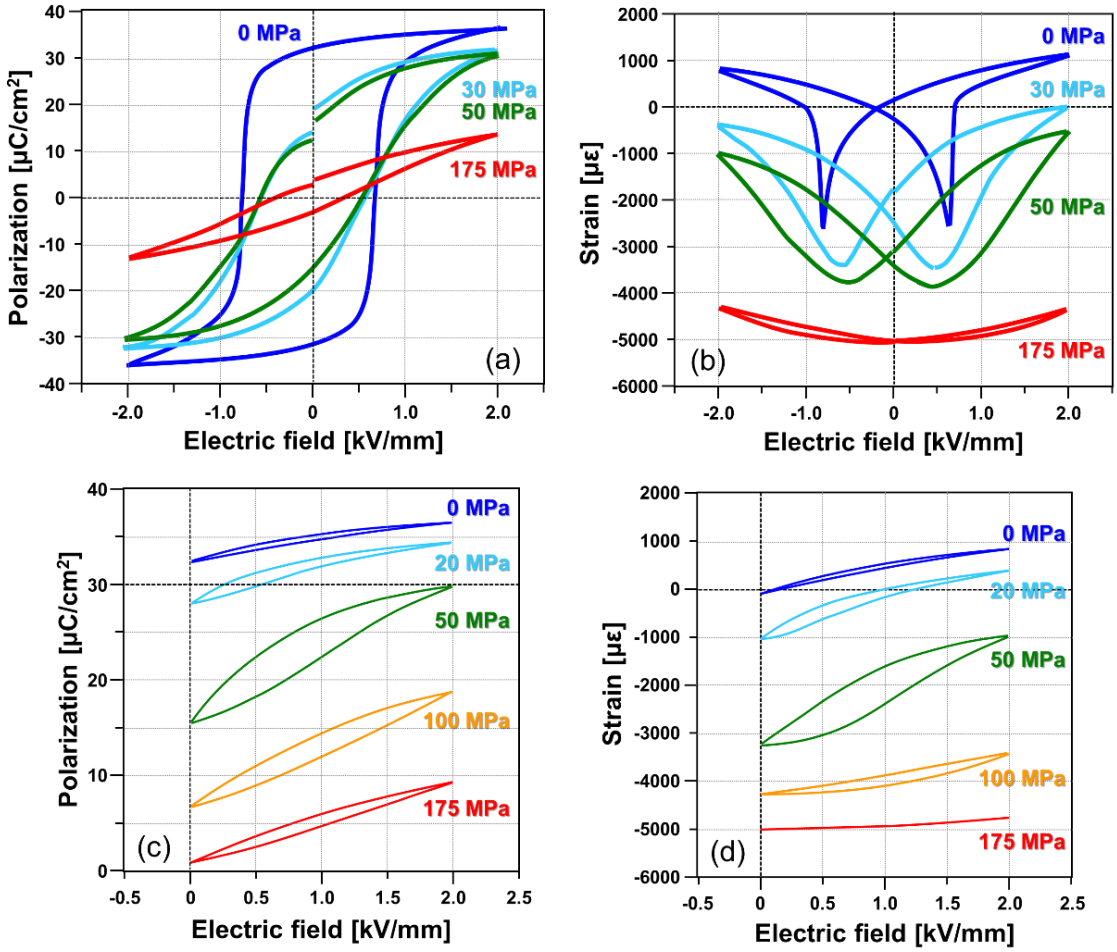

Figure 2.8: Stress-dependent large-signal responses of as-poled $Pb(Zr,Ti)O_3$ piezoceramics. All samples were electrically poled prior to the measurements. (a) Bipolar *P*−*E* and (b) *S*−*E* hysteresis loops exhibited a constant decrease in P_{Max} and S_{Max}, respectively. Conversely, (c) unipolar *P*−*E* and (d) *S*−*E* hysteresis loops exhibited an enhancement at −50 MPa (Reprinted with permission from [16]. Copyright 2001 © AIP Publishing.)

2.3 Fatigue processes

2.3.1 Classification of fatigue processes

Regardless of the lead content, piezoceramic fatigue under harsh conditions is an important consideration for future commercial use. Mobile charged defects stabilize a given domain configuration, thereby generating an internal bias field that counteracts the polarization reversal when an electric field is applied. Several recent studies have focused on fatigue mechanisms in piezoelectric ceramics [17],[18]. Carl and Härdtl identified three mechanisms, i.e., the volume, domain, and GB effects, based on their length scales (Fig. 2.9) [19]. The volume effect is associated with defect dipoles, which mainly form between B-site acceptor ions and neighboring oxygen vacancies (Fig. 2.10) [20],[21]. The domain effect is due to the accumulation of charged defects near domain walls (DWs), which hinders the transformation of domains (Fig. 2.11-2.13) [22]. The GB effect is related to the diffusion of ions, vacancies, or electrons to GBs. The GB effect includes the transformation of space charge associated with charge accumulation at the GBs and mechanical failures observed at the GBs near the electrodes during bipolar actuation (Fig. 2.14) [23].

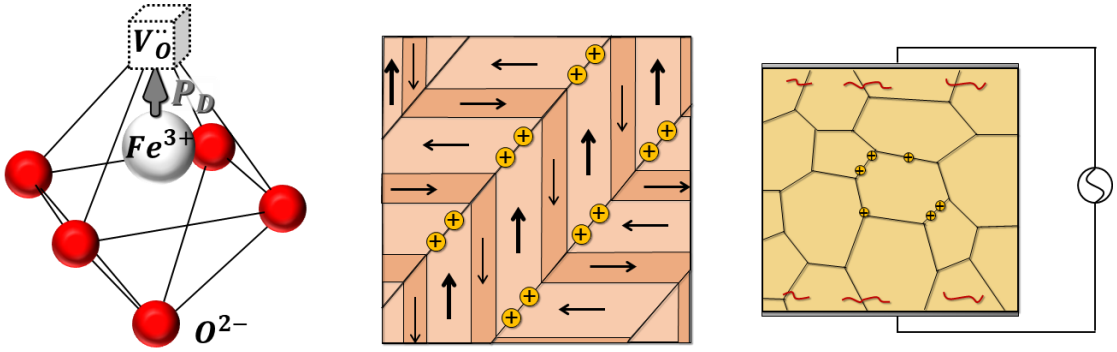

(a) Volume effect (b) Domain effect (c) Grain boundary effect

Figure 2.9: Classification of the different domain stabilization mechanisms based on their length scales and irreversible microstructural changes (based on the classification proposed by Genenko et al. [17].)

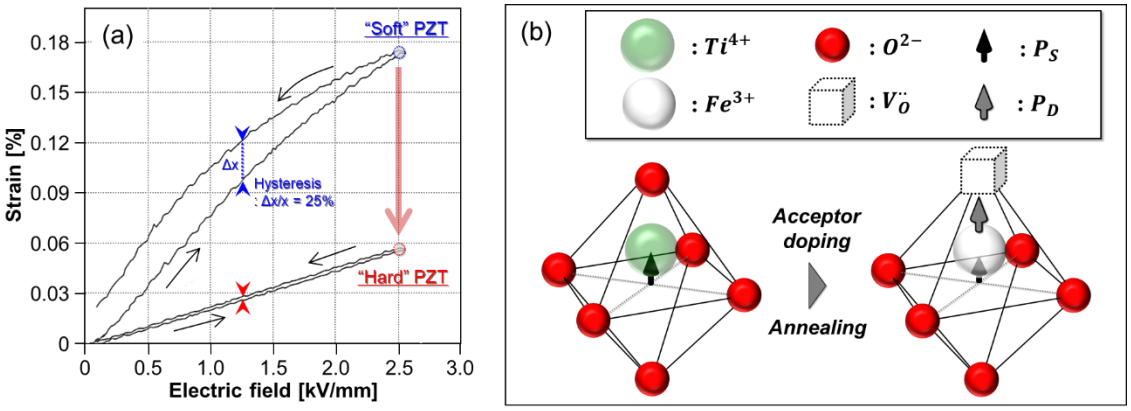

Figure 2.10: Volume effect of the hard PZT ceramics. (a) Unipolar *S*−*E* hysteresis loops of soft and hard PZT ceramics. (Reprinted with permission from [12]. Copyright 2007 © Springer Nature.) (b) Mechanism of the defect dipole P_D in the hard PZT ceramic sample [24].

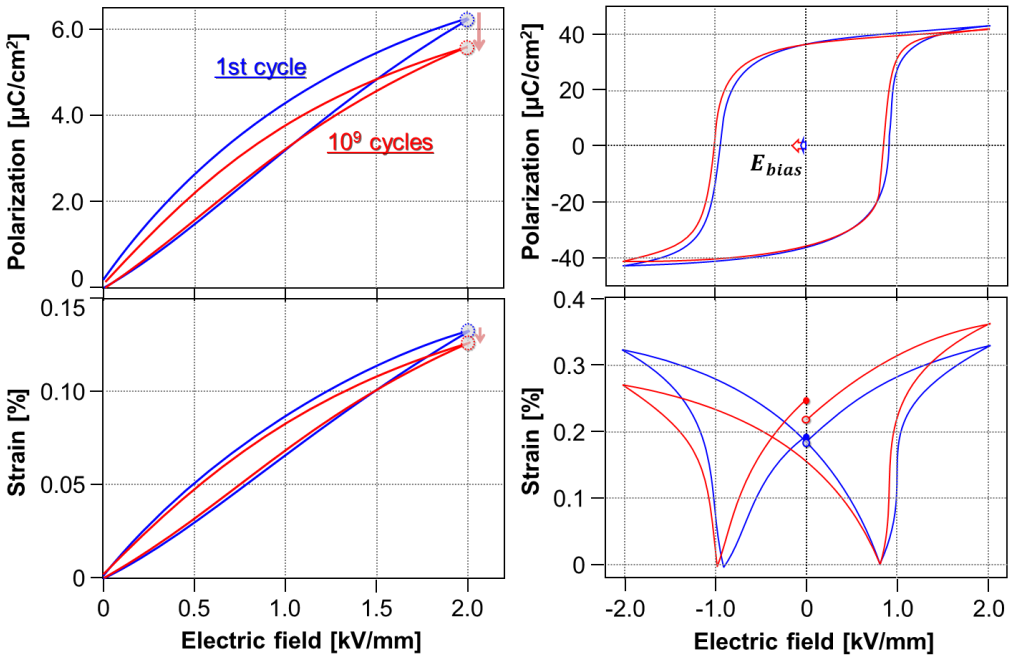

Figure 2.11: Unipolar fatigue of soft PZT ceramics. (a, b) Unipolar *P*−*E* and *S*−*E* hysteresis loops. (c, d) Bipolar *P*−*E* and *S*−*E* hysteresis loops. (Reprinted with permission from [25]. Copyright 2007 © John Wiley and Sons.)

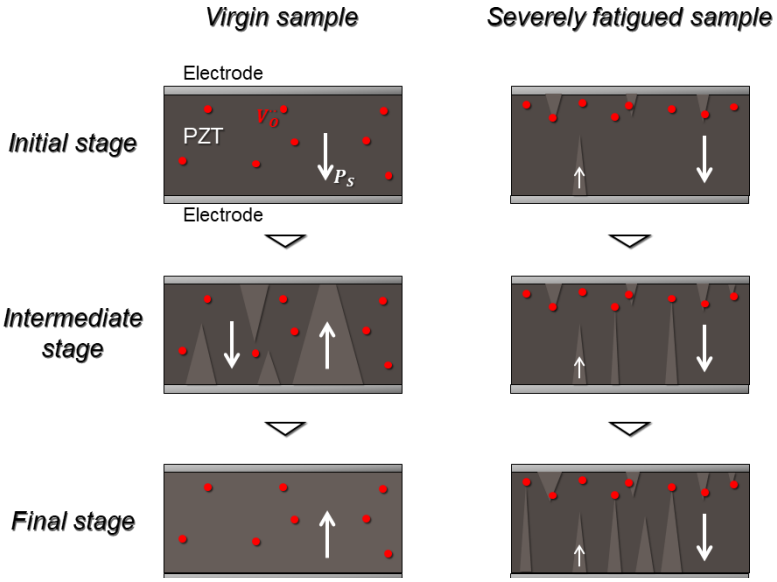

Figure 2.12: Schematic diagrams of the cross-section of the PZT ceramics showing the time-dependent domain switching process for different fatigued states [26].

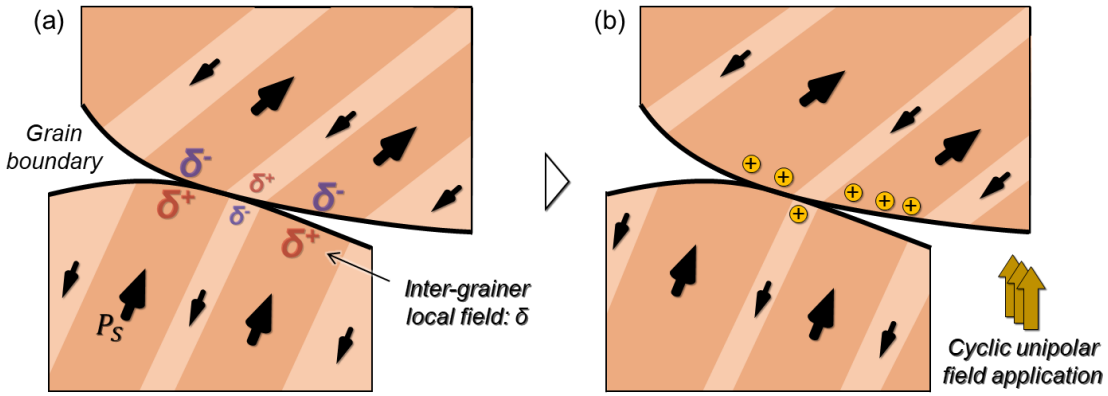

Figure 2.13: Schematic Illustrations of charge carrier agglomeration in the vicinity of the GBs during unipolar fatigue process [27].

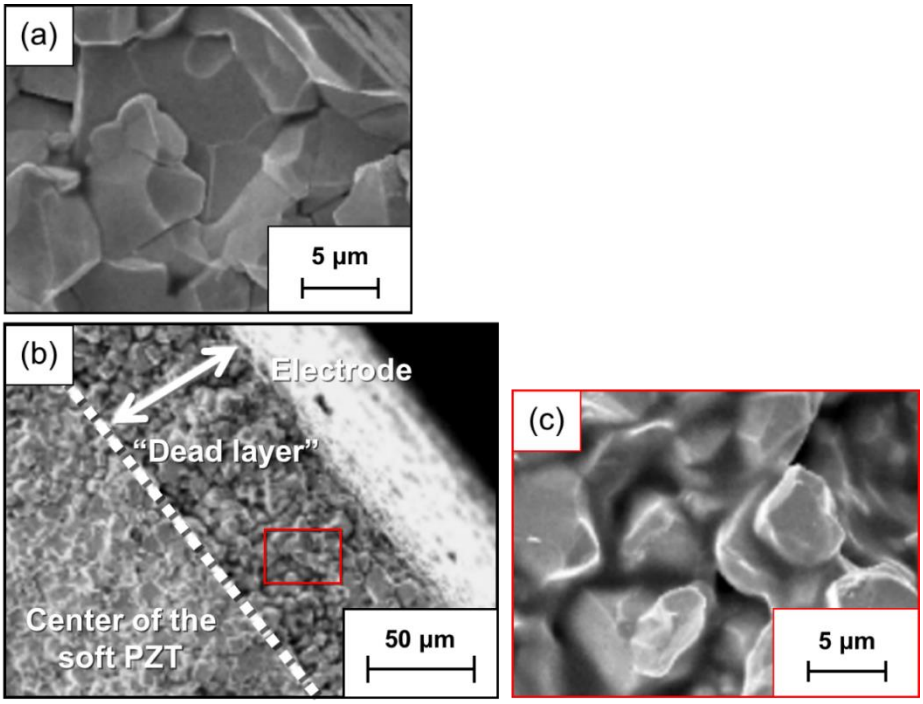

Figure 2.14: Fracture surfaces of (a) unfatigued and (b, c) fatigued PZT ceramics after 3 × 10^5 cycles of bipolar actuation. (Reprinted with permission from [23]. Copyright 2007 © John Wiley and Sons.)

2.4 Lead-free alkali niobate piezoceramics

Although PZT and other lead-based ferroelectric piezoceramics exhibit the most feasibility for electromechanical applications, the European Union Restriction on Hazardous Substances (RoHS) directives have restricted the use of certain hazardous substances, thus prompting investigations into materials with reduced lead and lead-free piezoceramics.

2.4.1 Crystal phase of Li-modified $(Na,K)NbO_3$

Lead-free piezoceramics have been extensively investigated over the past decades because of their environmental sustainability [28]–[30]. During this period, a series of lead-free piezoceramics, based on $0.94(Bi_{1/2}Na_{1/2})TiO_3$-$0.06BaTiO_3$ (BNT-6BT) [31]–[33], $(Ba_{1-x}Ca_x)(Zr_yTi_{1-y})O_3$ (BCZT) [34]–[36], and $(Na,K)NbO_3$ [37]–[39] solid solutions have been discovered. Among these, $(Na,K)NbO_3$ ferroelectrics exhibit a high Curie temperature T_C and excellent piezoelectric properties d_{33} [38]. Thus, $(Na,K)NbO_3$ is considered as a promising candidate for substituting lead-based piezoceramics for certain applications. To date, most research has focused on understanding the structural origin of the piezoelectric properties in $(Na,K)NbO_3$. Unlike $Pb(Zr,Ti)O_3$ (PZT) and BNT-6BT, which have a morphotropic phase boundary (MPB) composition, $(Na,K)NbO_3$-based materials have a PPT at elevated temperatures between the orthorhombic ($Amm2$) and tetragonal ($P4mm$) phase, as shown in Figure 2.15. At this temperature, the piezoelectric properties are enhanced because of the coexistence of two phases [40]. By shifting the PPT to lower temperatures via

doping, this enhancement could be achieved at room temperature [38]. Furthermore, recent studies have also attempted to additionally shift the low temperature rhombohedral phase to room temperature levels with different co-dopants [41]–[43]. As a result, a rhombohedral to tetragonal phase transition temperature was achieved at room temperature with enhanced electromechanical properties and increased thermal stability [43],[44]. Similarly, enhanced piezoelectric properties can be achieved at room temperature by using Li as a dopant. Figure 2.16 depicts the phase diagram $Li_x(Na_{0.5}K_{0.5})_{1-x}NbO_3$ ceramics. The crystal structure of $Li_x(Na_{0.5}K_{0.5})_{1-x}NbO_3$ (LNKN) is initially orthorhombic ($Amm2$) for x < 0.05 [45], while a coexistence of monoclinic (Pm) and tetragonal ($P4mm$) phases appears for $0.05 \leq x \leq 0.07$, as determined by Raman spectroscopy [45] and X-ray diffraction (XRD) [46]–[48]. It is believed that this phase coexistence is closely related to the enhancement of piezoelectric properties.

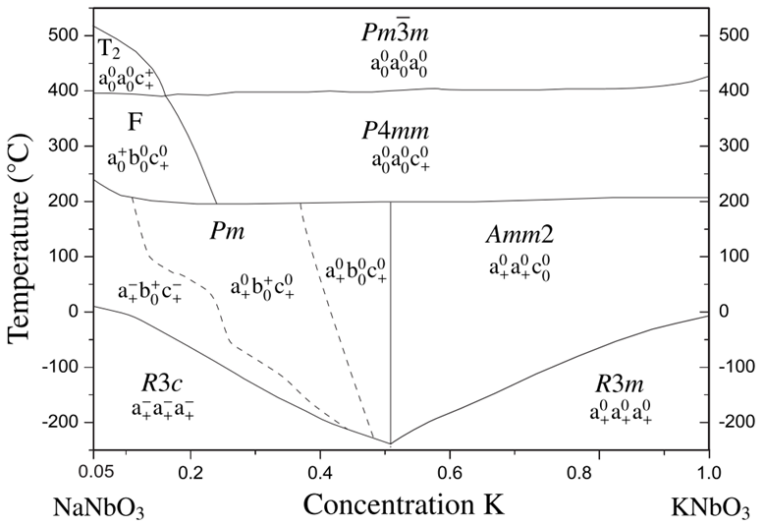

Figure 2.15: Phase diagram of (Na,K)NbO_3, showing oxygen tilting (superscript) and cation displacements (subscripts) for each phase. Dashed lines represent changes in the tilt system. (Reprinted with permission from [40]. Copyright 2009 © AIP Publishing.)

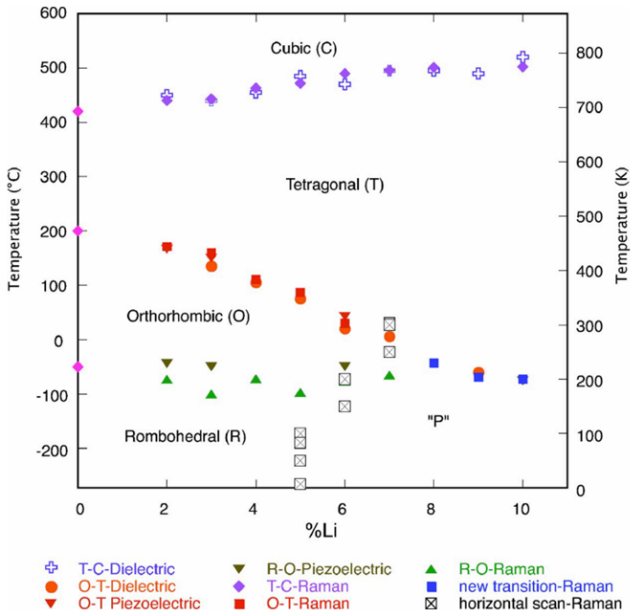

Figure 2.16: Phase diagram of $Li_x(Na_{0.5}K_{0.5})_{1-x}NbO_3$ solid solution for $0 \leq x \leq 0.1$, based on dielectric permittivity, piezoelectric response, and Raman spectroscopy measurements of ceramic samples ($0.02 \leq x$), revealing the

presence monoclinic phase (P), which maintains a vertical boundary with the rhombohedral phase. A triple point where the T, P, and O phases meet is approximately at x = 0.07. (Reprinted with permission from [45]. Copyright 2007 © AIP Publishing.)

2.4.2 Alkali volatilization

Meanwhile, most LNKN piezoceramics are synthesized within a narrow processing window based on the sintering temperature and dwelling time. A slightly higher temperature or prolonged dwelling time during the sintering step can easily cause significant volatilization of the alkali metal elements and abnormal grain growth, which results in inferior piezoelectric properties [49]–[52]. For example, the piezoelectric d_{33} constant of LNKN piezoceramics sintered at 1060 °C exhibited the highest value (314 pC/N), while that LNKN piezoceramics sintered at 1080 °C was only 220 pC/N [49]. Therefore, sintering studies have been conducted to determine the critical sintering temperatures and dwelling times. Wang et al. reported that although high temperatures (> 1050 °C) were required to obtain well-densified LNKN piezoceramics, alkali volatilization (particularly of Na) occurred at > ~1000 °C [50]. Conversely, Wang et al. reported that $(Li_{0.04}Na_{0.48}K_{0.48})(Nb_{0.80}Ta_{0.20})O_3$ piezoceramics sintered at 1145 °C for 1 h exhibited significant volatilization (particularly of K) when the ceramics were annealed without a protective atmosphere, resulting in increased PPT temperature T_{PPT} and decreased Curie temperature T_C [51]. Thus, inappropriate sintering conditions induce the volatilization of A-site alkali ions.

2.4.3 Multilayered piezoceramic actuator

ML piezoceramic actuators are one of the most important piezoelectric components; thus, (Na,K)NbO_3-based ML piezoceramics have been fabricated for decades [53]–[62]. In addition to large displacements at low driving voltages, another advantage is the capability of co-firing with base metals, allowing for lower production cost [54],[55],[58],[60]–[63]. More recently, Hatano et al. reported that LNKN-based ML piezoceramics (thickness: 13 μm) and Ag/Pd electrodes exhibited a superior d_{33}^* to PZT ML piezoceramics (thickness: 50 μm) at the same voltage (208 V). The applied fields were 16.0 kV/mm and 4.2 kV/mm for LNKN and PZT ML piezoceramics, respectively [64]. Thus, the improvement of piezoelectric properties in (Na,K)NbO_3-based ML piezoceramics has been investigated.

3. Experimental methodology

This chapter describes the experimental methods used throughout the thesis.

3.1 Large-signal properties

Large-signal properties were characterized using a specific signal. For *P*−*E* and *S*−*E* hysteresis measurements, three continuous signals were selected to obtain closed *P*−*E* and *S*−*E* loops (Fig. 3.1). On the other hand, the first strain response was determined from two continuous unipolar stress cycles for stress−strain measurement. For the stress−strain measurement, most of the ferroelastic domain orientation occurs in the first cycle, and almost no additional remanent strain is produced in the second cycle.

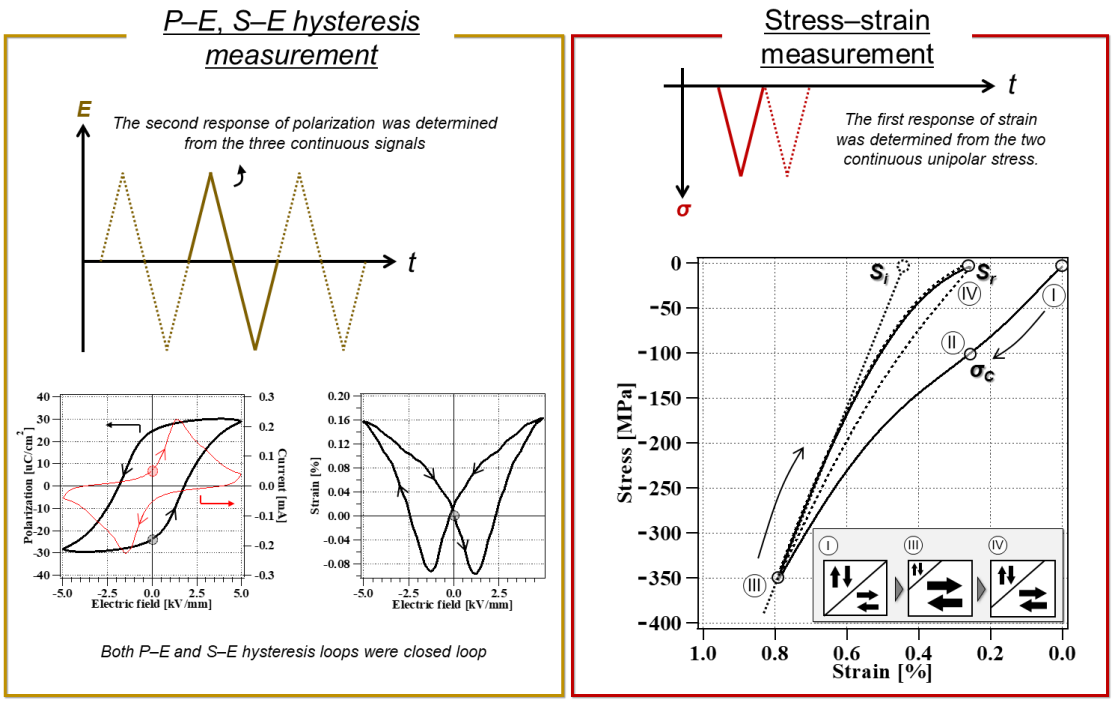

Figure 3.1: Large-signal measurement programs.

3.2 Mechanical setup

Electric-field-induced strain under uniaxial compressive stress and stress−strain measurements were performed using the setup shown in Fig. 3.2.

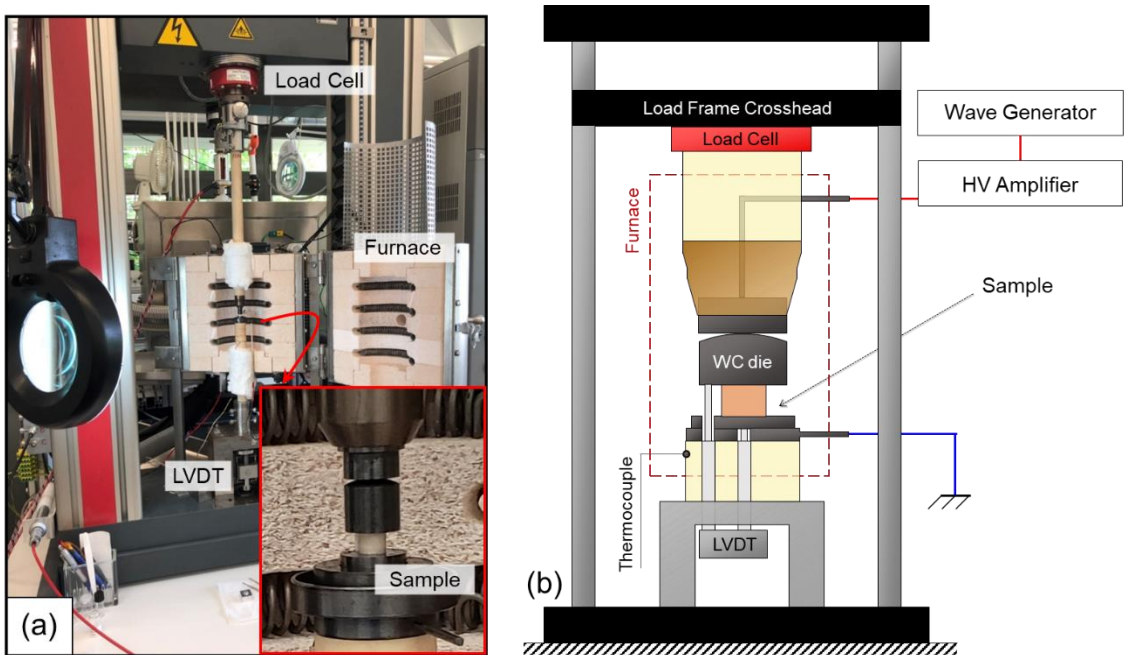

Figure 3.2: (a) Experimental setup for the stress−strain hysteresis measurement and temperature-dependent *S*−*E* hysteresis measurement under a compressive stress. (b) Schematic illustration of the measurement setup.

3.3 Cyclic unipolar fatigue test

The cyclic unipolar fatigue test was conducted according to the program shown in Fig. 3.3. Field heating and cooling were conducted to maintain the as-poled and fatigued state of the samples.

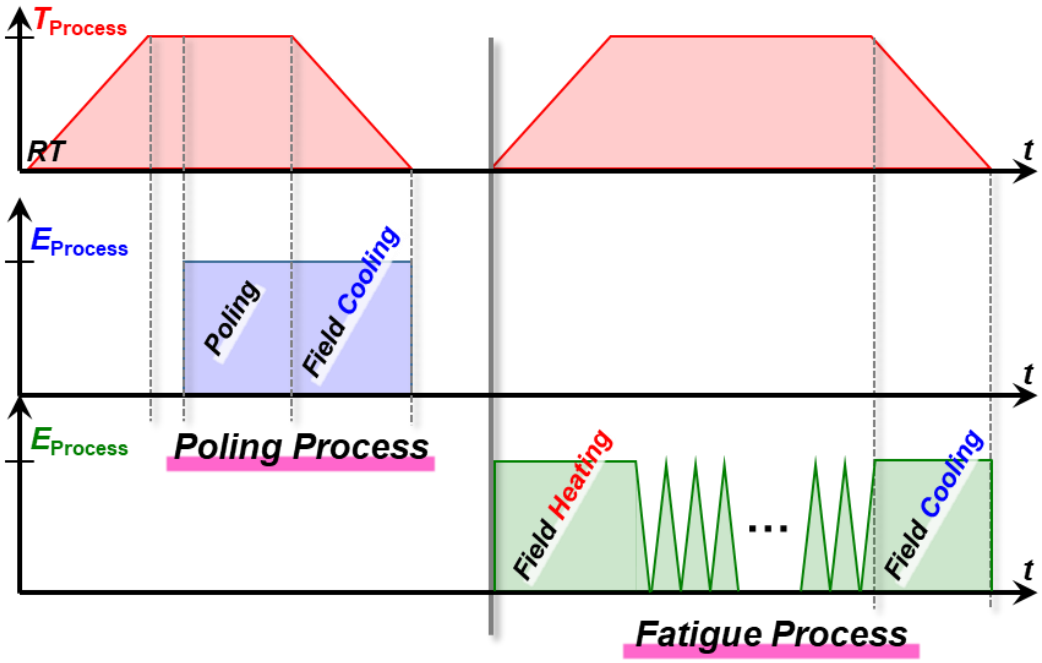

Figure 3.3: Temperature and electric field programs during the cyclic unipolar fatigue test.

3.4 Impedance spectroscopy

Impedance measurement was conducted using the measurement setup, as shown in Fig. 3.4. The detailed measurement conditions were summarized in Table 3.1 and 3.2. The frequency range of the impedance measurement was corresponded to the dipole and space charge polarization range in the dielectric dispersion (Fig. 3.5).

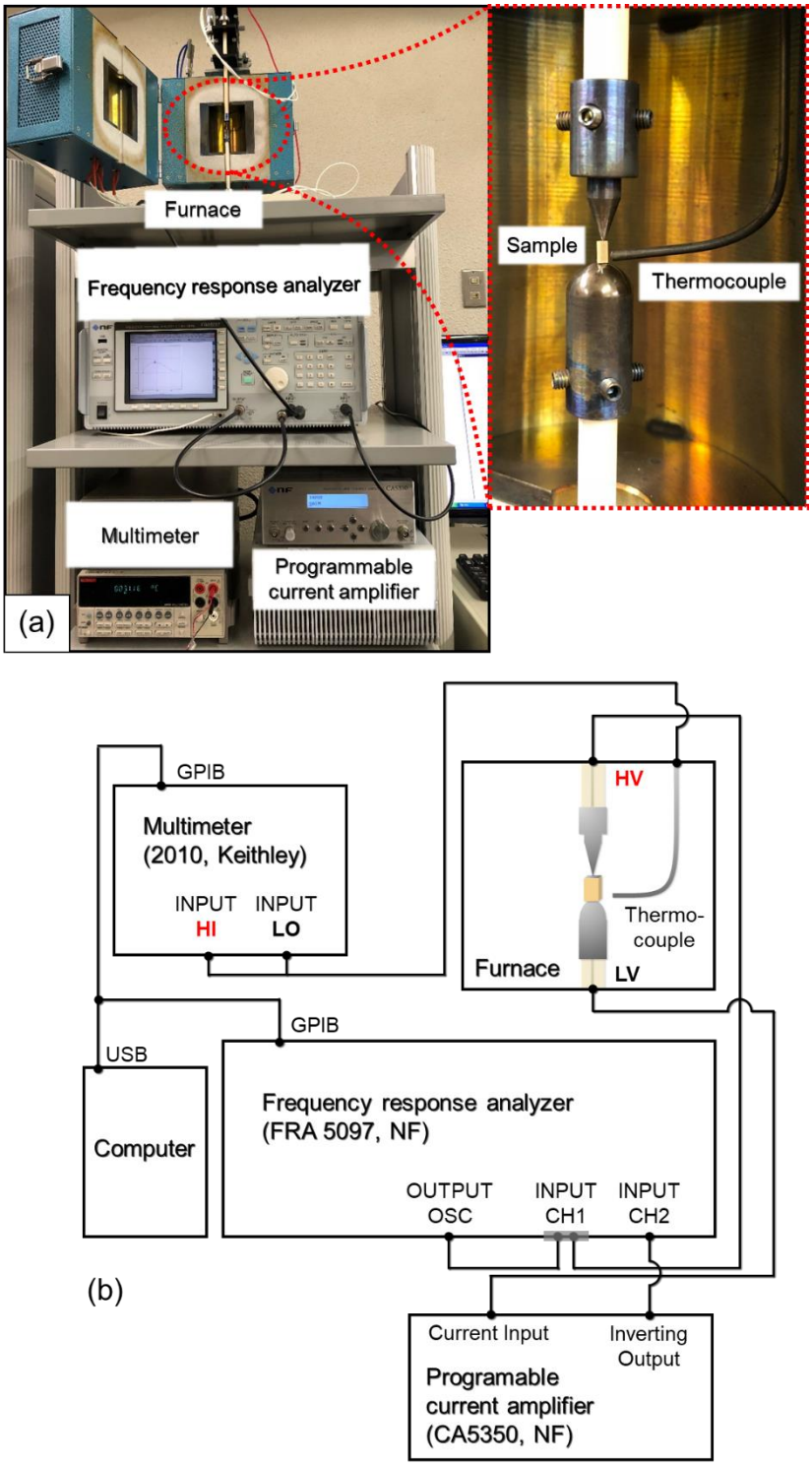

Figure 3.4: (a) Experimental setup for the impedance measurement. (b) Block diagram for the impedance measurement.

Table 3.1: Measurement conditions of the frequency response analyzer.

FRA CONDITION			
Amplitude	25.0 mVpeak	Open Correction	OFF
DC bias	0.00 V	Short Correction	OFF
Wave form	SINE	Measure Mode	CH1, CH2
Max Frequency	500 kHz	Coherence Mode	CH1 & CH2
Min Frequency	10 mHz	Weighing Factor CH1	1.0000E+00
Sweep Resolution Log	100 steps/sweep	Weighing Factor CH2	1.0000E-05
Integration Time	3 cycle	Invert	ON
Delay Time	0 cycle		

Table 3.2: Measurement conditions of the current amplifier.

CA CONDITION	
I/V Gain	10k
Gain	x10
Input	Rear

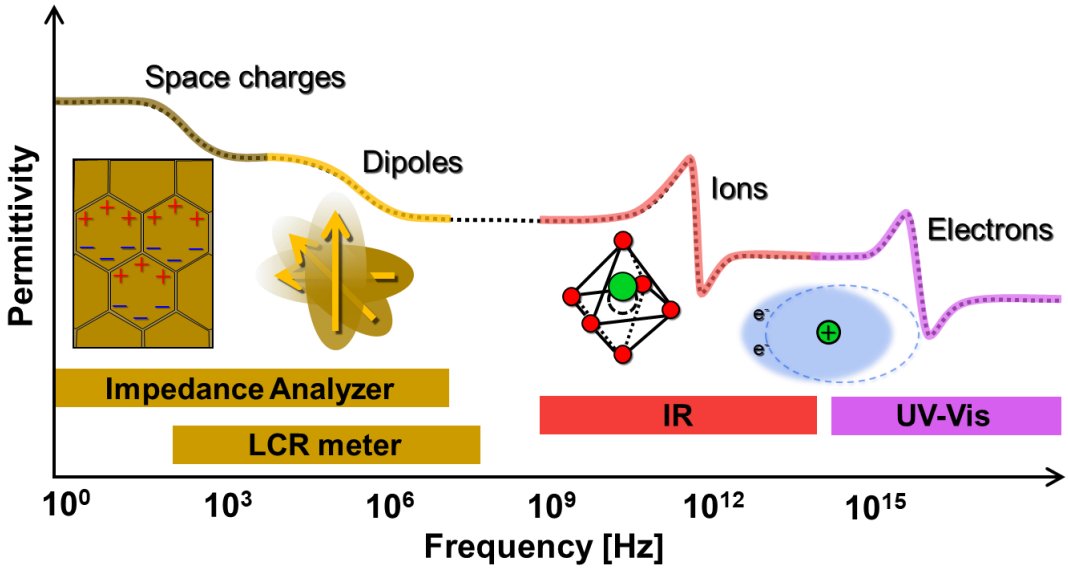

Figure 3.5: Schematic illustration of dielectric dispersion.

4. Alkali volatilization and susceptibility on ferroic properties

In this chapter, the alkali volatilization effect on the large-field ferroelectric and ferroelastic properties of (Li,Na,K)NbO_3-based piezoceramics was investigated. Regarding the defect structure of NKN, interactions of defect complexes and DWs in B-site acceptor doped NKN have been reported [65],[66], but the interaction of A-site vacancy caused by the alkali volatilization to ferroelectric and ferroelastic properties remains unclear. Hence, the alkali volatilization effect on the ferroelectric and ferroelastic properties was investigated.

4.1 Experimental procedure

$Li_{0.06}Na_{0.52}K_{0.42}NbO_3$ containing 0.65 mol% Li_2CO_3, 1.3 mol% SiO_2, 0.2 mol% $MnCO_3$, and 0.5 mol% $SrZrO_3$ (hereinafter LNKN6-a) piezoceramics were synthesized using a conventional sintering method described elsewhere [67]. According to the report, the microstructure of $Li_{0.06}Na_{0.52}K_{0.42}NbO_3$ can be manipulated by adding both Li_2CO_3 and SiO_2 compounds with an atomic ratio (Li/Si) of 1, resulting in lithium disilicate ($Li_2Si_2O_5$), which is a eutectic crystal. Furthermore, the addition of $MnCO_3$ and $SrZrO_3$ contributed to increased electrical resistivity. In order to introduce alkali deficiencies to LNKN6-a piezoceramics, the machined samples were post-annealed at the same sintering temperature for 2 h and 8 h. Disk samples (thickness: 0.5 mm, diameter: 10 mm) were used for *P*−*E* and *S*−*E* measurements, while cylindrical samples (thickness:

6.0 mm and diameter: 5.8 mm) were used for stress−strain measurements. After machining to the desired sample size, the surfaces were mirror-polished and subjected to post-annealing treatment. The final polishing step was performed with silica gel (OP-S silica colloidal suspension, Struers) for the microstructural observation images. The poling conditions were 3 kV/mm at 150 °C for 30 min in a thermostatic chamber. All samples, except for the polarized samples, were maintained at 600 °C for 3 h with heating and cooling rates of 5 °C/min and 1 °C/min, respectively [68]. This heat treatment was used before each electrical and mechanical test to eliminate residual stresses and ensure random domain distribution.

The crystal phases were measured by XRD (D8 ADVANCE Eco, Bruker) according to the $2\theta/\theta$ method from 20° to 60° at 25 °C. The microstructures of the sintered samples were analyzed using a scanning electron microscope (SEM; Quanta 200, FEI) with an energy-dispersive X-ray spectrometer (SEM-EDS). The polished surface of LNKN6-a piezoceramics was sputtered with gold and analyzed using SEM-EDS. The particle diameters on the ceramic surfaces were measured according to their Krumbein diameter (300 grains were counted for each sample) [39],[69]. EDS spot measurements were performed using an acceleration voltage of 20 kV [52],[70]. The spot size of the EDS measurement was ~7 μm, and measurements were taken by carefully targeting the center of the particle. Quantitative elemental analysis of Na, K, and Nb on the sintered samples was performed using an inductively coupled plasma optical emission spectrometer (ICP-OES; SPECTRO GENESIS, SPECTRO Analytical Instruments) [70].

P−*E* and *S*−*E* hysteresis loops were determined using a ferroelectric test system (TF Analyzer 2000, aixACCT). The post-annealed LNKN6-a piezoceramics before and after poling treatment were characterized for the hysteresis measurements. Three continuous bipolar waves were applied to the samples to obtain information of switchable domains from a closed hysteresis loop, then the change in polarization of the second bipolar wave was extracted [71],[72]. At the time bipolar *P*−*E* loops were measured, as-poled samples were set parallel and antiparallel to the poling direction to compare the internal bias field E_{bias}. The hysteresis measurements were conducted at room temperature with bipolar waves of 5 kV/mm at 1 Hz. In contrast, stress−strain hysteresis loops were characterized in an original setup: a screw-type loading frame equipped with a differential dilatometer and a heating furnace [73].

4.2 Results and discussion

4.2.1 Microstructure and chemical analysis

Figure 4.1 depicts the XRD patterns of post-annealed LNKN6-a piezoceramics. According to previous reports, this material shows a phase coexistence between the monoclinic (Pm) and tetragonal ($P4mm$) phases [47],[48]. All samples showed perovskite-type reflections, indexed with a pseudocubic parent cell and denoted with a subscript pc. No secondary phases were detected, even for the post-annealed samples. Besides the phase composition, changes in the microstructure can influence the electrical and mechanical properties of piezoceramics. For that reason, the microstructural images and grain size

distributions of LNKN6-a are shown in Figure 4.2. Upon increasing the annealing time to 8 h, the median diameter d_{50} increased from 4.34 μm to 6.38 μm [Fig. 4.2(d) and 4.2(f)]. The distribution shape of the as-sintered sample was unimodal, while the distribution of the sample annealed for 8 h was bimodal due to the abnormal grain growth during the post-annealing process [51].

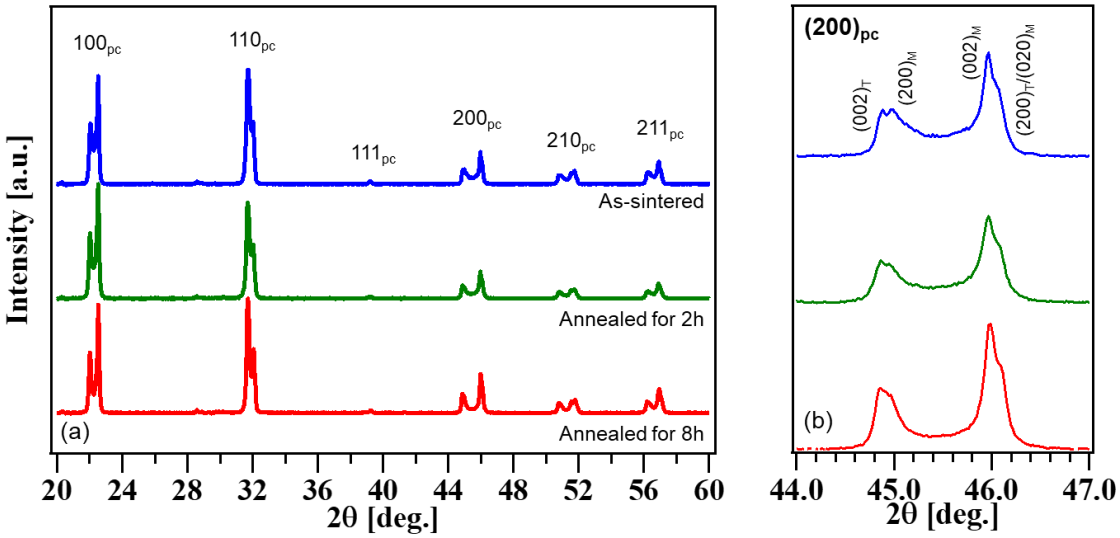

Figure 4.1: (a) Post-annealing dependent XRD profiles of LNKN6-a piezoceramics. (b) $(200)_{pc}$ reflections of LNKN6-a piezoceramics. (Reprinted with permission from [74]. Copyright 2021 © The Ceramic Society of Japan.)

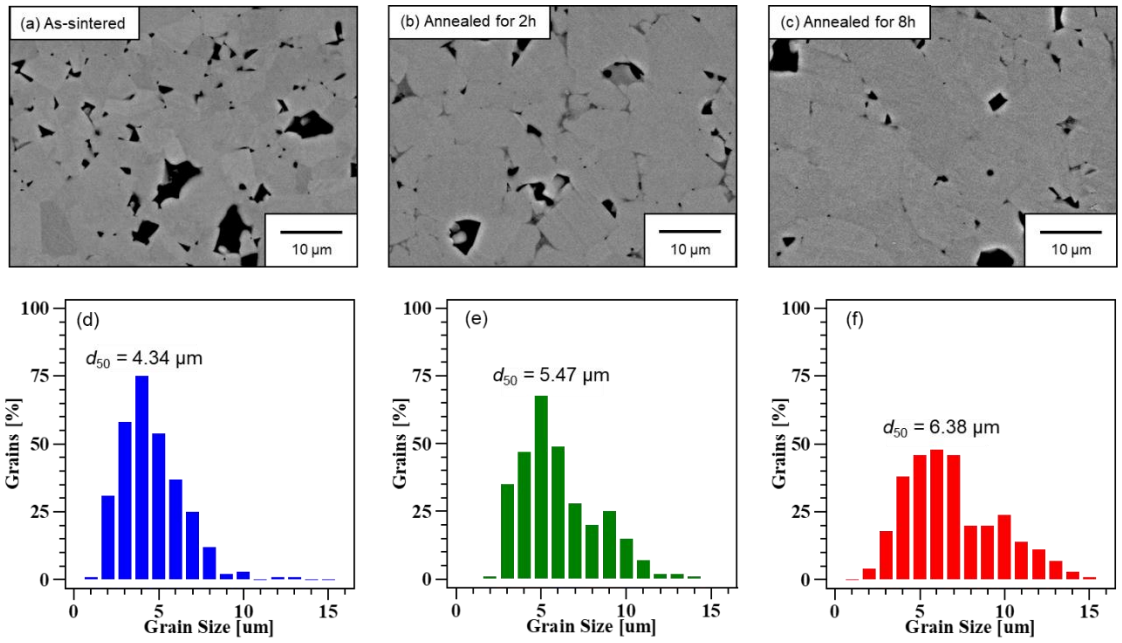

Figure 4.2: Microstructure of LNKN6-a piezoceramics. Backscattering images of various samples: (a) as-sintered, (b) annealed for 2 h, and (c) annealed for 8 h. Grain size distribution of (d) as-sintered, (e) annealed for 2 h, and (f) annealed for 8 h samples; 300 grains were measured for each sample by Krumbein method [69]. (Reprinted with permission from [74]. Copyright 2021 © The Ceramic Society of Japan.)

ICP-OES and EDS point analyses were conducted to investigate the chemical composition of the post-annealed samples. Figure 4.3 shows the results of ICP-OES analysis on Na, K, and Nb of the as-sintered and the annealed samples. Here, Nb was considered a non-volatile ion, so the (Na+K)/Nb ratio was calculated. The atomic number ratio of Na/Nb and K/Nb in the as-sintered state was almost the same as the nominal composition [75], while Na/Nb and K/Nb decreased slightly by 0.12 and 0.08 in the sample annealed for 8 h. As a result,

the atomic number of (Na+K)/Nb in the sample annealed for 8 h was lower than the nominal composition by 0.02. However, the sample annealed for 2 h exhibited the opposite behavior. In the ICP-OES analysis, crushed powders from the cylinder-type samples were used. Therefore, assuming that alkali volatilization proceeded from the sample surfaces, the volatilization effect on the ICP results may be weakened. Figure 4.4 shows the EDS point analysis results of LNKN6-a piezoceramics. The atomic number ratio of (Na+K)/Nb was lower than its nominal composition by ~0.15 for each condition. The detection sensitivity of sodium deteriorates when the excitation voltage is as high as 20 kV [70],[76]. Therefore, we could not conclude that the gap from the nominal composition of (Na+K)/Nb was due to alkali volatilization. On the other hand, the atomic number ratio of O/Nb gradually decreased from 2.70 for the as-sintered state to 2.36 for the sample annealed for 8 h. This decrease suggests that alkali volatilization mainly occurred on the sample surface during the post-annealing process, leaving oxygen vacancies that were generated due to the volatilization of sodium and potassium as Na_2O and K_2O, respectively [51]. The results of ICP-OES and EDS point analysis showed that alkali volatilization occurred on the sample surface, but did not proceed to the deep interior of the sample, as previously reported [77].

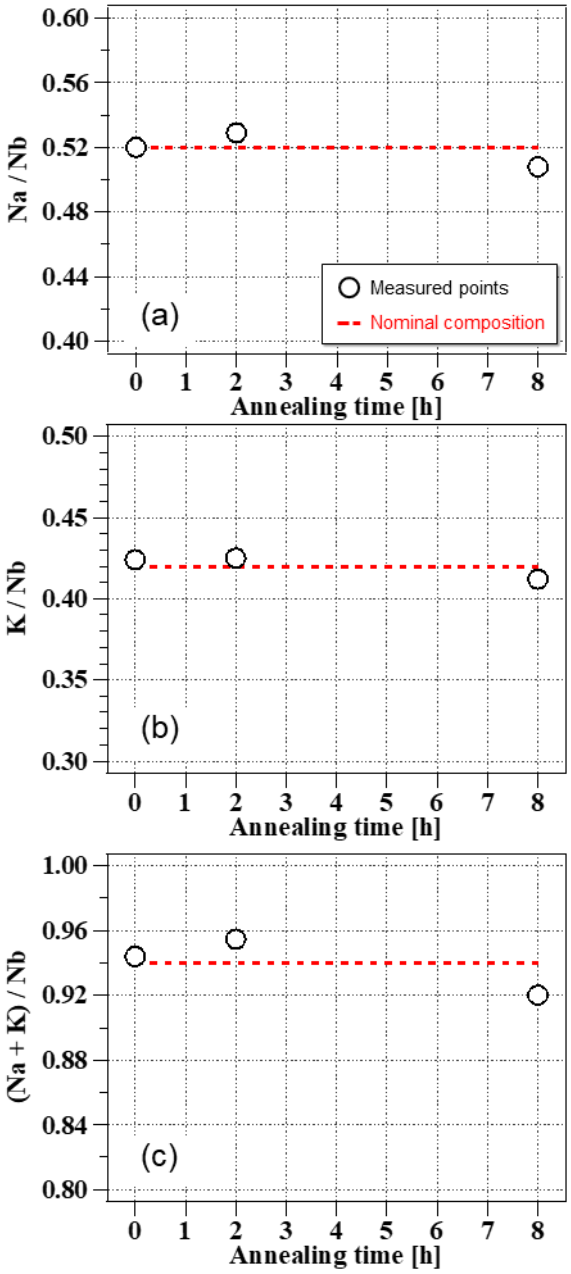

Figure 4.3: ICP analysis results of LNKN6-a piezoceramics: (a) Na/Nb, (b)K/Nb, and (Na+K)/Nb on as-sintered, annealed for 2 h, and annealed for 8 h. The nominal composition is denoted by red dashed lines. (Reprinted with permission from [74]. .)

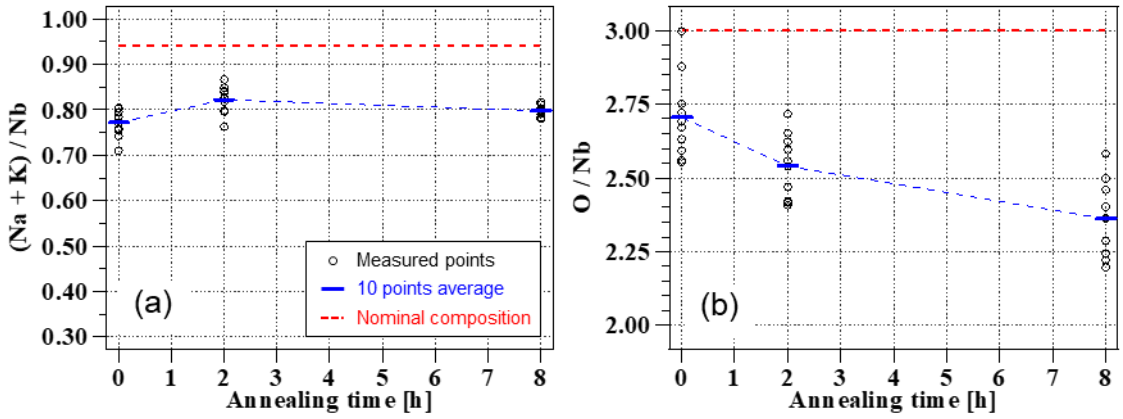

Figure 4.4: EDS point measurement results at the grains of LNKN6-a piezoceramics: as-sintered, annealed for 2 h, and annealed for 8 h. Measurements were conducted 10 times for each condition. Averages of these 10 points and the nominal composition are denoted by blue and red lines, respectively. (Reprinted with permission from [74]. Copyright 2021 © The Ceramic Society of Japan.)

4.2.2 Electrical and mechanical properties

Changes in the microstructure were observed; thus, alternations in the electrical and mechanical properties were expected. Figure 4.5 depicts the *P*–*E* and *S*–*E* hysteresis loops of post-annealed LNKN6-a piezoceramics. As the annealing time increased from 0 h to 8 h, the remanent polarization $2P_r$ decreased from 48.5 μC/cm^2 to 35.6 μC/cm^2, and the coercive field $2E_C$ increased from 3.6 kV/mm to 3.8 kV/mm, respectively (Fig. 4.5(a) and 4.5(b)). In addition to these electrical hardening behaviors, there were two switching currents in the annealed samples. One peak was observed at 1.4 kV/mm in the as-sintered and annealed samples, while the other was observed at > 3.5 kV/mm in the annealed samples,

but not in the as-sintered sample. Bipolar *S*−*E* loops of post-annealed LNKN6-a piezoceramics are shown in Fig. 4.5(c). The butterfly curve of the as-sintered sample was relatively sharp compared to the sprout-shaped curves of the annealed samples, which were observed in relaxor materials [30]. To characterize this difference in shape, two parameters were characterized as the peak-to-peak strain S_{p-p} and the crossing field at zero strain E_X^+. The electromechanical hardening behavior was obtained when S_{p-p} decreased from 0.260% to 0.211%, the annealing time increased from 0 h to 8 h, and E_X^+ increased from 2.38 kV/mm in the as-sintered sample to 2.83 kV/mm in the sample annealed for 8 h, thus changing the shape from butterfly to sprout.

The polarization reversal current peak was separated, and *S*−*E* loops changed from butterfly-shaped to sprout-shaped loops in LNKN6-a piezoceramics. There are three possibilities for these hardening behaviors. First, the microstructural change has an effect on the post-annealed LNKN6-a piezoceramics. The average grain size of as-sintered LNKN6-a piezoceramics was optimized to 3 μm [39] based on a report that the piezoelectric d_{33} constant of LNKN piezoceramics exhibited a maximum with a grain size of 3 μm [78],[79]. Although previous reports state that grains larger than this optimum size result in a smaller coercive field E_C [78],[80], the opposite was true in post-annealed samples; E_C increased with larger grains. Therefore, the microstructural effect on the hardening behavior was considered as a minor impact in this case. Second, the $MnCO_3$ sintering additive could function as an acceptor substituting Nb^{5+} for Mn^{2+} in the B-site, thus forming an acceptor ion Mn_{Nb}'''. If it was formed, dimetric $(V_O^{\cdot\cdot} - Mn_{Nb}''')'$ and/or trimetric $(V_O^{\cdot\cdot} - Mn_{Nb}''' - V_O^{\cdot\cdot})^{\cdot}$ defect association, that could

have performed as hardener. However, the scanning transmission electron microscopy (STEM) analysis result demonstrated that MnO segregated on the GB and hardly reacted with LNKN at 1000 °C [39]. Therefore, this is also not considered to be the dominant factor in hardening behavior.

The last and most promising theory is the change in the phase ratio around the PPT region caused by alkali volatilization. Figure 4.6 depicts the temperature-dependent permittivity of LNKN6-a piezoceramics. Based on the linear extrapolations in Fig. 4.6(b), the T_{PPT} of the as-sintered sample was 49.4 °C. This material was designed to have a T_{PPT} of ~50 °C [39],[48],[68]; however, the temperature decreased to 36.6 °C with inappropriate thermal treatment. Thus, the phase-coexistent region approached room temperature and presumably resulted in an increased tetragonal phase ratio. With regard to the phase coexistence, Zhao et al. [81] reported the E_C of Er^{3+}-doped $Li_x(Na_{0.48}K_{0.52})_{1-x}NbO_3$ piezoceramics in the vicinity of the phase-coexistent composition: the E_C of the orthorhombic phase was 1.43 kV/mm (x = 0), while that of the tetragonal phase was 2.12 kV/mm (x = 0.08). In particular, the E_C of the phase-coexistent composition (x = 0.06) exhibited the highest value (2.35 kV/mm). It is suggested that the increase in E_C and the split of the polarization reversal current observed in the post-annealed LNKN6-a piezoceramics was due to the phase coexistence region.

Another evidence of the compositional fluctuation on the annealed LNKN6-a was the permittivity change. The dielectric anomalies in the heating process from the tetragonal to the cubic phase are shown in Fig. 4.6(c). The Curie temperature T_C were shifted from 451.0 °C in the as-sintered state to 454.5 °C

in the 8 h annealed state. At the same time, T_{PPT} shifted from 49.4 °C to 36.6 °C, as mentioned above. This symmetric shift is peculiar in Li-modified NKN [38]; therefore, Na and K were considered as volatilized candidates in the post-annealing process. On the other hand, the T_C of the polished sample that was originally post-annealed for 8 h shifted back to 451.8 °C. According to a previous report, the alkali volatilization had a depth profile up to 55 μm determined by Raman spectroscopy [77]. Based on this report, the alkali volatilization of the T_C shift suggested that the alkali volatilization had a depth profile and did not exceed 75 μm from each surface of the disk sample. This further supports the results received from the ICP-OES and EDS spot analyses.

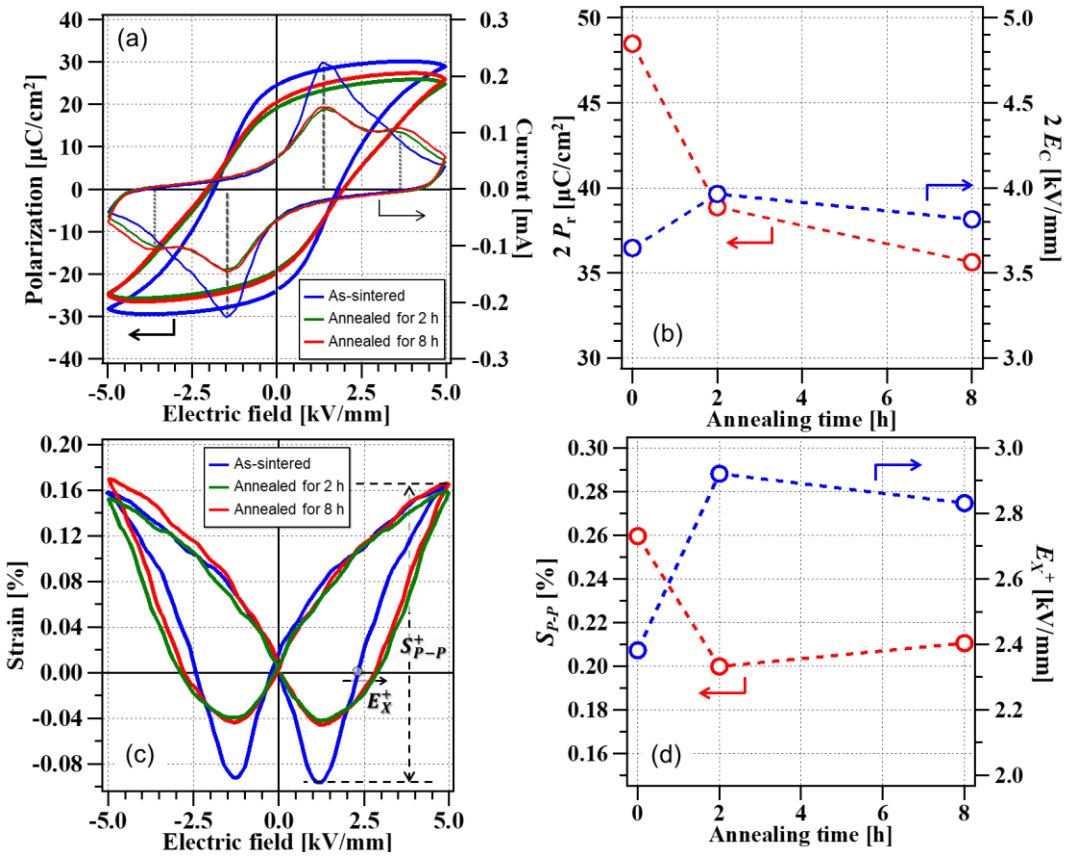

Figure 4.5: (a) *P*−*E* hysteresis loops of LNKN6-a piezoceramics before the poling treatment. (b) Annealing time dependence of coercive field $2E_C$ and remanent polarization $2P_r$. (c) *S*−*E* hysteresis loops of LNKN6-a piezoceramics before the poling treatment. (d) Annealing time dependence of the peak-to-peak strain S_{p-p} and crossing field at zero stress E_X^+. (Reprinted with permission from [74]. Copyright 2021 © The Ceramic Society of Japan.)

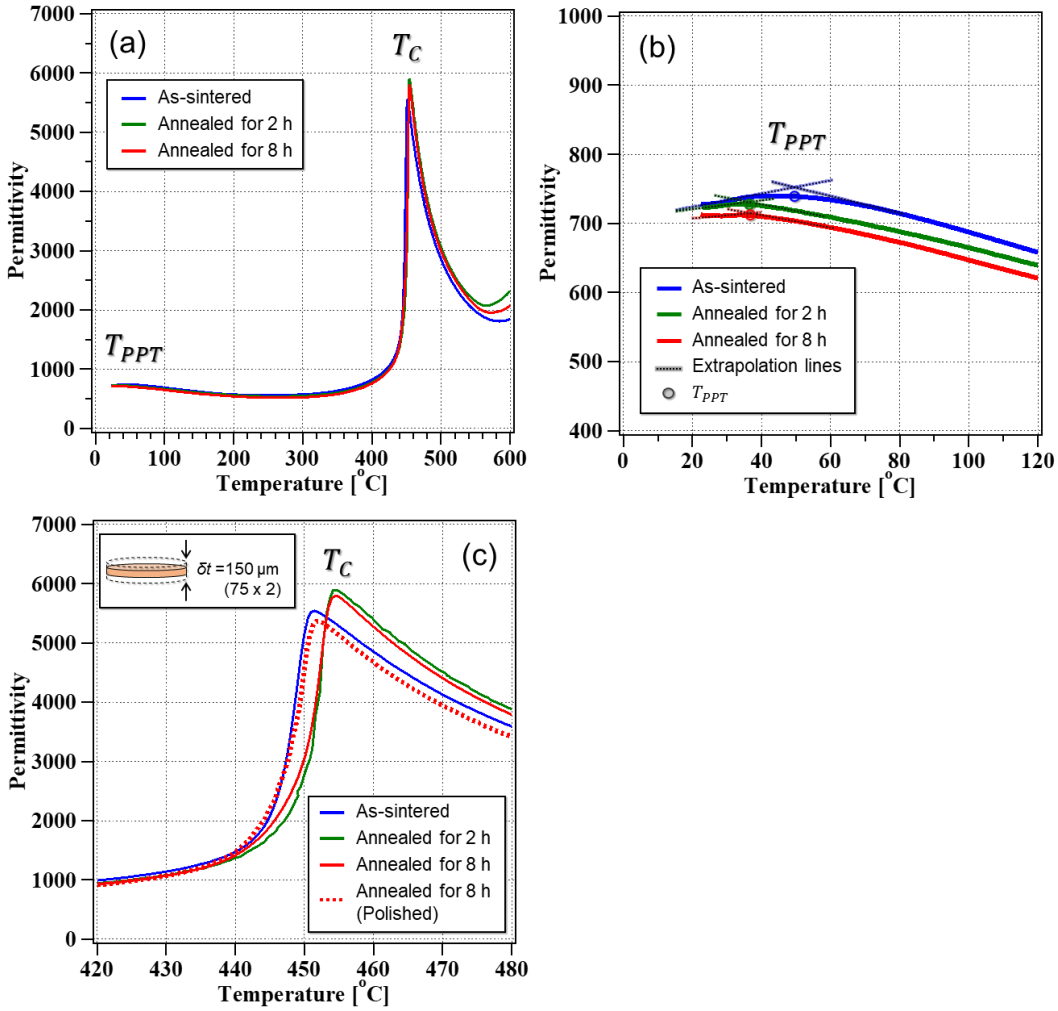

Figure 4.6: (a) Temperature-dependent permittivity change in post-annealed LNKN6-a piezoceramics. (b) Magnified view of the permittivity changes around T_{PPT}. T_{PPT} estimated from linear extrapolations shown as dotted lines. (c) The Curie temperature T_C at the phase transition from the tetragonal to the cubic phase is shown. In addition to the post-annealing dependence of the permittivity, the result for the sample annealed for 8 h, which was polished by 75 μm from both sides of the surface, is shown. (Reprinted with permission from [74]. .)

Figure 4.7 depicts the *P*−*E* hysteresis loops of the as-poled LNKN6-a piezoceramics. The bipolar *P*−*E* loops that were characterized as parallel and antiparallel to the poling direction shifted to the left and right sides, respectively. These shifts from the zero point are defined as the internal bias field E_{bias} $\{= (E_C^+ - |E_C^-|)/2\}$ [25],[82],[83], where E_C^+ and E_C^- are the coercive fields on the positive and negative sides of the *P*−*E* loops, respectively. When the annealing time increased from 0 h to 8 h, the values of E_{bias} increased from −0.73 to −0.91 kV/mm in the parallel direction and from 0.53 to 0.71 kV/mm in antiparallel direction. This anisotropic change in the E_{bias} is due to the existence of defect associations between alkali deficiencies V_M' (M = Li, Na, K) and oxygen vacancies $V_O^{\cdot\cdot}$ [84]. As the post-annealing time increased, the amount of the associated defects of V_M' and $V_O^{\cdot\cdot}$ increased, which hindered the transformation of the domain structure [85]. This hardening effect could be smaller than the effect of B-site substitution because the associated defects of V_M' and $V_O^{\cdot\cdot}$ were weakly bound [86]. The increased E_{bias} in the annealed samples may be attributed to the increase in the A-site defect associations based on the switchability of the E_{bias}.

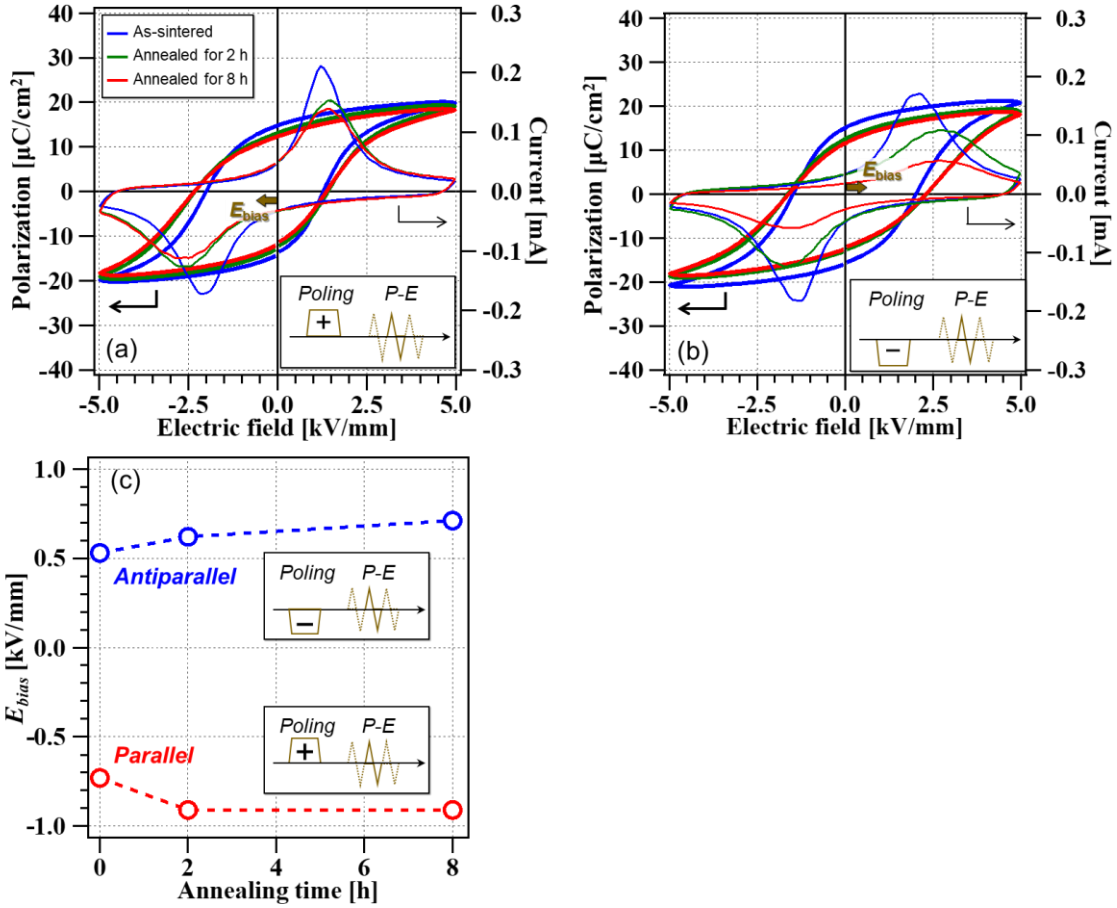

Figure 4.7: *P*−*E* hysteresis loops of LNKN6-a piezoceramics after the poling treatment. (a) *P*−*E* loops measured toward the parallel direction of the poling treatment. (b) *P*−*E* loops measured toward the antiparallel direction of the poling treatment. (c) Post-annealing time dependence of the internal bias E_{bias} and its capability of switching. (Reprinted with permission from [74]. Copyright 2021 © The Ceramic Society of Japan.)

Figure 4.8(a) depicts the stress−strain hysteresis loops of as-sintered LNKN6-a piezoceramics in a solid line. The inset schematically depicts the domain structures at labeled positions [87]. The sequence symbols from (I) to (IV) represent different domain states. The as-sintered material initially had a randomly oriented domain structure (I). Upon compressing, the strain increased

linearly at first. Further application of compressive stress changed the strain response to nonlinear behavior. The strain continued to increase nonlinearly with further compression, until all ferroelastic domains available for reorientation had been ferroelastically switched to the in-plane direction. The inflection point during the loading process (II) is defined as coercive stress σ_C, which is analogous to the poling field E_{pol} in *P*−*E* hysteresis loops [88],[89]. Most domains were switched during the application of coercive stress σ_C. At the maximum stress level (III), no additional domains were reoriented, and the material response in the vicinity of the point was again linear elastic. Upon unloading, the initially linear elastic material toward ideal strain S_i began to exhibit nonlinearity with decreasing compressive stress. This nonlinearity in the unloading process was due to the release of constraint forces toward the in-plane direction. Notably, the sample did not return to its initial state (IV≠I) because not all of the domains switched back to the initial state, thus resulting in a remanent strain S_r. Additionally, the second stress−strain loop was also shown in Fig. 4.8(a) (dotted lines). The second loop trajectory in the loading process differed from the first stress−strain loop (solid lines) because most of the switchable domain were already mechanically poled to the in-plane direction during the first loop. In contrast, the unloading process of the second stress−strain loop was matched to the first loop, indicating that the ferroelastic domain had sufficiently oriented in the first loop, then no further orientation had occurred in the second loop.

Figure 4.8(b) and 4.8(c) show the annealing time-dependent stress−strain loops of LNKN6-a piezoceramics and the coercive stress σ_C and domain backswitching η_B $(= 1 - S_r/S_i)$. The coercive stress σ_C increased from

−123.1 MPa to −139.5 MPa and the domain backswitching η_B increased from 48.8% to 57.6%, respectively. Although there seemed to be some hardening in the average values, the stress−strain hysteresis loops did not exhibit significant changes in these ferroelastic properties. This difference in susceptibility is most likely due to the difference in the volume ratio of the samples used in the ferroelectric and ferroelastic measurements. The cylindrical shape used for measuring ferroelastic properties was presumably less affected by alkali volatilization, which only occurs on the surface, than the disk shape used for measuring ferroelectric properties.

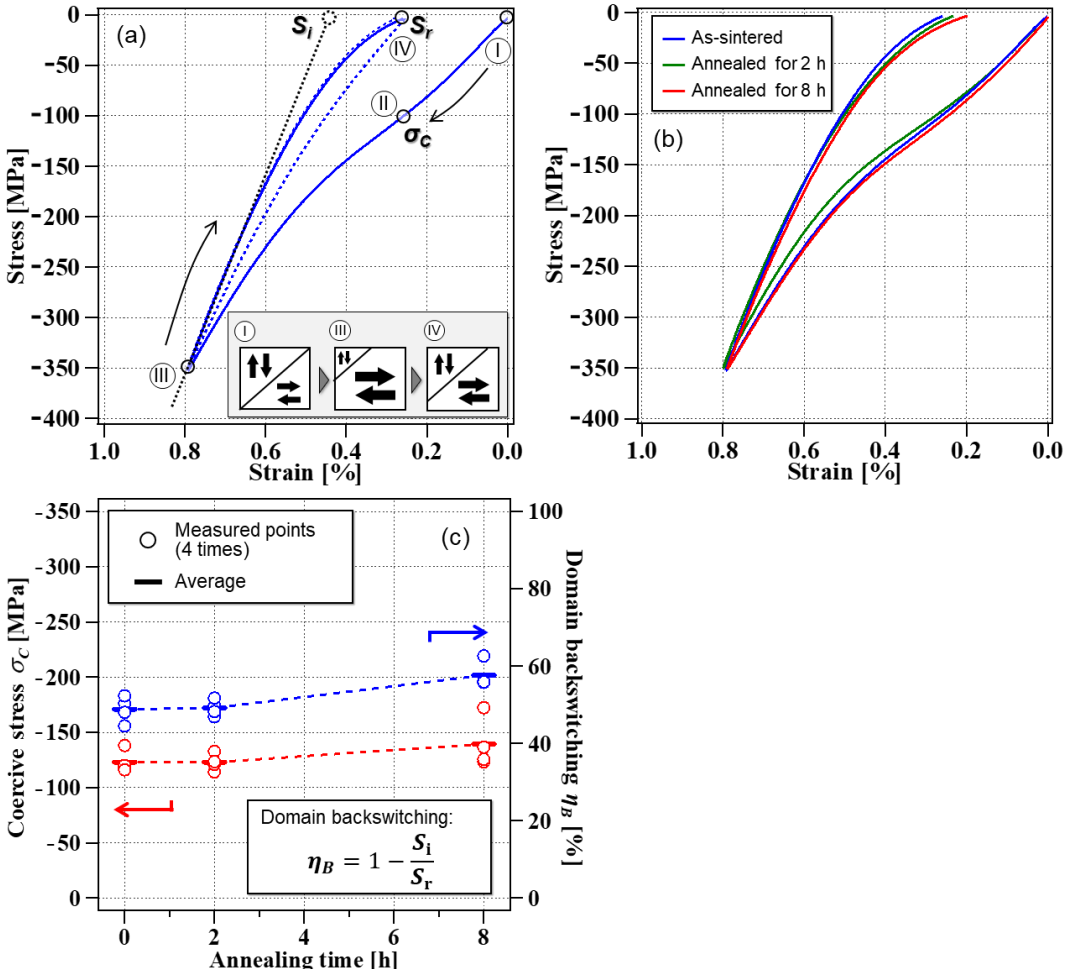

Figure 4.8: (a) Stress−strain hysteresis loops of as-sintered LNKN6-a piezoceramics. The first and second loops are denoted by blue solid and dotted lines, respectively. The arrows indicate the measurement direction. The black dotted line represents the tangent line of the stress−strain curve on unloading at point III. (b) Representative stress−strain behavior of LNKN6-a piezoceramics. (c) Annealing time dependence of the ferroelastic parameters: coercive stress σ_C and domain backswitching η_B. Measurements were conducted four times for each condition to verify the repeatability. (Reprinted with permission from [74]. .)

4.3 Conclusion

In this study, the alkali volatilization effect on the ferroelectric and ferroelastic properties of LNKN6-a piezoceramics was investigated. Alkali volatilization was performed by exposing the specimens to the sintering temperature for up to 8 h. Alkali volatilization was analyzed by SEM-EDS and ICP-OES. The annealed samples exhibited reduced remanent polarization $2P_r$ and enhanced coercive E_C and internal bias E_{bias} fields, suggesting that the annealed sample had an electrical hardening effect. The switchability of the polarity of E_{bias} according to the poling direction suggested that there were several types of associated defects. Conversely, stress−strain hysteresis revealed that coercive stress σ_C and domain backswitching η_B did not significantly change, which suggested that the mechanical properties did not exhibit hardening effects. In light of the above, we concluded that alkali volatilization affected ferroelectric properties, but did not significantly affect the ferroelastic properties because alkali volatilization proceeded from the surface of the samples.

5. Electric-field-induced strain of multilayered piezoceramics under compressive stress

In this chapter, the stress-dependent electric-field-induced strain of (Li,Na,K)NbO_3-based ML piezoceramics is characterized. Large-field properties under uniaxial mechanical preloading are essential to evaluate actuation performance because preloading is applied to most ML piezoceramics to prevent the layered structure from cracking [90]–[92]. However, these types of studies have not been reported for LNKN. Investigation of the mechanical load-dependent electromechanical properties is important, particularly for PZT [71],[93], BNT-6BT [94],[95], and BCZT [96] piezoceramics, because a maximum electric-field-induced strain can be achieved at moderate stress levels. This is due to the additional switching of the in-plane aligned non-180° domains. Among them, the stress-dependent electromechanical properties of BCZT ferroelectrics, which also exhibit a PPT region in the vicinity of room temperature, is highly dependent on the vicinity of the ferroelectric-to-paraelectric phase transition temperature T_C [96]. In the case of LNKN (x = 0.06), the polymorphic phase transition temperature (T_{PPT}) is approximately room temperature, whereas T_C is > 400 °C. This wider separation suggests a more pronounced influence of the PPT. Therefore, the large-signal unipolar behavior of application-relevant lead-free LNKN-based ML piezoceramics under uniaxial compressive stress was investigated.

5.1 Experimental procedure

5.1.1 Materials

$Li_{0.06}Na_{0.52}K_{0.42}NbO_3$ + 0.65 mol% Li_2CO_3 + 1.3 mol% SiO_2 + 0.2 mol% $MnCO_3$ + 0.5 mol% $SrZrO_3$ ML piezoceramics (LNKN6-a ML) were prepared. The preparation process of the ML is detailed in a previous report [67]. Figure 5.1 depicts a cutaway view of LNKN6-a ML. The Pd inner electrodes were screen printed on green sheets and stacked into a structure containing 55 ceramic and 56 inner electrode layers. The dimensions of the ML samples were 5.0 mm × 3.6 mm × 5.0 mm (length × height × width) and the ceramic layer thickness was ~50 μm. The side margin and the cover layer thickness were 504 μm and 370 μm, respectively [Fig. 5.1(a)]. Terminal electrodes were formed by firing silver paste, then sputtering platinum onto the surface of the silver surface. Additionally, the sputtered platinum electrodes were extended to the largest faces perpendicular to the longitudinal direction. This enabled the application of a combined electromechanical loading, whose electric field was parallel to the compressive stress [Fig. 5.1(b)]. Finally, high-temperature silicon paste was placed onto the terminal electrodes to avoid short circuits. Figure 5.1(c) depicts the cross-sectional face, which is indicated by the parallelogram enclosed with dotted lines in Fig. 5.1(b). Few pores were observed in the piezoceramic layer, and the internal electrodes were sufficiently attached to the piezoelectric layers [Figs. 5.1(d, e)]. Figure 5.2 shows the ML structure taken from the mirror-polished surface of the LNKN6-a ML. The side margins and cover layers of the ML were 504 μm and 370 μm, respectively.

LNKN6-a bulk ceramics were synthesized by a conventional sintering method to compare the properties of the bulk and ML materials. The preparation process of LNKN6-a bulk ceramics is detailed in a previous report [39]. Disk samples (thickness: 0.5 mm and diameter: 10 mm) were prepared. The poling condition of the bulk and ML samples was 3 kV/mm at 100 °C in a thermostatic chamber.

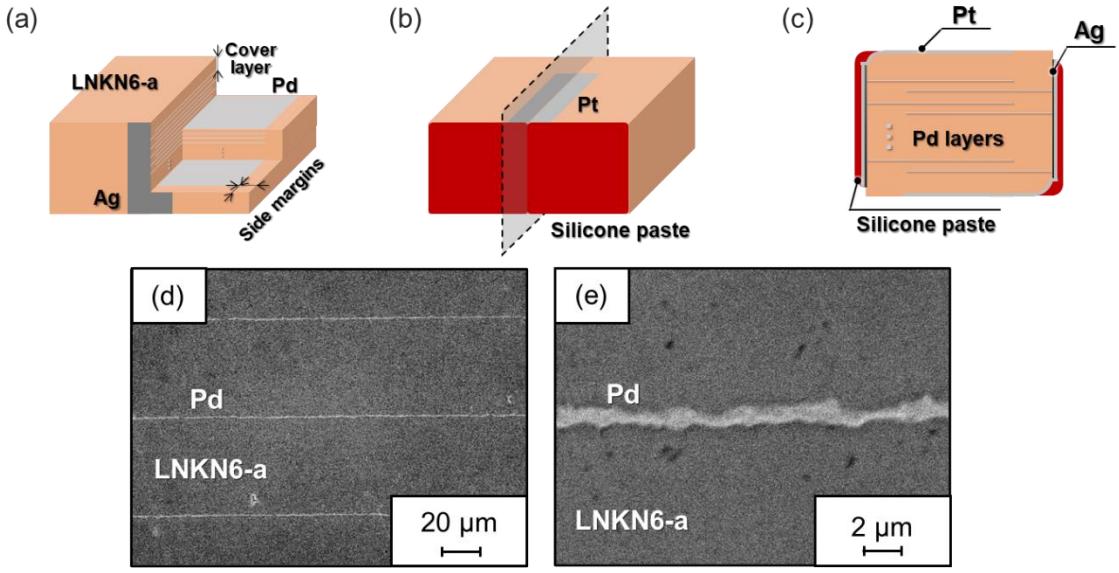

Figure 5.1: Schematic of the (a) multilayered structure of LNKN6-a ML, (b) external view of the multilayer, (c) cross-sectional view of the multilayer. (d) SEM image of a cross-sectional plane of the multilayer. (e) Magnification of image (d) around the Pd internal electrode. (Reprinted with permission from [97]. Copyright 2020 © AIP Publishing.)

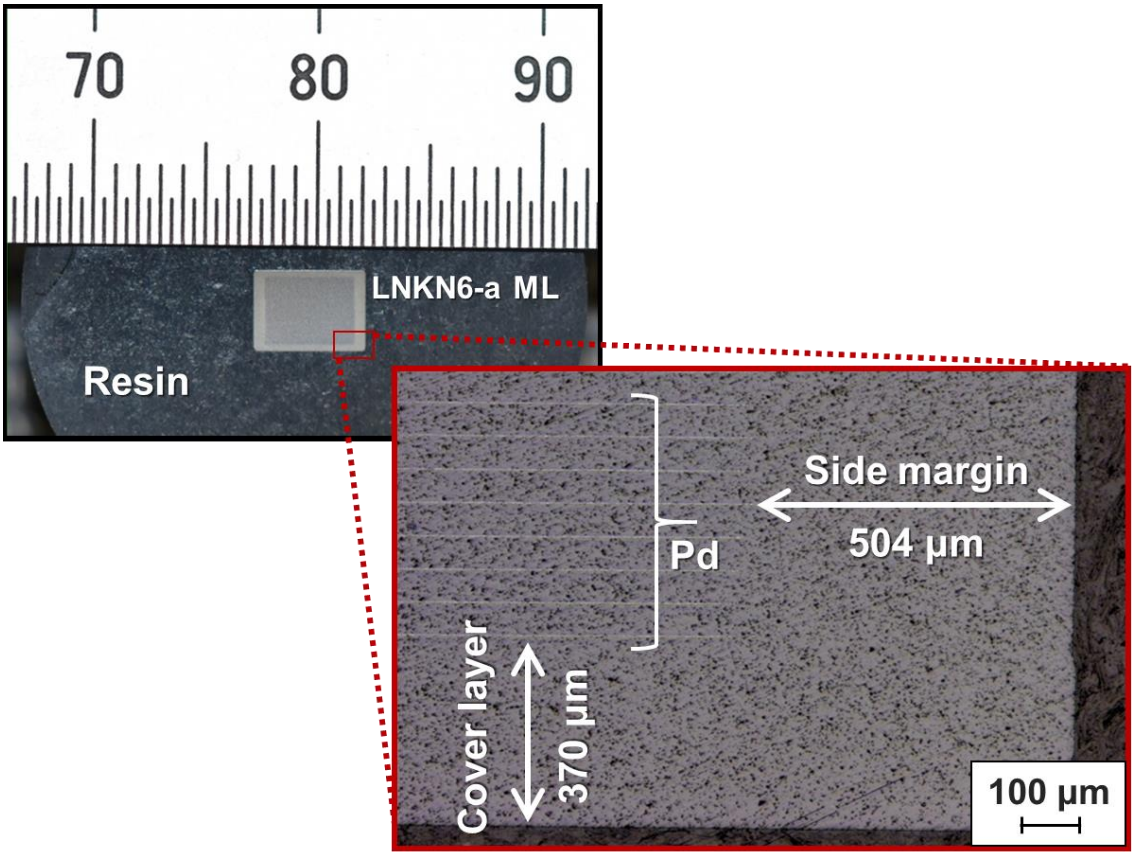

Figure 5.2: Mirror-polished surface of the LNKN6-a ML. The side margins and the cover layers are 504 µm and 370 µm, respectively.

5.1.2 Characterization

Permittivity was characterized at 1 kHz using a precision LCR meter (E4980AL, Keysight Technologies). A heating rate of 2 °C/min was used during measurement of the temperature-dependent permittivity. Stress−strain hysteresis loops were measured using a custom-built setup, consisting of a screw-type loading frame equipped with a differential dilatometer and a heating furnace. A conical loading bearing was placed on the top of the ML, creating a point contact with the indenter to prevent eccentric loading on the specimen. Webber et al. detailed the measurement technique and the test setup [73]. The stress−strain loop and the

stress−polarization change during the loading process were characterized up to −350 MPa at 25 °C. Electric-field-induced strain measurements were conducted with two experimental setups. The first was a laser displacement meter attached to the ferroelectric test system (TF Analyzer 2000, aixACCT) to determine the displacement under zero stress. The second was the abovementioned dilatometer to apply a high compressive stress to the MLs during the electrical field application. A signal generator (33220A, Keysight Technologies) and high voltage amplifier (623B, TREK, Inc.) were connected to the loading frame to apply large electric fields. Three consecutive unipolar triangular waveforms of 10 mHz were selected as the input signal for characterizing the sample strain. The input signal contained nine subsequent cycles, three cycles for each field of 2 kV/mm, 4 kV/mm, and 6 kV/mm, respectively; the second cycle of each field was used for analysis to obtain a closed hysteresis loop [71]. The stress levels ranged from −5 MPa, which was the minimum level required to make contact, to −200 MPa. During each *S*−*E* measurement, stress levels were kept constant.

5.2 Results and discussion

Figure 5.3 depicts the temperature-dependent permittivity of the as-sintered and as-poled LNKN6-a piezoceramics. The as-poled LNKN6-a ML had a T_C at 452 °C owing to the phase transition from a tetragonal ($P4mm$) to a cubic ($Pm\bar{3}m$) phase (Fig. 5.3(a)) [38]. On the other hand, a hump in the permittivity was observed at 39.8 °C and 68.1 °C for the as-sintered and as-poled LNKN6-a ML, respectively (Fig. 5.3(b)). This hump can be attributed to the PPT from the lower symmetry monoclinic (Pm) to the aforementioned tetragonal phase [38].

Interestingly, the T_C of the ML is influenced by the poling process; however, the T_{PPT} shifted to a higher temperature by ~30 °C owing to the poling procedure. There is no direct experimental evidence of the origin of such a large shift in T_{PPT}; however, the change in phase fraction due to the electric-field-induced phase transformation may influence the stability of the T_{PPT} [47]. Furthermore, the T_{PPT} of the as-sintered LNKN6-a bulk ceramic is 49.4 °C, which is higher than the as-sintered LNKN6-a ML by approximately 10 °C [48]. The difference between the T_{PPT} in the bulk and ML can arise due to co-firing with the electrodes, which causes internal stress in the material. As reported previously, mechanical stress can change the phase fraction in NKN-based materials [48].

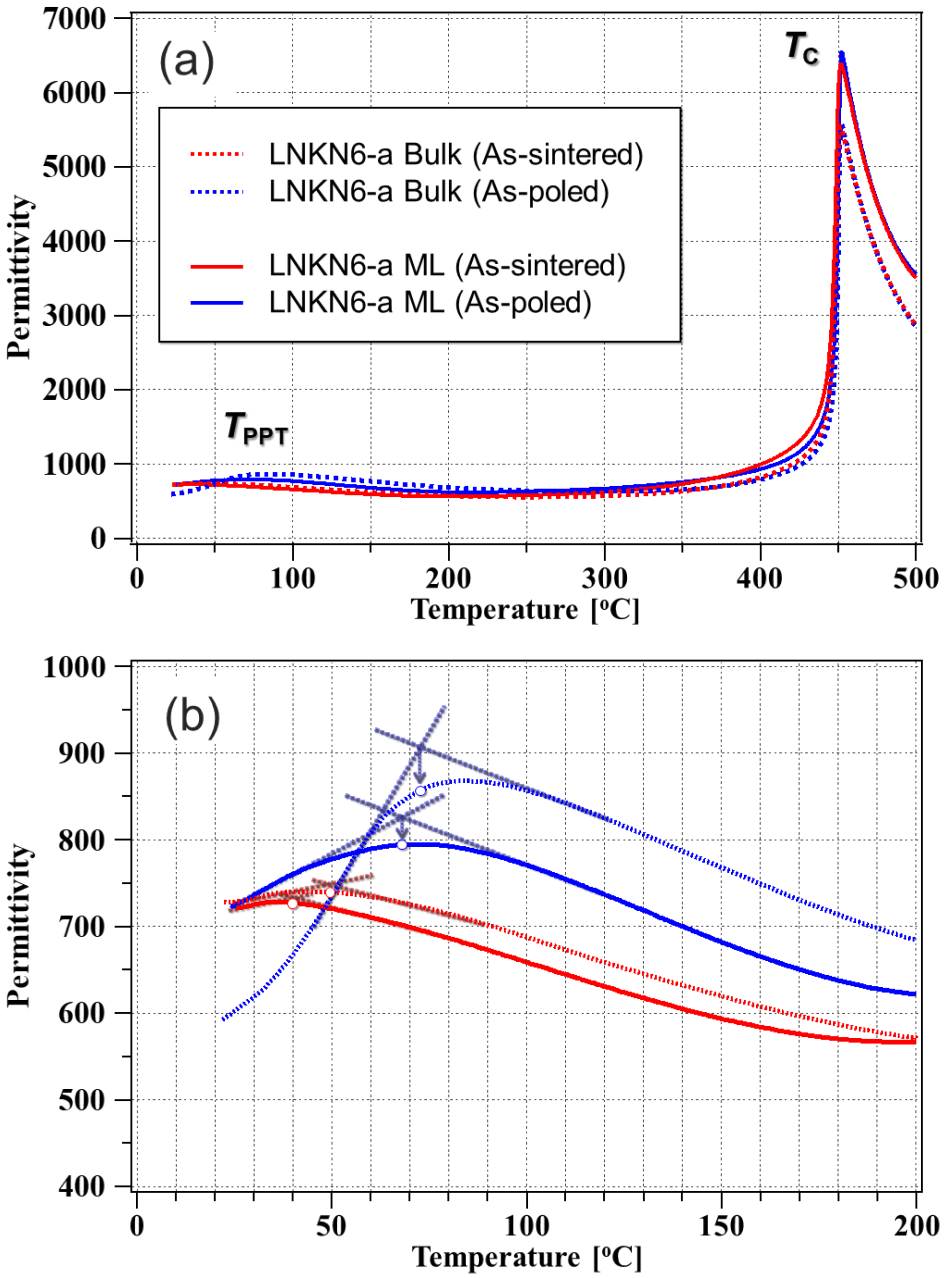

Figure 5.3: (a) Temperature-dependent permittivity of as-sintered (red) and as-poled (blue) LNKN6-a ceramics. Bulk and ML LNKN6-a are shown. (b) Polymorphic phase transition temperature (T_{PPT}) of the as-sintered and as-poled LNKN6-a piezoceramics calculated from the crossing point of the tangent lines in the vicinity of the dielectric anomaly. (Reprinted with permission from [97]. Copyright 2020 © AIP Publishing.)

Stress–strain and stress−polarization hysteresis loops of the as-poled LNKN6-a ML are shown in Fig. 5.4(a). The sequence symbols from (I) to (IV) represent different domain states. The electrically poled sample started with an out-of-plane oriented domain structure (I). During compressive stress loading, the strain initially increased linearly. Further application of compressive stress changed the strain response to that of nonlinear behavior due to ferroelastic domain switching. This nonlinearity further increases with increasing compression until all available ferroelastic domains have been switched. The inflection point during the loading process (II) was defined as the coercive stress σ_C. At the saturated point (III), no additional domains were reoriented, and the material response in the vicinity of the point became linearly elastic again. Upon unloading, the material that was initially linearly elastic toward the ideal strain S_i began to exhibit nonlinearity with decreasing compressive stress. This was due to the local electrical and mechanical fields in the polycrystalline material, resulting in the switching of certain domains back to the initial state (I). Nevertheless, the sample did not reach its initial state (IV≠I) because not all domains switch back, resulting in a remanent strain S_r. The inset in Fig. 5.4(a) shows a schematic of the domain structures at the states mentioned above [87]. The coercive stress during the loading process was −91.8 MPa [Fig. 5.4(b)].

Additionally, the intersection between the tangent line at σ_C and the linear extrapolations from the zero point (σ_a) and from the maximum field (σ_b) were located at −52.6 MPa and −153.1 MPa, respectively. From the stress−polarization hysteresis loop, indicated by the dotted gray line shown in Fig. 5.4(c), the inflection point of polarization change in (π_C) was −118.8 MPa. The

appearance of a polarization change suggests a transition to the in-plane oriented domain structure from the out-of-plane oriented domain structure. Additionally, the intersections between the tangent lines at π_C and the linear extrapolations form the zero point (π_a) and from the maximum field (π_b) were −67.1 MPa and −202.3 MPa, respectively. The start-point of the nonlinear polarization change, π_a, was larger than −40 MPa. Therefore, we suspected that the as-poled LNKN6-a ML maintained its poling state up to −40 MPa. Notably, σ_C of the LNKN6-a bulk piezoceramic was approximately −160 MPa at the as-sintered state [68], which is higher than the σ_C of the as-poled LNKN6-a ML. This difference is considered to originate from a local-scale stress variation around the inner LNKN6-a ML electrode [98]–[100].

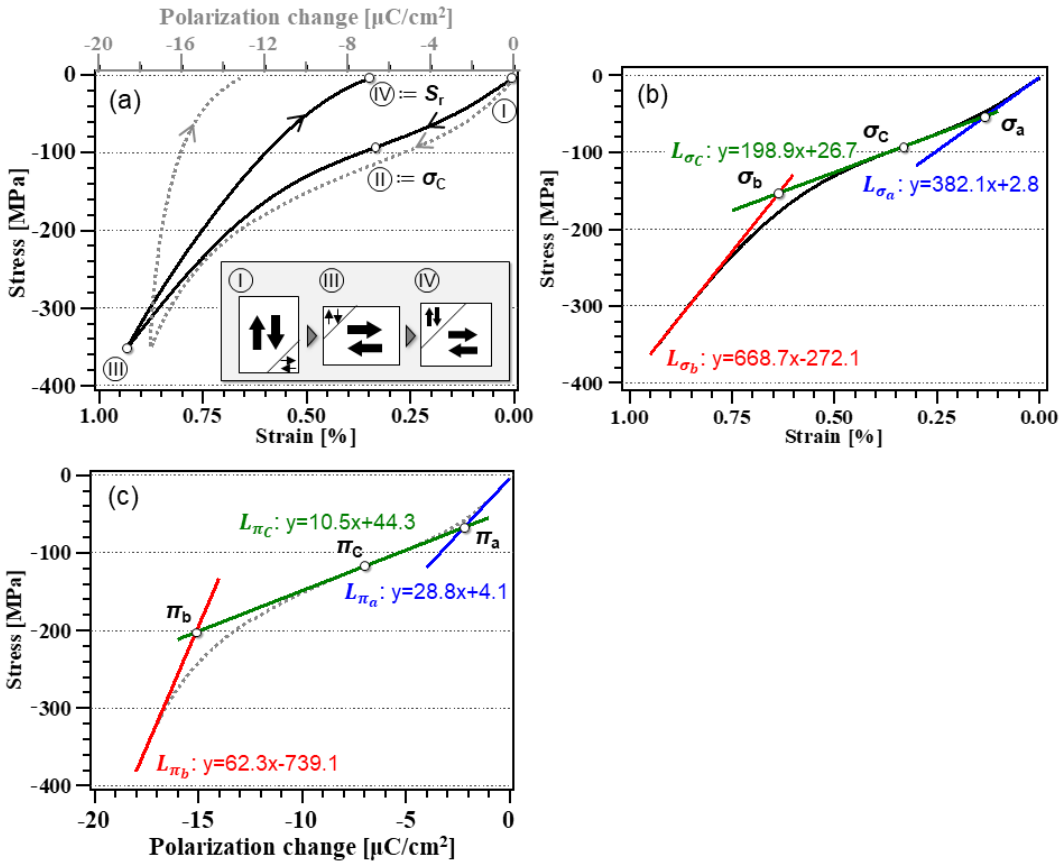

Figure 5.4: (a) Compressive stress dependence of longitudinal strain and the polarization change in a LNKN6-a ML. The stress−strain and stress−polarization hysteresis loops are indicated by the solid black and gray dotted lines, respectively. (b) Loading process of the stress−strain curve denoted by a solid black line. The intersections between the tangent line at the inflection point (σ_C) and the linear extrapolations from the zero point (σ_a) and from the maximum field (σ_b), are illustrated. The tangent lines at σ_C were labeled L_{σ_C}, and linear extrapolations from the zero point of the stress−strain hysteresis loop and the maximum field were labeled L_{σ_a} and L_{σ_b}, respectively. (c) Loading process of the stress−polarization change denoted by the dotted gray curve. The intersections between the tangent line at the inflection point (π_C) and the linear extrapolations from the zero point (π_a) and from the

maximum field (π_b) are illustrated. The tangent lines at π_C were labeled L_{π_C}, and linear extrapolations from the zero point of the stress−polarization hysteresis loop and the maximum field were labeled L_{π_a} and L_{π_b}, respectively. (Reprinted with permission from [97]. Copyright 2020 © AIP Publishing.)

The electric-field-induced strain response, up to an applied electric field of 14 kV/mm and without externally applied stress, is shown in Fig. 5.5(a). This sequential change in the *S*−*E* hysteresis loops reflects a susceptibility of the non-180° domain to the applied electric fields. The electromechanical strain increased, with an *S*-like shape, when the applied field increased from 2 kV/mm to 8 kV/mm. This *S*-shape of the *S*–*E* curve saturated at applied fields over 10 kV/mm, which is represented in the plot by a downward bending shape. This change suggested a decreasing amount of non-180° domains contributing to the electromechanical strain upon increasing the applied electric field [101]. To demonstrate this change in detail, the inflection point of the *S*−*E* curve (X_C) and intersections between the tangent line at X_C, as well as the linear extrapolations from the zero point (X_a) and from the maximum field (X_b) were characterized (Fig. 5.5(b)). Fig. 5.5(c) depicts the electric field dependence of the d_{33}^* (S_{max}/E_{max}), where a maximum of 341 pm/V at 6 kV/mm was observed. This is equated to the latter half of the *S*−shape region ($X_C - X_b$), the hatched gray region in Fig. 5.5(c), and suggests that most of the electromechanical strain, caused by non-180° domains, already occurred by 6 kV/mm. Thus, further measurements were conducted at a maximum electric field of 6 kV/mm.

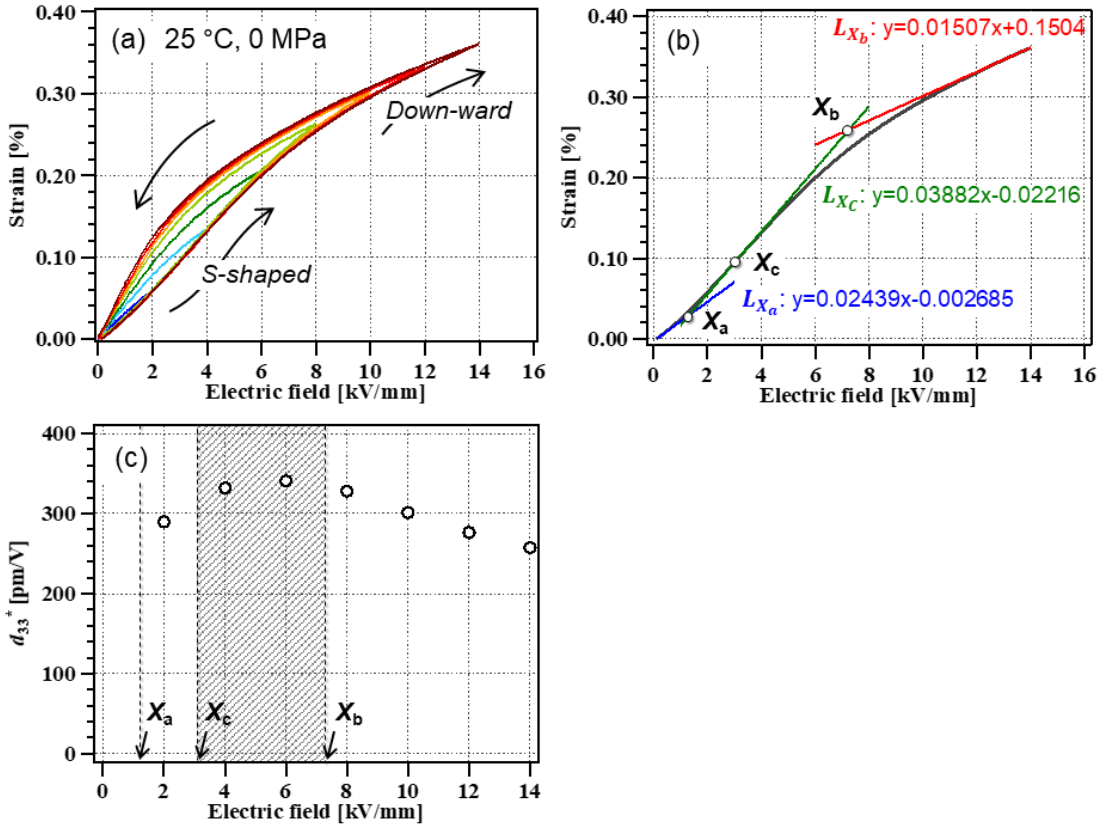

Figure 5.5: (a) Electromechanical response as a function of maximum applied electric field. (b) Loading process of the *S*−*E* curve (black curve). The intersections between the tangent line at the inflection point (X_C) and the linear extrapolations from the zero point (X_a) and from the maximum field (X_b) are shown. The tangent lines at X_C were labeled L_{X_C}, and linear extrapolations from the zero point of the stress−strain hysteresis loop and the maximum field were labeled L_{X_a} and L_{X_b}, respectively. (c) Electric-field dependence of piezoelectric constant d_{33}^*. (Reprinted with permission from [97]. Copyright 2020 © AIP Publishing.)

Changes in the previously mentioned *S*–*E* curve shape and the macroscopic properties were observed after applying a uniaxial compressive stress to the MLs during electric-field loading (Figure 5.6). S_{Max}, measured at 6

kV/mm, decreased from 0.21% at −5 MPa to 0.13% at −40 MPa, when the compressive stress was increased at 25 °C. Simultaneously, the shape of the *S*–*E* curve changed from an S-shape and an increase in linearity was observed. Interestingly, upon further increasing the compressive stress, a subsequent increase in S_{Max} was observed at −80 MPa and the curve exhibited an *S*-shape again. Above a specific level of compressive stress, the *S*–*E* curves began to show an upward bending and a further reduction of field-induced strain occurred. These behaviors were also observed in the measurements at 50 °C and 75 °C. On the other hand, the electric-field-induced strain at 100 °C was continuously suppressed with increasing compressive stress.

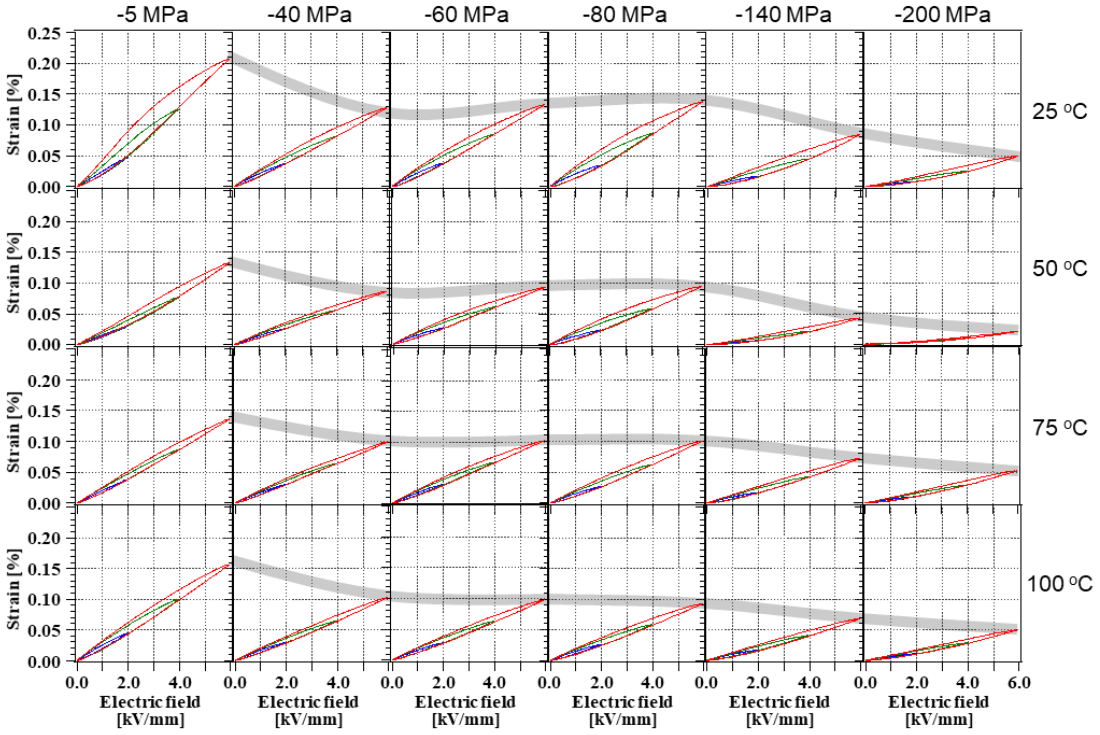

Figure 5.6: Compressive stress dependence of *S*−*E* loops measured at 25 °C, 50 °C, 75 °C, and 100 °C. (Reprinted with permission from [97]. Copyright 2020 © AIP Publishing.)

To compare the results with the literature, the maximum unipolar strain was normalized with the maximum electric field, *i.e.*, the large-signal piezoelectric constant d_{33}^*. The compressive stress dependence of $d_{33}^*(\sigma)$ in LNKN6-a ML, measured at several temperatures and electric-field values, is summarized in Fig. 5.7. Except for 100 °C, $d_{33}^*(\sigma)$ of the as-poled LNKN6-a ML with unipolar actuation exhibited a local maximum at a certain stress level, σ_{Peak}. This enhancement in d_{33}^* under unipolar actuation by uniaxial compressive stress has been observed in other piezoceramics. Stress-dependent *P*−*E* and *S*−*E* hysteresis loops of soft-type PZT under unipolar drive showed an enhancement at a certain stress level [16]. This enhancement may be due to the fact that the

highest achievable strain originates from in-plane oriented domains switched to out-of-plane via an electric field. Owing to the mechanical compressive stress, domains can be aligned in the in-plane orientation. As a result, the overall strain was enhanced compared to samples with randomly distributed domains. Nevertheless, this enhancement is only possible if the applied electric field is large enough to counteract the applied mechanical stress. Therefore, the local maximum σ_{Peak} of the as-poled LNKN6-a ML was also regarded as the balance of the non-180° domain orientation by electric field and compressive stress. Local maxima of the $d_{33}^{*}(\sigma)$ σ_{Peak}s had electric-field dependence at 25 °C and 50 °C. Electric-field-induced strain was primarily due to the extrinsic effect of the piezoactive layers. Therefore, the higher electric field could generate a larger force to push back the uniaxial stress. Additionally, σ_{Peak}s of 6 kV/mm were located at −80 MPa at 25 °C and 50 °C, while the maximum was shifted to −60 MPa at 75 °C. Furthermore, no local maximum peak was observed at 100 °C. The ferroelastic behaviors of the LNKN6-a ML require further investigation to explain these suppressions under combined loadings.

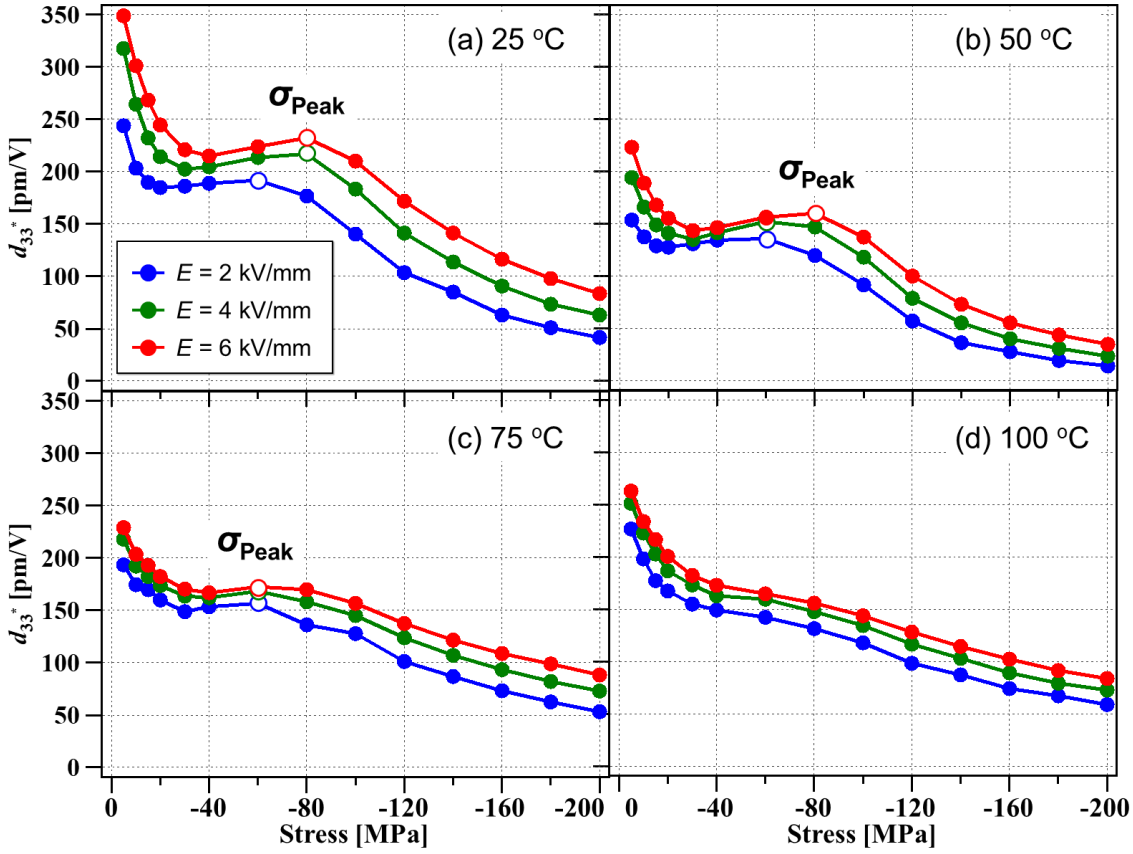

Figure 5.7: Compressive stress dependence of piezoelectric constant $d_{33}^{*}(\sigma)$ induced by unipolar electric fields in the LNKN6-a ML at (a) 25 °C, (b) 50 °C, (c) 75 °C, and (d) 100 °C. The local maximum points, σ_{peak}, are denoted by open circles. (Reprinted with permission from [97]. Copyright 2020 © AIP Publishing.)

Figure 5.8 shows the comparison of $d_{33}^{*}(\sigma)$ measured at 25 °C and 100 °C. The major trend of $d_{33}^{*}(\sigma)$ at 25 °C, which occurred over −200 MPa, exhibited a gradual decrease with a local maximum at −80 MPa. According to the literature, soft-type bulk PZT demonstrated this peak at −50 MPa, which had a similar value to that of coercive stress [73]. The coercive stress of the as-poled LNKN6-a ML was −91.8 MPa, which is close to the peak value of $d_{33}^{*}(\sigma)$ (−80 MPa). Therefore,

this peak is considered as a balance of the non-180° domain orientation produced by the applied electric field and the compressive stress (Fig. 5.8, region (ii)). The *S*-shaped configuration of *S*−*E* loops appearing at −80 MPa also supports this explanation (Fig. 5.6). Above −80 MPa, the in-plane orientation of the domain structure became predominant upon increasing the compressive stress for the LNKN6-a ML. Stress levels above the local peak σ_{peak} lead to domain clamping, suppressing the out-of-plane domain orientation via an applied electric field (Fig. 5.8). As a result, the shape of the *S*−*E* curves resulted in upward bending since a higher field would be required to switch domains against the applied mechanical stress. Above that threshold stress σ_{peak}, domain clamping was predominant (Fig. 5.8, region (iii)). In contrast, the compressive stress dependence of $d_{33}^{*}(\sigma)$ at 100 °C showed a gradual decrease, owing to thermal depolarization during the phase transition from monoclinic to tetragonal (Fig. 5.6). Notably, the stress-induced phase transformation of the monoclinic phase and the electric-field-induced phase transformation of the tetragonal phase are evident around the PPT, as suggested by previous studies [47],[48]. These opposing processes potentially influence the macroscopic electromechanical performance of the LNKN6-a ML with increasing stress. However, to evaluate the extent of this influence, *in situ* XRD would be required. Nevertheless, stress-induced phase transformation seemed to have a significant impact in the first region (Fig. 5.8, region (i)).

The electrically poled domain structure of LNKN6-a ML seemed to remain at −40 MPa at 25 °C, but the actuation was significantly constrained by compressive stress [Fig. 5.8, region (i)]. There are two possible reasons for this. First, the effect of domain clamping became more pronounced in the PPT region with

applied compressive stress. Martin et al. reported the temperature dependence of the piezoelectric small signal d_{33} (T) of Li-modified $(Na_{0.5}K_{0.5})NbO_3$ piezoceramics [102]. According to their investigation, $d_{33}(T)$ exhibited a sharp peak in the vicinity of T_{PPT} under zero stress, as reported in PZT [103],[104]. Additionally, when the Li substitution increased from 0 mol% to 4 mol%, the T_{PPT} shifted from 210 °C to 111 °C. The sharp peak of $d_{33}(T)$ in Li-modified NKN disappeared under −50 MPa, which was sufficiently lower than its coercive stress σ_C. Notably, the d_{33} of 4 mol% Li-modified NKN at 25 °C decreased from 118 pC/N (at –5 MPa) to 107 pC/N (at −50 MPa), respectively, owing to the disappearance of the electromechanical enhancement in the vicinity of the T_{PPT}. The T_{PPT} was 111 °C in 4 mol% Li-modified NKN piezoceramics. The T_{PPT} of as-poled LNKN6-a ML was 70 °C; therefore, the disappearance of the electromechanical enhancement in $d_{33}(T)$ significantly affected the large-signal piezoelectric constant $d_{33}^*(\sigma)$ in the temperature range from 25 °C to 100 °C. Second, the material was in the PPT region under the zero-stress condition. This region shifts to a higher temperature and can lead to a drastic deterioration of d_{33}^* when a compressive stress is applied. We recently reported that LNKN6-a samples exhibited a shift in T_{PPT} by ~0.2 °C/MPa [48]. This was significantly larger than that observed for other perovskite ferroelectrics, such as polycrystalline $BaTiO_3$ [105] and PZT [104], which exhibited display rates of 0.05 °C/MPa and 0.1 °C/MPa, respectively.

This unique sensitivity to the applied stress seemingly originates from the PPT region and appears to be influenced by the composition. For example, Wang et al. reported the electromechanical properties of

$0.95(K_{0.49}Na_{0.49}Li_{0.02})(Ta_{0.2}Nb_{0.8})O_3$-$0.05CaZrO_3$ + 2 wt% MnO_2 (hereinafter CZ5) piezoceramics under uniaxial strain [106]. CZ5 exhibited temperature-insensitive properties from room temperature to 175 °C [107]. Thus, CZ5 exhibited enhanced electromechanical properties without a drastic decrease, as seen in region (i) in Fig. 5.8. This behavior was also observed for the respective PPT region. However, as shown by Martin et al., LNKN6-a exhibited the most significant change in macroscopic ferroelastic properties around the PPT [68]. In future studies, it would be interesting to determine the underlying microscopic process that leads to these stress-sensitive properties. Understanding this process could lead to more durable material design for harsh environments. Piezoelectric materials should possess excellent piezoelectric properties and increased stability to the fluctuation of temperature and stress. Consequently, the material should be designed in the off-PPT region, rather than pursuing high piezoelectric constants at room temperature and under zero-stress conditions by fixing the material composition in the PPT region.

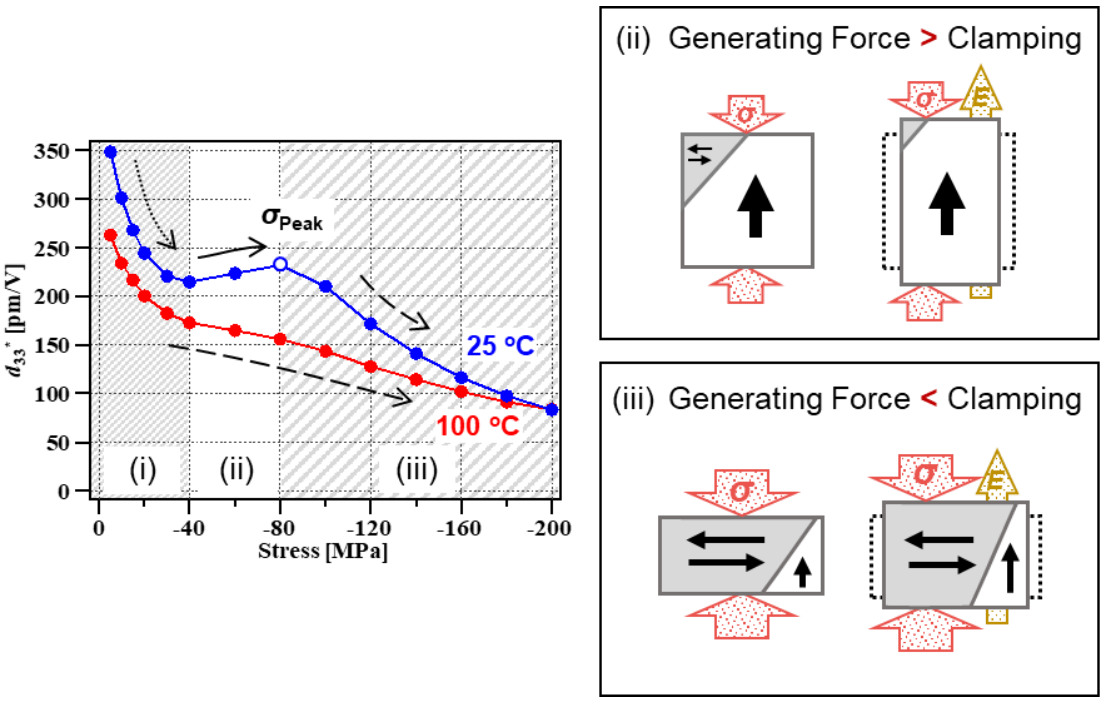

Figure 5.8: Temperature dependence of $d_{33}^*(\sigma)$ and schematic images of domain transformation with mechanical (σ) and electrical (E) loadings in regions (ii) and (iii). (Reprinted with permission from [97]. Copyright 2020 © AIP Publishing.)

5.3 Conclusion

The large-signal unipolar behavior of LNKN6-a ML was characterized under combined electrical and mechanical loadings. The major trend of $d_{33}^*(\sigma)$ at 25 °C, which takes place over −200 MPa, was a gradual decrease with a local maximum in $d_{33}^*(\sigma)$ defined as σ_{peak}. This stress level was consistent with the coercive stress, σ_C, of the as-poled LNKN6-a ML. Therefore, σ_{peak}s below 100 °C was considered in terms of the non-180° domain orientation produced by the balance of the combined electrical and stress fields. On the other hand, $d_{33}^*(\sigma)$ at 100 °C revealed a gradual decrease without an apparent peak, but a hump was observed

at −80 MPa. The disappearance of the peak was mainly due to a thermal depolarization induced during the structural phase transition from orthorhombic to tetragonal. Additionally, the drastic deterioration of d_{33}^{*} up to −40 MPa was attributed to the fact that the material was in the PPT region; therefore, its domain structure was easily clamped by the uniaxial stress. Furthermore, a shift of T_{PPT} also affected the deterioration observed in the wide temperature range (25–100 °C).

In actuator applications, ML piezoceramics are often intended for use under mechanical preload to reduce undesirable tensile stresses. Piezoelectric materials should exhibit excellent piezoelectric properties and stability with temperature fluctuation and stress. In that context, preloading on LNKN6-a ML up to −40 MPa was considered a moderate condition that achieved a high piezoelectric d_{33}^{*} constant (~200 pm/V) over the wide temperature range (25-100 °C). Our results suggest that the material should be designed in the off-PPT region, rather than pursuing high piezoelectric constants at room temperature and under zero-stress conditions by fixing the material composition in the PPT region.

6. Unipolar fatigue of multilayered piezoceramics and impedance spectroscopy

In this chapter, the unipolar fatigue of LNKN6-a ML is characterized using *P*–*E* hysteresis measurement. Furthermore, the domain effect during the fatigue process is determined by impedance spectroscopy. Piezoelectric actuators are most commonly operated in unipolar driving mode. Strain and polarization degradation during long-term use in the unipolar driving mode is mainly attributed to the domain effect [36],[108]. However, since several factors such as the domain effect and mechanical failure simultaneously affect cyclic fatigue, the specific cause is difficult to identify. Impedance spectroscopy is a powerful tool that can be used to investigate the causes of fatigue. Impedance spectroscopy is used to characterize the electrical properties of microstructures, such as grains, GBs, and EI–Ceram interfaces. Impedance values are averages obtained after the measurement of numerous grains and GBs, so modeling is required to analyze the averaged data. The brick layer model has been used to interpret the impedance spectra of polycrystalline materials [109]. Core–shells with heterogeneous microstructures containing pure $BaTiO_3$ cores (ferroelectric) and $BaTiO_3$ shells with additives (paraelectric) [36],[109] and the oriented domain structure of $LiTaO_3$ single crystals [110] have also been evaluated. It has been reported that the electrical properties of grains and GBs in $(Na,K)NbO_3$ piezoceramics can be evaluated near the T_C, and that domain orientation in a strong electric field is accompanied by spectral changes [111].

The objective of this study is to evaluate the domain structure of ML piezoceramics in a fatigued state using the frequency distribution of their impedance spectra. In this study, we analyzed the impedance spectra of Li-modified (Na,K)NbO_3 ML piezoceramics near T_C to compare the ferroelectric and paraelectric phases. We also investigated the mechanism of unipolar fatigue by performing unipolar *P–E* hysteresis measurements and impedance spectroscopy.

6.1 Experimental procedure

We synthesized an ML $Li_{0.06}Na_{0.52}K_{0.42}NbO_3$ piezoceramic containing 0.65 mol% Li_2CO_3, 1.3 mol% SiO_2, 0.2 mol% $MnCO_3$, and 0.5 mol% $SrZrO_3$ (LNKN6-a ML) using a previously reported tape-casting method [67]. A cross-sectional view of LNKN6-a ML is shown in Fig. 6.1. The ML structure consisted of 10 ceramic layers and 11 Pd inner electrode layers. The dimensions of the ML samples were 3.2 mm × 0.7 mm × 1.6 mm (length × height × width), and the ceramic layer thickness was 50 μm. Silver paste was fired onto the terminal to serve as an external electrode. Figure 6.2 shows the ML structure taken from the mirror-polished surface of the LNKN6-a ML. The side margins and cover layers of the ML were 242 μm and 75 μm, respectively. LNKN6-a ML was poled by placing it in silicon oil at 100 °C and subjecting it to a 4 kV/mm DC electric field for 3 min. Samples were cooled to 40 °C with DC loading to prevent the effect of thermal disturbance on the as-poled state. A cyclic unipolar field was then applied to the poled LNKN6-a ML sample in silicone oil at 100 °C. Cycling performance was investigated by subjecting it to 4 kV/mm unipolar triangular waves at 50 Hz for up to 10^7 cycles.

Immediately after the cyclic field application, the samples were cooled down to 40 °C with a 4 kV/mm DC electric field to maintain the fatigued state. *P*−*E* curves and impedance spectra were recorded 24 h after poling treatment and after the fatigue test to account for aging effects [83],[112]. Impedance measurements were conducted at 10 °C intervals in the temperature range from 400 °C to 500 °C with a downward sweep in a 0.5 V/mm oscillating field using a frequency response analyzer (NF FRA5097) connected to a current amplifier (NF CA5350). Piezoceramics have resonance frequencies, and the permittivity of these materials jumps near these frequencies [113]. The first resonance frequency of as-poled LNKN6-a ML was 665 kHz, so we selected a frequency range below this value. Sweep measurements were performed near the Curie temperature, T_C. Parallel circuits with resistors and constant phase elements (R−CPEs) were selected for equivalent circuit fitting. The impedance (Z_{CPE}), capacitance (C), and relaxation frequency (ω_{Max}) of each R−CPE circuit were calculated using Equations 6.1–6.3.

$$Z_{\mathrm{CPE}} = \frac{R}{1 + (j\omega)^{p} T_{\mathrm{CPE}} R}, \tag{6.1}$$

$$C = T_{\mathrm{CPE}}^{1/p} \cdot R^{(1-p)/p}, \text{ and} \tag{6.2}$$

$$\omega_{\mathrm{Max}} = \frac{1}{2\pi (T_{\mathrm{CPE}} R)^{\frac{1}{p}}}, \tag{6.3}$$

where ω is the frequency, T_{CPE} is the CPE constant, and p is the CPE index.

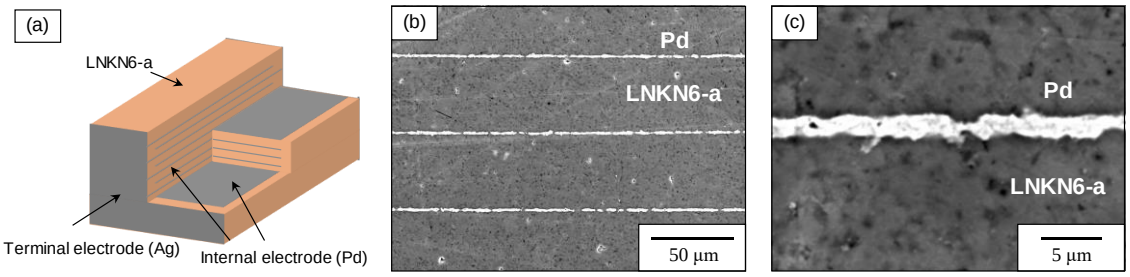

Figure 6.1: (a) Cross-sectional view of LNKN6-a ML. (b) External and (c) cross-sectional views of the polished surface of the ML sample. (Reprinted with permission from [72]. Copyright 2020 © The Japan Society of Applied Physics.)

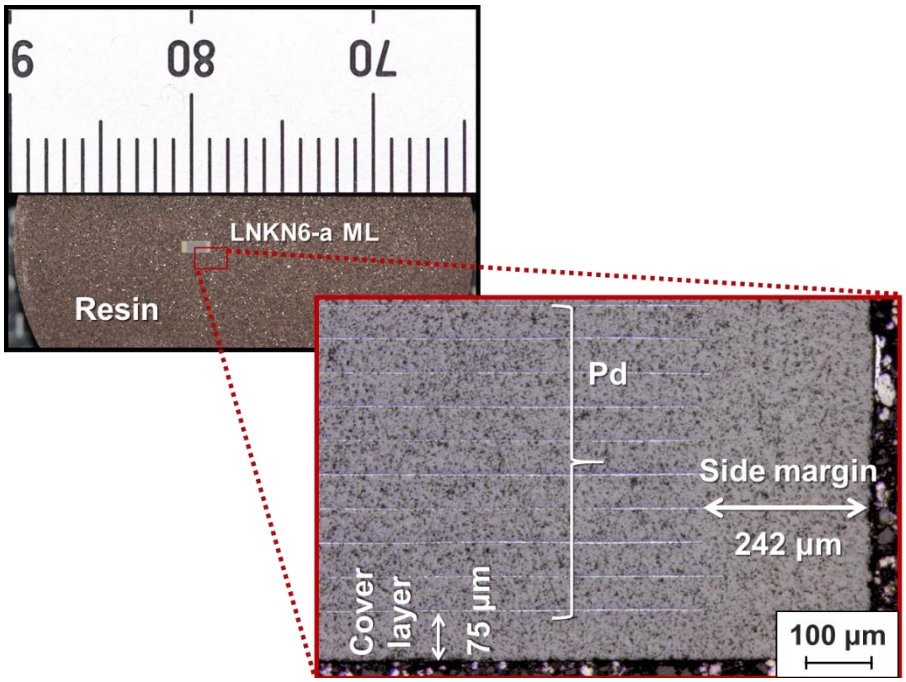

Figure 6.2: Mirror-polished surface of the LNKN6-a ML. The side margins and the cover layers are 242 μm and 75 μm, respectively.

6.2 Results and discussion

6.2.1 Cyclic properties

The unipolar *P*−*E* hysteresis loops recorded before and after loading the cyclic field are shown in Fig. 6.3. Changes in the polarization induced by three continuous unipolar waves are plotted in Fig. 6.3(a). The second set of *P*−*E* loops shown in Fig. 6.3(b) were extracted from the continuous wave data to determine the trajectory of switchable polarization. The amount of polarization in the unipolar electric field decreased from 12.4 μC/cm^2 in the as-poled state to 11.3 μC/cm^2 in the fatigued state, which was given by $P_{Max} - P_0$. The second set of *P*−*E* loops were closed for both the as-poled and fatigued samples, so leakage current did not appear to increase in the applied cyclic field. Cyclic fatigue during bipolar actuation is reportedly primarily due to mechanical failure at the interfaces between ceramics and electrodes and at GBs [23], whereas cyclic fatigue during unipolar actuation is attributed to DW pinning [25]. DW pinning was presumably responsible for the decrease in polarization shown in Fig. 6.3(b). The unipolar driving mode was used for actuator applications. Unipolar fatigue has been reported to occur both in ceramics containing lead, such as Pb(Zr,Ti)O_3, and lead-free ceramics, such as (1−x)$Bi_{1/2}Na_{1/2}TiO_3$-x$BaTiO_3$ [114], (Na,K)NbO_3 [27], and (Ba,Ca)(Ti,Zr)O_3 [36].

The main aim of this study was to distinguish between the effect of domain orientation and other effects. Evaluating *P*−*E* hysteresis by performing positive-up-negative-down (PUND) polarization measurements enabled us to ignore contributions from the leakage current and focus on the effect of domain switching [115],[116]. Dittmer et al. reported that when the leakage current is small, changes

in the polarization of a sample and energy loss due to the domain orientation can be calculated by extracting a closed loop from a continuous unipolar wave [71]. This technique can be applied to characterize unipolar fatigue without having to consider the pre-poling behavior and leakage current. The energy loss (e_{loss}) depicted in the inset of Fig. 6.3(b) was quantified using Equation (4).

$$e_{loss} = \oint P(E) \cdot dE \tag{4}$$

The dissipation energy, e_{loss}, decreased from 178.6 kJ/m^3 to 164.0 kJ/m^3, which confirms that DW pinning occurred during the cycling test.

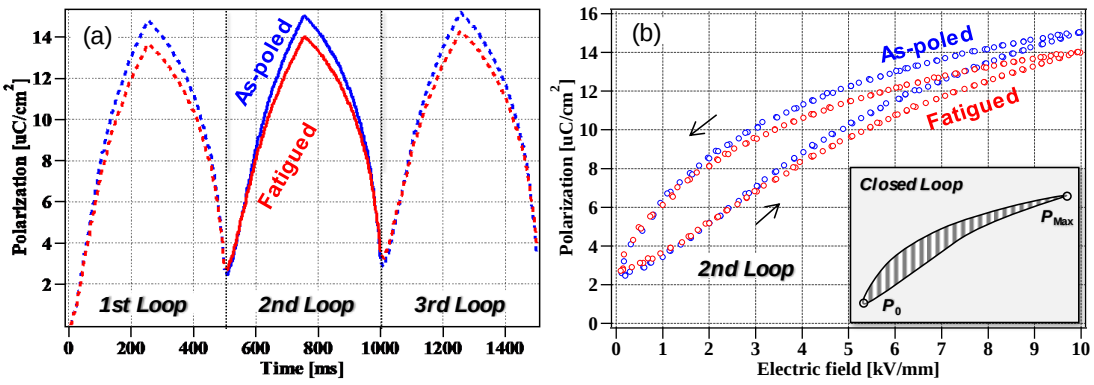

Figure 6.3: Unipolar *P*–*E* hysteresis loops of LNKN6-a ML. (a) Changes in polarization during three continuous loops. (b) Second set of hysteresis loops extracted from the continuous waves. Closed loops are obtained for both the as-poled and fatigued samples. The dissipation of energy (e_{loss}) is illustrated schematically in the inset. (Reprinted with permission from [72]. Copyright 2020 © The Japan Society of Applied Physics.)

6.2.2 Impedance analysis

The impedance spectra of the as-sintered, as-poled, and fatigued LNKN6-a ML samples in Fig. 6.4 were acquired near the T_C of 450 °C to compare the ferroelectric and paraelectric phases. The impedance spectra in Fig. 6.4(a–c) show the dependence of cyclic fatigue below the T_C. Two relaxation processes in the frequency range from 500 kHz to 10 mHz indicated in the spectra of LNKN6-a ML also occur in single-layer (SL) (Na,K)NbO_3-based ceramics [117],[118]. The spectra of the as-sintered and as-poled samples in Fig. 6.4(c) indicated that impedance decreased isotopically by 47%, and that it decreased again by 18% after the cyclic field was applied. This behavior was attributed to the domain orientation. The impedance spectra in Fig. 6.4(e) were acquired above the T_C, and they also reflected two relaxation processes in the measured frequency range. The semicircular plot of Factor 1 did not change after the cyclic field was applied, whereas that of Factor 2 broadened after the field was applied (Fig. 6.4(f)). Considering the disappearance of the ferroelectric domain structure, the difference of Factor 2 was not due to the domain wall pinning.

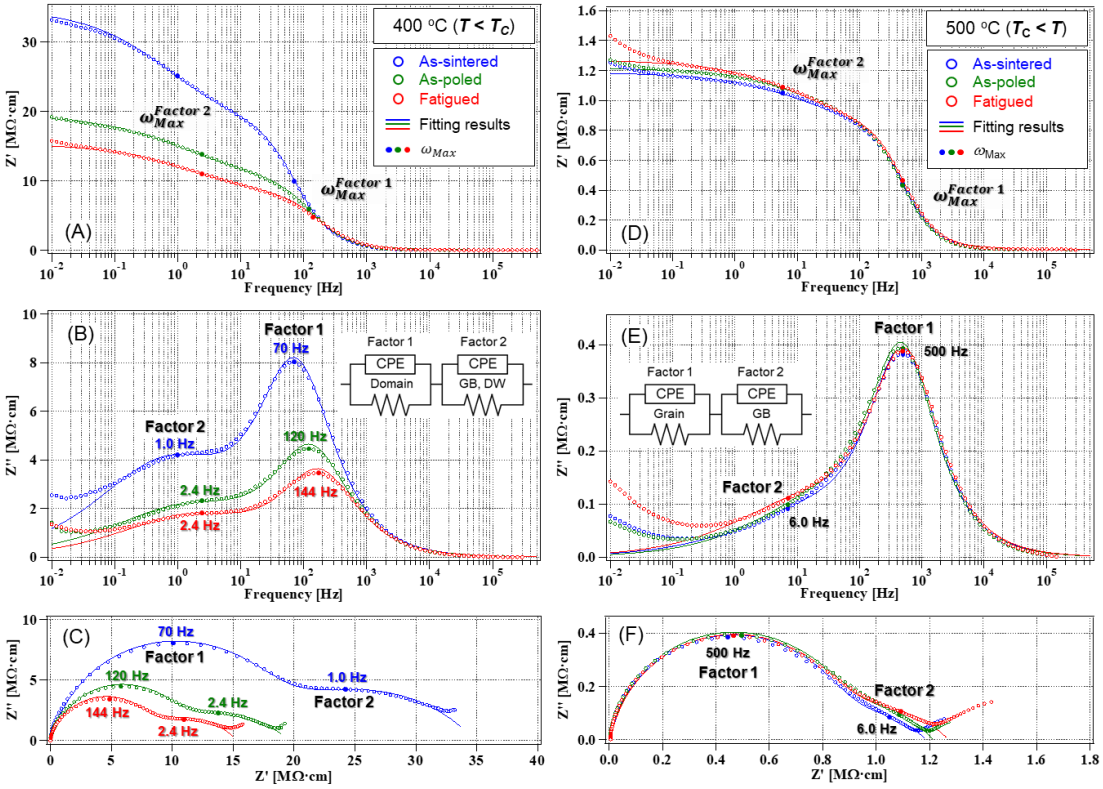

Figure 6.4: Impedance spectra of the as-sintered, as-poled, and fatigued LNKN6-a ML samples at (a–c) 400 °C ($T < T_C$) and (d–f) 500°C ($T > T_C$). Fitting results obtained with a 2 R−CPE equivalent circuit were appended to the measured spectra. The relaxation frequencies (ω_{Max}) are indicated by the filled circles. (Reprinted with permission from [72]. Copyright 2020 © The Japan Society of Applied Physics.)

The results obtained by fitting the spectra in Fig. 6.4 are shown in Fig. 6.5. The fitting parameters obtained from the 2 R−CPE equivalent circuit analysis are summarized in Table 6.1, and a schematic illustration of the relaxation process of LNKN6-a ML below T_C is shown in Fig. 6.6. Changes in the permittivity and conductivity (log σ) with temperature are shown for Factor 1 in Fig. 6.5(a) and

6.5(b). The permittivity of Factor 1 exhibited a dielectric anomaly, which indicated that Factor 1 was associated with inner domains [119],[120]. Therefore, Factor 2 was attributed to boundaries, including GBs and DWs. The decline in the permittivity values of Factor 1 from as-sintered to fatigued samples below T_C was attributed to the domain orientation toward the applied field [121]. The amplitude during the poling and fatigue tests was approximately three times that of the coercive field (E_C) of LNKN6-a [83]. The decrease in impedance as the as-poled sample was fatigued [Fig. 6.4(c)] may have been due to an increase in the volume fraction of domains that oriented toward the applied field, which was facilitated by DW pinning. Arrhenius plots showing conductivity for Factor 1 are shown in Fig. 6.5(b). The thermal activation energies (E_as) of the as-sintered, as-poled, and fatigued samples were 1.24 eV, 1.03 eV, and 0.98 eV, respectively. The measured conductivities and activation energies were nearly equal to those reported for $(Na_{0.5}K_{0.5})NbO_3$ piezoceramics [117], so we concluded that doubly ionized oxygen vacancies were the primary conductive carriers in this temperature range [117],[118],[122],[123].

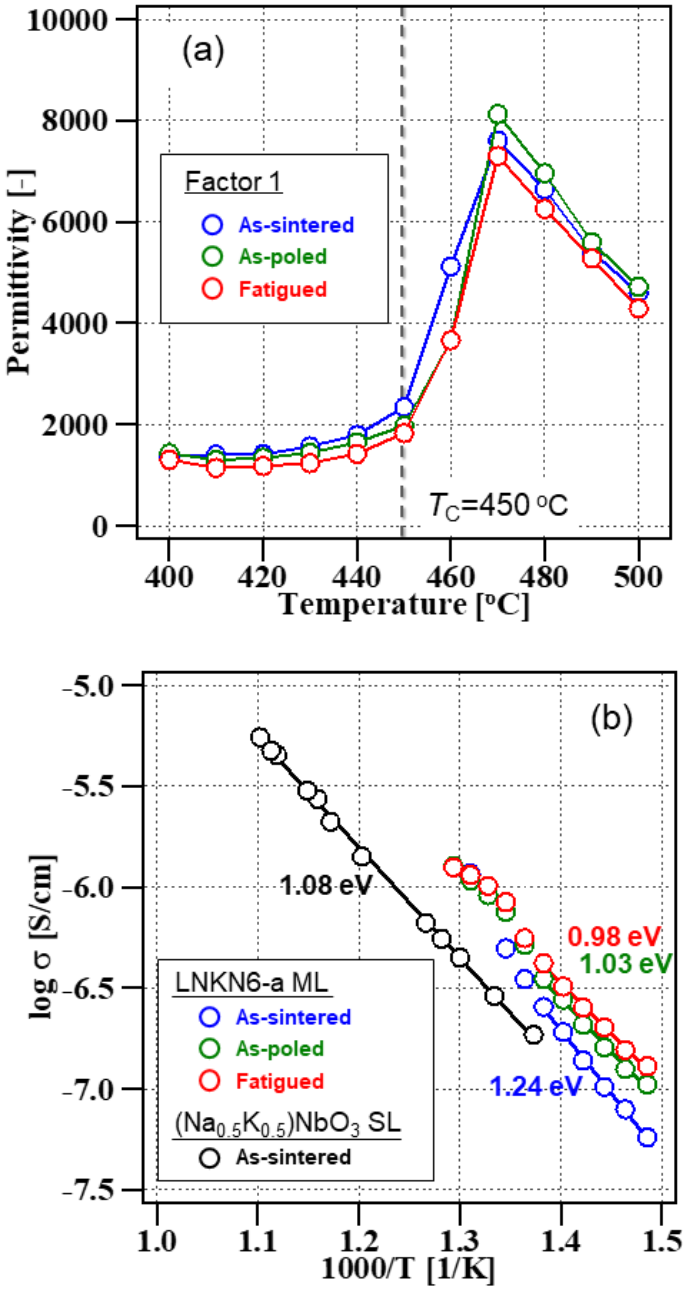

Figure 6.5: (a) Temperature dependence of permittivity in Factor 1 calculated by 2 R−CPE equivalent circuit fitting. (b) Changes in conductivity in Factor 1 at several stages of fatigue. The conductivity of a $Na_{0.5}K_{0.5}NbO_3$ SL ceramic is appended to the graph [117]. (Reprinted with permission from [72]. Copyright 2020 © The Japan Society of Applied Physics.)

Table 6.1: Parameters of the 2 R−CPE equivalent circuit used to fit the as-sintered, as-poled, and fatigued LNKN6-a ML sample data. (Reprinted with permission from [72]. Copyright 2020 © The Japan Society of Applied Physics.)

	As-sintered						As-poled						Fatigued					
	Factor 1			Factor 2			Factor 1			Factor 2			Factor 1			Factor 2		
Temperature [°C]	*R [kΩ]*	*T_{CPE}*	*p*	*R [kΩ]*	*T_{CPE}*	*p*	*R [kΩ]*	*T_{CPE}*	*p*	*R [kΩ]*	*T_{CPE}*	*p*	*R [kΩ]*	*T_{CPE}*	*p*	*R [kΩ]*	*T_{CPE}*	*p*
400	332.57	12.87×10^{-9}	0.885	332.96	1.37×10^{-6}	0.537	181.33	13.86×10^{-9}	0.890	192.17	1.74×10^{-6}	0.498	147.22	13.48×10^{-9}	0.886	145.81	2.03×10^{-6}	0.527
410	241.33	13.44×10^{-9}	0.888	240.80	1.71×10^{-6}	0.523	152.32	12.37×10^{-9}	0.897	137.66	1.98×10^{-6}	0.523	122.00	10.29×10^{-9}	0.910	103.28	2.36×10^{-6}	0.556
420	186.88	13.60×10^{-9}	0.891	162.41	2.04×10^{-6}	0.558	118.99	12.11×10^{-9}	0.907	104.18	2.45×10^{-6}	0.515	94.62	9.93×10^{-9}	0.921	79.83	3.01×10^{-6}	0.532
430	138.39	15.37×10^{-9}	0.891	124.46	2.37×10^{-6}	0.533	91.65	12.44×10^{-9}	0.916	79.51	2.86×10^{-6}	0.505	75.44	10.47×10^{-9}	0.922	57.54	3.55×10^{-6}	0.552
440	99.92	15.43×10^{-9}	0.913	99.32	2.91×10^{-6}	0.492	68.77	13.48×10^{-9}	0.925	61.83	3.06×10^{-6}	0.493	59.43	12.67×10^{-9}	0.916	43.56	4.07×10^{-6}	0.548
450	74.85	19.90×10^{-9}	0.915	77.88	3.33×10^{-6}	0.477	54.11	15.27×10^{-9}	0.933	48.61	3.40×10^{-6}	0.487	45.50	16.80×10^{-9}	0.913	32.06	5.10×10^{-6}	0.540
460	54.38	42.23×10^{-9}	0.914	41.01	5.42×10^{-6}	0.526	36.96	24.70×10^{-9}	0.949	32.88	3.76×10^{-6}	0.501	34.20	31.99×10^{-9}	0.915	22.19	5.12×10^{-6}	0.570
470	38.36	57.31×10^{-9}	0.927	24.89	7.09×10^{-6}	0.538	25.25	61.78×10^{-9}	0.929	12.51	8.24×10^{-6}	0.557	22.67	54.10×10^{-9}	0.935	13.00	11.87×10^{-6}	0.505
480	18.84	44.51×10^{-9}	0.951	9.66	9.40×10^{-6}	0.522	20.96	52.58×10^{-9}	0.933	11.15	7.84×10^{-6}	0.547	18.80	45.72×10^{-9}	0.940	12.30	9.67×10^{-6}	0.498
490	16.34	39.93×10^{-9}	0.941	8.04	11.29×10^{-6}	0.517	17.70	38.91×10^{-9}	0.948	9.57	8.80×10^{-6}	0.540	16.68	39.76×10^{-9}	0.938	11.01	11.08×10^{-6}	0.486
500	15.03	36.16×10^{-9}	0.935	7.64	13.21×10^{-6}	0.499	15.02	35.11×10^{-9}	0.941	8.15	8.75×10^{-6}	0.543	15.18	36.15×10^{-9}	0.926	9.06	11.42×10^{-6}	0.516

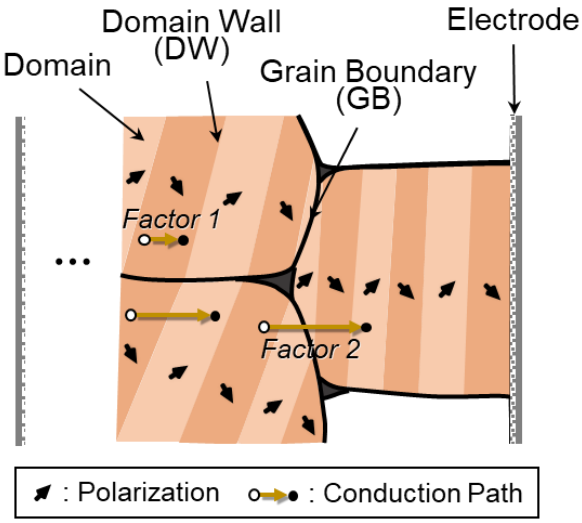

Figure 6.6: A schematic illustration of the relaxation process of LNKN6-a ML below T_C.

To consider why the log σ value of Factor 1 in the fatigued state increased below T_C, bottleneck areas of LNKN6-a were calculated from the lattice constant at 400 °C [68]. Cook et al. [124] and Sammells et al. [125]. reported that oxide ions in the perovskite structure had to pass through a bottleneck formed by two A-site cations and a B-site cation. Yashima et al. [126]. determined the oxide conduction pathway in a $LaGaO_3$-based perovskite by analyzing neutron diffraction patterns. Following the examples of these oxides, the conduction path and bottleneck region in LNKN6-a at 400 °C are illustrated in Fig. 6.7. The dimensions along the a-axis ($S_{BN,a-axis}$) (Fig. 6.7(a)) and c-axis ($S_{BN,c-axis}$) (Fig. 6.7(b)) related to oxygen ion conduction bottlenecks in LNKN6-a were 5.63 $Å^2$ and 5.73 $Å^2$, respectively [68]. Considering the domain structure in the as-sintered state as random and those in the as-poled and fatigued states as c-axis oriented, the larger bottleneck in the $S_{BN,c-axis}$ direction corresponded to an increase in conductivity in Factor 1 based on the domain orientation.

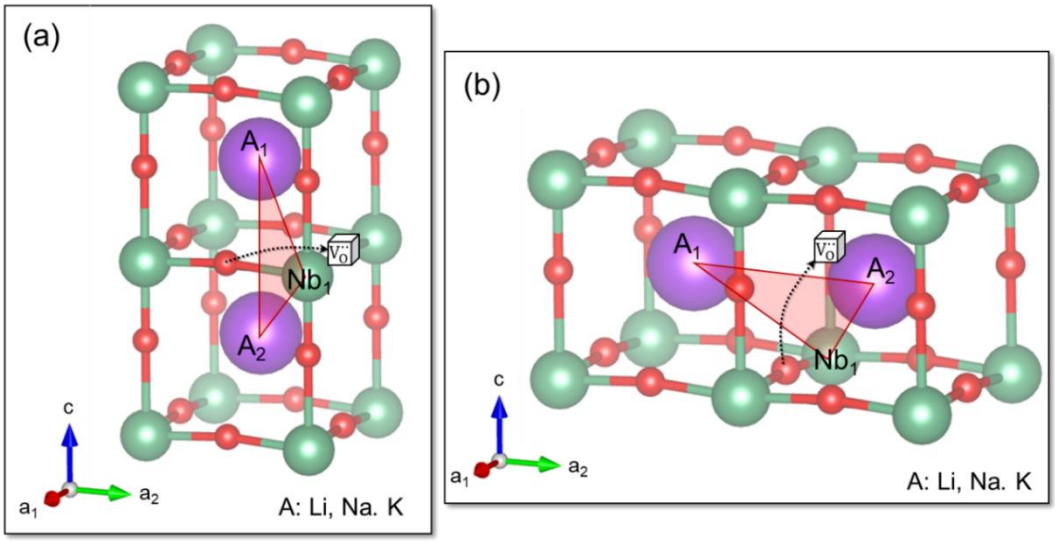

Figure 6.7: Anisotropy of oxygen vacancy conduction pathways along the (a) a-axis and (b) c-axis and the bottleneck areas at 400 °C. The bottleneck areas are indicated by red triangles, and the conduction pathways are denoted by dotted arrows. (Reprinted with permission from [72]. Copyright 2020 © The Japan Society of Applied Physics.)

Changes in the resistance at 500 °C are plotted for Factor 1 and Factor 2 in Fig. 6.8. The resistance of Factor 1 ($R_{Factor1}$) did not change, whereas that of Factor 2 ($R_{Factor2}$) increased from 7.6 kΩ in the as-sintered state to 9.1 kΩ in the fatigued state. Since ferroelectricity was eliminated, this behavior could not be attributed to DW pinning. Unipolar actuation could not have caused mechanical failure, because the elastic changes were smaller than those occurring during bipolar actuation. The anisotropy of changes in $R_{Factor1}$ and $R_{Factor2}$ in the paraelectric cubic phase was attributed to the formation of space charge layers near GBs. Alkali ion vacancies may have migrated from the GBs in the applied cyclic field at 100 °C, which could have raised the double-Schottky barriers,

resulting in an increased $R_{Factor2}$ in the paraelectric phase. Further investigation, including chemical analysis and observation of the microstructure near GBs, is required to confirm this.

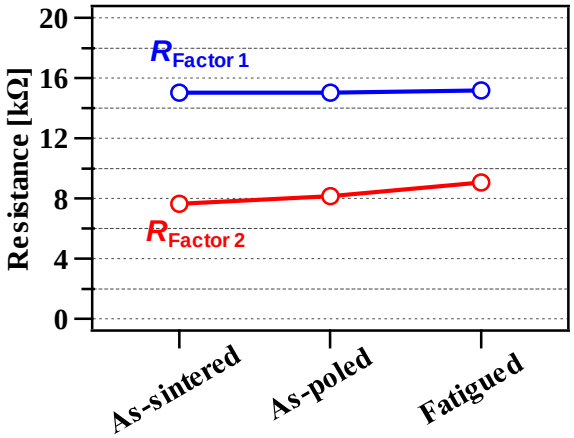

Figure 6.8: Resistance changes in Factors 1 and 2 measured at 500 °C before and after the fatigue test. (Reprinted with permission from [72]. Copyright 2020 © The Japan Society of Applied Physics.)

6.3 Conclusion

The unipolar fatigue of an ML piezoceramic, LNKN6-a ML, was investigated by measuring the unipolar *P*–*E* hysteresis and analyzing impedance spectra. Applying a cyclic field decreased the amount of polarization ($P_{Max} - P_0$) and dissipation energy (e_{loss}) by 8.9% and 8.2%, respectively, which was consistent with unipolar fatigue. The impedance spectra of LNKN6-a ML indicated that two relaxation processes occurred in the frequency range from 500 kHz to 10 mHz. These processes have also been observed in monolayered (Na,K)NbO_3-based ceramics. Below the T_C, these processes were attributed to inner domains

(Factor 1) and interfaces, including DWs and GBs (Factor 2). Above the T_C, Factors 1 and 2 were ascribed to grains and GBs, respectively. The intensity of the impedance spectra decreased isotropically by 47% due to a transition from the as-sintered state to the as-poled state. The intensity decreased by another 18% after cyclic field loading. This may have been due to an increase in the volume fraction of domains oriented toward the applied field, which would be facilitated by the DW pinning. On the other hand, $R_{Factor2}$ increased by 20.0%, even in the paraelectric phase. This suggested that fatigue occurred at the GBs, and that it was unrelated to the ferroelectric domain structure. ML structures with internal electrodes can be characterized by performing impedance spectroscopy and by comparing them with SL samples. The combination of unipolar *P*–*E* hysteresis and impedance spectroscopy is thus a powerful way to characterize unipolar fatigue in ML piezoceramics.

7. Summary and conclusion

First, we demonstrated the alkali volatilization of (Li,Na,K)NbO_3-based bulk piezoceramics to characterize the effect of A-site defects on ferroelectric and ferroelastic properties. We confirmed the experimental evidence that the alkali volatilization of LNKN6-a piezoceramics occurred less than 75 μm from the sample surface. Hence, when ceramic margins (75 μm) covering piezo-active layers were prepared, this effect was ruled out.

To investigate the electromechanical properties of LNKN6-a ML under harsh environments, we characterized two types of conditions: stress dependence and cyclic properties.

The large-signal unipolar behavior of LNKN6-a ML was characterized under combined electrical and mechanical loadings. The major trend of $d_{33}^{*}(\sigma)$ at 25 °C, which occurred over −200 MPa, exhibited a gradual decrease with a maximum in $d_{33}^{*}(\sigma)$ defined as σ_{peak}. This stress level was matched to the coercive stress σ_C of as-poled LNKN6-a ML. Therefore, σ_{peak}s below 100 °C were considered in terms of non-180° domain orientation produced by the balance of the combined electrical and stress fields. Notably, the ML showed this behavior as in bulk piezoceramics. On the other hand, $d_{33}^{*}(\sigma)$ at 100 °C exhibited a gradual decrease with no peak, but a hump at −80 MPa. The disappearance of the peak was considered as a thermal depolarization induced by the structural phase transition from orthorhombic to tetragonal. Additionally, the decrease in d_{33}^{*} up to −40 MPa was attributed to the fact that the material was in the PPT region. Therefore, its domain structure was readily clamped by the uniaxial stress.

In addition, a shift in T_{PPT} also affected the deterioration observed in a wide temperature range (25–100 °C). Consequently, our results suggest that the ML piezoceramic materials should be designed at the off-PPT region, rather than pursuing high piezoelectric constants at room temperature and under zero-stress conditions, by fixing the material composition in the PPT region.

The unipolar fatigue of LNKN6-a ML was also investigated using unipolar *P*–*E* hysteresis measurements and impedance spectroscopy. Applying a cyclic field decreased the amount of polarization ($P_{Max} - P_0$) and energy loss (e_{loss}), as reported in the previous studies of the unipolar fatigue. The impedance spectra of the ML revealed two relaxation processes, as observed in monolayered (Na,K)NbO_3-based ceramics. Hence, these processes were attributed to inner domains (Factor 1) and interfaces, such as DWs and GBs (Factor 2), below the T_C. Conversely, above the T_C, Factors 1 and 2 were ascribed to grains and GBs, respectively. The intensity of the impedance spectra decreased isotropically by 47% owing to a transition from the as-sintered state to the as-poled state. It decreased by another 18% after cyclic field loading. This further decrease may be attributed to an increase in the volume fraction of domains oriented toward the applied field, which was facilitated by the DW pinning. ML structures with internal electrodes can be characterized by performing impedance spectroscopy and comparing them with SL samples. The combination of unipolar *P*–*E* hysteresis and impedance spectroscopy is a powerful way to characterize unipolar fatigue in ML piezoceramics.

References

[1] M. Gagliardi, Am. Ceram. Soc. Bull. **99**, 7 (2020).

[2] A. V. Virkar and R. L. K. Matsumoto, J. Am. Ceram. Soc. **69**, C‐224 (1986).

[3] S. Kim, D. Kim, J. Kim and S. Cho, J. Am. Ceram. Soc. **73**, 161 (1990).

[4] S. Baik and S. M. Lee, J. Mater. Sci. **29**, 6115 (1994).

[5] F. Meschke, A. Kolleck and G. A. Schneider, J. Eur. Ceram. Soc. **17**, 1143 (1997).

[6] S. L. Dos Santos E Lucato, D. C. Lupascu and J. Rödel, J. Am. Ceram. Soc. **83**, 424 (2000).

[7] A. Kolleck, G. A. Schneider and F. A. Meschke, Acta Mater. **48**, 4099 (2000).

[8] A. B. K. Njiwa, T. Fett, D. C. Lupascu and J. Rödel, J. Am. Ceram. Soc. **86**, 1973 (2003).

[9] G. A. Schneider, Annu. Rev. Mater. Res. **37**, 491 (2007).

[10] G. Brennecka, R. Sherbondy, R. Schwartz and J. Ihlefeld, Am. Ceram. Soc. Bull. **99**, 24 (2020).

[11] E. Aksel and J. L. Jones, Sensors **10**, 1935 (2010).

[12] T. R. Shrout and S. J. Zhang, J. Electroceramics **19**, 111 (2007).

[13] H. F. Kay and P. Vousden, London, Edinburgh, Dublin Philos. Mag. J. Sci. **40**, 1019 (1949).

[14] S. Trolier-McKinstry, Am. Ceram. Soc. Bull. **99**, 22 (2020).

[15] M. De Jong, W. Chen, H. Geerlings, M. Asta and K. A. Persson, Sci. Data **2**, 1 (2015).

[16] P. M. Chaplya and G. P. Carman, J. Appl. Phys. **90**, 5278 (2001).

[17] Y. A. Genenko, J. Glaum, M. J. Hoffmann and K. Albe, Mater. Sci. Eng. B **192**, 52 (2015).

[18] J. Glaum and M. Hoffman, J. Am. Ceram. Soc. **97**, 665 (2014).

[19] K. Carl and K. H. Hardtl, Ferroelectrics **17**, 473 (1977).

[20] M. I. Morozov, M. A. Einarsrud, J. R. Tolchard, P. T. Geiger, K. G. Webber, D. Damjanovic and T. Grande, J. Appl. Phys. **118**, 164104 (2015).

[21] M. I. Morozov and D. Damjanovic, J. Appl. Phys. **107**, 034106 (2010).

[22] A. Chandrasekaran, X. K. Wei, L. Feigl, D. Damjanovic, N. Setter and N. Marzari, Phys. Rev. B **93**, 144102 (2016).

[23] N. Balke, H. Kungl, T. Granzow, D. C. Lupascu, M. J. Hoffmann and J. Rödel, J. Am. Ceram. Soc. **90**, 3869 (2007).

[24] X. Ren, Nat. Mater. **3**, 91 (2004).

[25] N. Balke, D. C. Lupascu, T. Granzow and J. Rödel, J. Am. Ceram. Soc. **90**, 1081 (2007).

[26] S. M. Yang, T. H. Kim, J. Yoon and T. W. Noh, Adv. Funct. Mater. **22**, 2310 (2012).

[27] F.-Z. Yao, K. Wang, J.-F. Li, J. Glaum, W. Jo and J. Rödel, Appl. Phys. Lett. **103**, 192907 (2013).

[28] J. Rödel, K. G. Webber, R. Dittmer, W. Jo, M. Kimura and D. Damjanovic, J. Eur. Ceram. Soc. **35**, 1659 (2015).

[29] K. G. Webber, M. Vögler, N. H. Khansur, B. Kaeswurm, J. E. Daniels and F. H. Schader, Smart Mater. Struct. **26**, 063001 (2017).

[30] W. Jo, R. Dittmer, M. Acosta, J. Zang, C. Groh, E. Sapper, K. Wang and J.

Rödel, J. Electroceramics **29**, 71 (2012).

[31] T. Tadashi, K. Maruyama and K. Sakata, Jpn. J. Appl. Phys. **30**, 2236 (1991).

[32] H. Simons, J. Glaum, J. E. Daniels, A. J. Studer, A. Liess, J. Rödel and M. Hoffman, J. Appl. Phys. **112**, 044101 (2012).

[33] N. Kumar, X. Shi, J. Jones and M. Hoffman, J. Am. Ceram. Soc. **102**, 5997 (2019).

[34] W. Liu and X. Ren, Phys. Rev. Lett. **103**, 257602 (2009).

[35] D. S. Keeble, F. Benabdallah, P. A. Thomas, M. Maglione and J. Kreisel, Appl. Phys. Lett. **102**, 092903 (2013).

[36] Y. Zhang, J. Glaum, M. C. Ehmke, K. J. Bowman, J. E. Blendell and M. J. Hoffman, J. Am. Ceram. Soc. **99**, 1287 (2016).

[37] G. Shirane, R. Newnham and R. Pepinsky, Phys. Rev. **96**, 581 (1954).

[38] Y. Guo, K. Kakimoto and H. Ohsato, Appl. Phys. Lett. **85**, 4121 (2004).

[39] K. Hatano, A. Yamamoto, Y. Doshida and Y. Mizuno, J. Ceram. Soc. Japan **123**, 561 (2015).

[40] D. W. Baker, P. A. Thomas, N. Zhang and A. M. Glazer, Appl. Phys. Lett. **95**, 2007 (2009).

[41] M. H. Zhang, K. Wang, J. S. Zhou, J. J. Zhou, X. Chu, X. Lv, J. Wu and J. F. Li, Acta Mater. **122**, 344 (2017).

[42] R. Wang, K. Wang, F. Yao, J. F. Li, F. H. Schader, K. G. Webber, W. Jo and J. Rödel, J. Am. Ceram. Soc. **98**, 2177 (2015).

[43] X. Lv, J. Wu, J. Zhu and D. Xiao, Phys. Chem. Chem. Phys. **20**, 20149 (2018).

[44] M. H. Zhang, K. Wang, Y. J. Du, G. Dai, W. Sun, G. Li, D. Hu, H. C. Thong, C. Zhao, X. Q. Xi, Z. X. Yue and J. F. Li, J. Am. Chem. Soc. **139**, 3889 (2017).

[45] N. Klein, E. Hollenstein, D. Damjanovic, H. J. Trodahl, N. Setter and M. Kuball, J. Appl. Phys. **102**, 014112 (2007).

[46] W. Ge, Y. Ren, J. Zhang, C. P. Devreugd, J. Li and D. Viehland, J. Appl. Phys. **111**, 103503 (2012).

[47] T. Iamsasri, G. Tutuncu, C. Uthaisar, S. Wongsaenmai, S. Pojprapai and J. L. Jones, J. Appl. Phys. **117**, 024101 (2015).

[48] N. H. Khansur, A. Martin, K. Riess, H. Nishiyama, K. Hatano, K. Wang, J. F. Li, K. Kakimoto and K. G. Webber, Appl. Phys. Lett. **117**, 032901 (2020).

[49] P. Zhao, B. P. Zhang and J. F. Li, Appl. Phys. Lett. **90**, 242909 (2007).

[50] K. Wang and J. F. Li, J. Adv. Ceram. **1**, 24 (2012).

[51] Y. Wang, D. Damjanovic, N. Klein and N. Setter, J. Am. Ceram. Soc. **91**, 1962 (2008).

[52] D. Jenko, A. Benčan, B. Malič, J. Holc and M. Kosec, Microsc. Microanal. **11**, 572 (2005).

[53] M. S. Kim, S. Jeon, D. S. Lee, S. J. Jeong and J. S. Song, J. Electroceramics **23**, 372 (2009).

[54] S. Kawada, M. Kimura, Y. Higuchi and H. Takagi, Appl. Phys. Express **2**, 111401 (2009).

[55] M. I. Morozov, M. Bäurer and M. J. Hoffmann, J. Am. Ceram. Soc. **94**, 3591 (2011).

[56] K. Hatano, K. Kobayashi, T. Hagiwara, H. Shimizu, Y. Doshida and Y.

Mizuno, Jpn. J. Appl. Phys. **49**, 09MD11 (2010).

[57] R. Gao, X. Chu, Y. Huan, X. Wang and L. Li, Phys. Status Solidi Appl. Mater. Sci. **211**, 2378 (2014).

[58] R. Gao, X. Chu, Y. Huan, Z. Zhong, X. Wang and L. Li, J. Eur. Ceram. Soc. **35**, 389 (2015).

[59] R. Gao, X. Chu, Y. Huan, Y. Sun, J. Liu, X. Wang and L. Li, Smart Mater. Struct. **23**, 105018 (2014).

[60] L. Gao, H. Guo, S. Zhang and C. Randall, Actuators **5**, 8 (2016).

[61] L. Gao, S. W. Ko, H. Guo, E. Hennig, C. A. Randall and J. L. Jones, J. Am. Ceram. Soc. **99**, 2017 (2016).

[62] T. Reimann, S. Fröhlich, A. Bochmann, A. Kynast, M. Töpfer, E. Hennig and J. Töpfer, J. Eur. Ceram. Soc. **41**, 344 (2020).

[63] K. Kobayashi, Y. Doshida, Y. Mizuno and C. A. Randall, Jpn. J. Appl. Phys. **52**, 09KD07 (2013).

[64] K. Hatano, G. Watanabe, S. Kishimoto and N. Sasaki, Jpn. J. Appl. Phys. **59**, SPPD01 (2020).

[65] R. A. Eichel, E. Erünal, P. Jakes, S. Körbel, C. Elsässer, H. Kungl, J. Acker and M. J. Hoffmann, Appl. Phys. Lett. **102**, 242908 (2013).

[66] R. A. Eichel, H. Kungl and P. Jakes, Mater. Technol. **28**, 241 (2013).

[67] K. Hatano, A. Yamamoto, S. Kishimoto and Y. Doshida, Jpn. J. Appl. Phys. **55**, 10TD03 (2016).

[68] A. Martin, K. Kakimoto, K. Hatano, Y. Doshida and K. G. Webber, J. Appl. Phys. **122**, 204102 (2017).

[69] Y. Arai, "Chemistry of Powder Production", Chapman & Hall, United

Kingdom (1996) pp.215–216.

[70] T. Rojac, A. Benčan, H. Uršič, B. Malič and M. Kosec, J. Am. Ceram. Soc. **91**, 3789 (2008).

[71] R. Dittmer, K. G. Webber, E. Aulbach, W. Jo, X. Tan and J. Rödel, Sensors Actuators A **189**, 187 (2013).

[72] H. Nishiyama, K. Kakimoto, K. Hatano, S. Kishimoto and N. Sasaki, Jpn. J. Appl. Phys. **59**, SPPD05 (2020).

[73] K. G. Webber, E. Aulbach, T. Key, M. Marsilius, T. Granzow and J. Rödel, Acta Mater. **57**, 4614 (2009).

[74] H. Nishiyama, A. Martin, K. Hatano, S. Kishimoto, N. Sasaki, K. G. Webber and K. Kakimoto, J. Ceram. Soc. Japan., **129**, 127 (2021).

[75] H. E. Mgbemere, M. Hinterstein and G. A. Schneider, J. Am. Ceram. Soc. **96**, 201 (2013).

[76] Z. Samardžija, S. Bernik, R. B. Marinenko, B. Malič and M. Čeh, Microchim. Acta **145**, 203 (2004).

[77] L.-Q. Cheng, K. Wang, F.-Z. Yao, F. Zhu and J.-F. Li, J. Am. Ceram. Soc. **96**, 2693 (2013).

[78] K. Kakimoto, R. Kaneko and I. Kagomiya, Jpn. J. Appl. Phys. **51**, 09LD06 (2012).

[79] K. Kato, K. Kakimoto, K. Hatano, K. Kobayashi and Y. Doshida, J. Ceram. Soc. Japan **122**, 460 (2014).

[80] T. M. Kamel and G. de With, J. Eur. Ceram. Soc. **28**, 851 (2008).

[81] Y. Zhao, Y. Ge, X. Yuan, Y. Zhao, H. Zhou, J. Li and H. B. Jin, J. Alloys Compd. **680**, 467 (2016).

[82] F. Yao, J. Glaum, K. Wang, W. Jo, J. Rödel, J. Li and J. Li, Appl. Phys. Lett. **103**, 192907 (2013).

[83] A. Martin, K. Kakimoto, K. Hatano and Y. Doshida, J. Ceram. Soc. Japan **124**, 730 (2016).

[84] H. S. Han, J. Koruza, E. A. Patterson, J. Schultheiß, E. Erdem, W. Jo, J. S. Lee and J. Rödel, J. Eur. Ceram. Soc. **37**, 2083 (2017).

[85] Z. Cen, Y. Zhen, W. Feng, P. Zhao, L. Chen, X. Wang and L. Li, J. Eur. Ceram. Soc. **38**, 3136 (2018).

[86] K. Kobayashi, Y. Doshida, Y. Mizuno and C. A. Randall, J. Am. Ceram. Soc. **95**, 2928 (2012).

[87] M. Marsilius, K. G. Webber, E. Aulbach and T. Granzow, J. Am. Ceram. Soc. **93**, 2850 (2010).

[88] H. Zhang, C. Groh, Q. Zhang, W. Jo, K. G. Webber and J. Rödel, Adv. Electron. Mater. **1**, 1500018 (2015).

[89] A. B. Kounga, E. Aulbach, T. Granzow and J. Rödel, Acta Mater. **55**, 675 (2007).

[90] C. A. Randall, A. Kelnberger, G. Y. Yang, R. E. Eitel and T. R. Shrout, J. Electroceramics **14**, 177 (2005).

[91] M. S. Senousy, R. K. N. D. Rajapakse, D. Mumford and M. S. Gadala, Smart Mater. Struct. **18**, 045008 (2009).

[92] F. X. Li, R. K. N. D. Rajapakse, D. Mumford and M. Gadala, Smart Mater. Struct. **17**, 015049 (2008).

[93] I. Kerkamm, P. Hiller, T. Granzow and J. Rödel, Acta Mater. **57**, 77 (2009).

[94] R. Dittmer, K. G. Webber, E. Aulbach, W. Jo, X. Tan and J. Rödel, Acta

Mater. **61**, 1350 (2013).

[95] H. Zhang, W. Ma, B. Xie, L. Zhang, S. Dong, P. Fan, K. Wang, J. Koruza and J. Rödel, J. Am. Ceram. Soc. **102**, 6147 (2019).

[96] H. I. Humburg, M. Acosta, W. Jo, K. G. Webber and J. Rödel, J. Eur. Ceram. Soc. **35**, 1209 (2015).

[97] H. Nishiyama, A. Martin, K. Hatano, S. Kishimoto, K. Kakimoto and K. Hatano, J. Appl. Phys. **128**, 244101 (2020).

[98] A. Furuta and K. Uchino, J. Am. Ceram. Soc. **76**, 1615 (1993).

[99] S. R. Winzer, N. Shankar and A. P. Ritter, J. Am. Ceram. Soc. **72**, 2246 (1989).

[100] S. Takahashi, A. Ochi, M. Yonezawa, T. Yano, T. Hamatsuki and I. Fukui, Ferroelectrics **50**, 181 (1983).

[101] H. Kungl, T. Fett, S. Wagner and M. J. Hoffmann, J. Appl. Phys. **101**, 044101 (2007).

[102] A. Martin, N. H. Khansur, U. Eckstein, K. Riess, K. Kakimoto and K. G. Webber, J. Appl. Phys. **127**, 114101 (2020).

[103] F. H. Schader, M. Morozov, E. T. Wefring, T. Grande and K. G. Webber, J. Appl. Phys. **117**, 194101 (2015).

[104] F. H. Schader, D. Isaia, M. Weber, E. Aulbach and K. G. Webber, J. Mater. Sci. **53**, 3296 (2018).

[105] F. H. Schader, N. Khakpash, G. A. Rossetti, Jr. and K. G. Webber, J. Appl. Phys. **121**, 064109 (2017).

[106] K. Wang, F. Z. Yao, J. Koruza, L. Q. Cheng, F. H. Schader, M. H. Zhang, J. Rödel, J. F. Li and K. G. Webber, J. Am. Ceram. Soc. **100**, 2116 (2017).

[107] K. Wang, F. Z. Yao, W. Jo, D. Gobeljic, V. V. Shvartsman, D. C. Lupascu, J. F. Li and J. Rödel, Adv. Funct. Mater. **23**, 4079 (2013).

[108] N. Balke, T. Granzow and J. Rödel, J. Appl. Phys. **105**, 104105 (2009).

[109] J. Fleig and J. Maier, J. Eur. Ceram. Soc. **19**, 693 (1999).

[110] D. C. Sinclair and A. R. West, Phys. Rev. B **39**, 13486 (1989).

[111] H. Nishiyama, K. Kakimoto, K. Hatano and Y. Konishi, Jpn. J. Appl. Phys. **56**, 10PD07 (2017).

[112] S. W. Gotmare, S. O. Leontsev and R. E. Eitel, J. Am. Ceram. Soc. **93**, 1965 (2010).

[113] Z. Li, M. Grimsditch, C. M. Foster and S. K. Chan, J. Phys. Chem. Solids **57**, 1433 (1996).

[114] Z. Luo, J. Glaum, T. Granzow, W. Jo, R. Dittmer, M. Hoffman and J. Rödel, J. Am. Ceram. Soc. **94**, 529 (2011).

[115] M. Fukunaga and Y. Noda, J. Phys. Soc. Japan **77**, 1 (2008).

[116] T. Yamaguchi and M. Takashige, Phisical Soc. Japan **66**, 603 (2011).

[117] F. Hussain, I. Sterianou, A. Khesro, D. C. Sinclair and I. M. Reaney, J. Eur. Ceram. Soc. **38**, 3118 (2018).

[118] C. Long, T. Li, H. Fan, Y. Wu, L. Zhou, Y. Li, L. Xiao and Y. Li, J. Alloys Compd. **658**, 839 (2016).

[119] D. C. Sinclair and A. R. West, J. Appl. Phys. **66**, 3850 (1989).

[120] H. Chazono and K. Hiroshi, Jpn. J. Appl. Phys. **40**, 5624 (2001).

[121] F. Jona and G. Shirane, Ferroelectric Crystals, Pergamon Press (1962) pp.111.

[122] M. Saiful Islam, J. Mater. Chem. **10**, 1027 (2000).

[123] B. Guiffard, E. Boucher, L. Eyraud, L. Lebrun and D. Guyomar, J. Eur.

Ceram. Soc. **25**, 2487 (2005).

[124] R. L. Cook and A. F. Sammells, Solid State Ionics **45**, 311 (1991).

[125] A. F. Sammells, R. L. Cook, J. H. White, J. J. Osborne and R. C. MacDuff, **52**, 111 (1992).

[126] M. Yashima, K. Nomura, H. Kageyama, Y. Miyazaki, N. Chitose and K. Adachi, Chem. Phys. Lett. **380**, 391 (2003).

List of Figures

List of Tables

Acknowledgement

Numerous individuals have contributed to this thesis and supported me during the three years of research.

First and foremost, I would like to express my sincere gratitude to my advisor, Prof. Dr. Ken-ichi Kakimoto, for providing me with the opportunity to complete my doctoral thesis at the Nagoya Institute of Technology. He greatly supported this research project and also contributed my personal development with his knowledge and experience. His guidance, openness, and humor were the foundation for the strict but pleasant working atmosphere that I totally enjoyed. I am humbly grateful for the opportunity to have met such an excellent role model, both as a scientist and a father figure. I will never forget the lesson: always keep in mind the backcasting images of the research fields.

I would also like to thank my committee members, Prof. Dr. Hirotaka Maeda and Assoc. Prof. Dr. Toru Asaka, for their continued support, even during hardship. I would also like to extend gratitude for their insightful comments and suggestions.

My sincere thanks go to Prof. Dr. Wataru Sakamoto at Chubu University as I greatly benefited from his outstanding expertise and his commitment to science.

I would also like to extend special thanks to Prof. Dr. Kyle Grant Webber and Dr. Neamul Hayet Khansur for their friendship and fruitful discussions, through which ideas for this study were born. Without their kind support and

advice, this work would not have been successful. I also acknowledge Kevin Rieß and Udo Eckstein for their excellent experimental and technical supports.

In addition, I want to thank Taiyo Yuden Co., Ltd for the overall support of my work and providing the (Li,Na,K)NbO_3 samples. Further, special thanks goes to Keiichi Hatano for sharing his knowledge and providing me with invaluable advice.

Furthermore, I would like to express my gratitude to Assist. Prof. Dr. Martin Alexander for his inspirational advice and dedication for reviewing the English in my manuscript. He was always available for providing help and scientific discussions. His optimistic and cooperative attitude is exemplary and will not be forgotten.

I owe a great debt of gratitude to all members of the electroceramics laboratory at Nagoya Institute of Technology for the friendly and inspiring working atmosphere as well as the fond memories and experiences that I owe to them. I am especially grateful to Assist. Prof. Dr. Teruaki Fuchigami for improving the atmosphere of the laboratory training seminar. Your insightful comments always inspire my research as well as the other scientific fields.

Last but not least, I owe an invaluable debt of gratitude to my beloved parents, Susumu and Rika, as well as my big brother Wataru. Without your love, patience, and support during my studies and throughout my life, this work could not have been accomplished.

Hiroshi Nishiyama
Nagoya, March 2021